

The title "ANNUAL REPORT 2019" is centered on the page. The word "ANNUAL" is in a black serif font, "REPORT" is in a green serif font, and "2019" is in a black serif font. The text is surrounded by decorative elements: a large grey pentagon with three concentric white outlines on the left, a solid grey pentagon on the right, and a smaller grey pentagon below the word "REPORT". On the right side of the page, there are several parallel diagonal lines in shades of blue and green.

Kansai Photon Science Institute
Quantum Beam Science Research Directorate
National Institutes for
Quantum and Radiological Science and Technology

**ANNUAL
REPORT
2019**

Contents

Preface	1
Activities of KPSI	3
User Facilities	9
Research Highlights	15
Publication List	57
The Kids' Science Museum of Photons	71
Appendix	83

はじめに

本年報では、関西光科学研究所（以下、関西研）において 2019 年度に実施された研究開発の主な成果を紹介しています。関西研は国立研究開発法人量子科学技術研究開発機構（以下、量研）の研究開発拠点であり、けいはんな学研都市にある京都府木津地区と兵庫県播磨地区の 2 か所に研究サイトを持っています。ここでは、研究系職員約 80 名及びそれを支える技術系・事務系スタッフを含めて総勢約 150 名のスタッフが、量研における関西研のミッションである「レーザーや放射光による光科学技術の研究開発」を推進しています。木津地区では、世界トップレベルの高強度レーザー技術を基盤としたレーザー加速や X 線発生等のレーザー駆動の新しい放射線源開発、レーザーの短パルス性を活かした超高速計測技術開発、そして放射線影響や創薬に資する量子生命科学の最先端の研究開発を実施しています。また、播磨地区では、大型放射光施設 SPring-8 に 2 本の専用ビームラインと計算機シミュレーションを活用することで、新しい放射光 X 線利用技術開発と物質材料科学の最先端研究を展開しています。2019 年度からは、量研の組織改変に伴って量子生命科学領域が発足し、その分野に関連する 2 つの研究グループが本部直轄の研究領域に移りましたが、関西研全体としては、これまで通り、量研の成果最大化に向けて最大限努めて参りたいと思います。

木津地区のレーザー科学分野においては、次世代の高強度レーザーを支える励起光源の安定化や、パラメトリック増幅を用いた新しい発振器の提案がなされました。また、レーザーイオン加速研究においては照射強度と加速エネルギーの新しい関係性の解明、そして、量子生命科学領域においては、単一分子を対象として DNA 損傷を直接観察する試み等の新たな知見が生まれています。また、播磨地区においても、共鳴非弾性散乱法による銅酸化物超伝導体の電子励起の詳細な観察や、幾何学的にフラストレーションを内包する三角格子磁性体の磁気特性の理論考察など、数多くの優れた成果を挙げています。さらに、光技術の実用化の観点からは、非侵襲血糖値測定やレーザーによるトンネル検査技術の実用化に向けた取組を引き続き行っています。

関西光科学研究所は、「光」を通じた我が国の量子科学技術の発展とイノベーション戦略に貢献する開かれた研究拠点としての役割を果たすべく、今後とも職員一同、より一層努力してまいります。皆様のご理解・ご協力を宜しくお願い申し上げます。

2020 年吉日
関西光科学研究所
所長 河内 哲哉



Preface

This annual report from the Kansai Photon Science Institute (KPSI) provides highlights of the scientific and technical research that was conducted over the 2019 fiscal year.

KPSI is one of the research and development (R&D) bases of the National Institute of Quantum and Radiological Science and Technology (QST). At KPSI's two R&D sites—the Kizu site in Keihanna Science City in Kyoto Prefecture and the Harima site in Hyogo Prefecture—there are around 150 staff, comprising around 80 researchers and the technical and administrative staff who support them. We promote the R&D of optical science and technology using lasers and synchrotron-radiation X-rays, which is the mission of KPSI at QST. At the Kizu site, we are conducting state-of-the-art research such as developing new types of laser-driven radiation sources, such as laser-accelerated particle beams and ultrashort X-rays based on world-leading top-class high-intensity laser technology, ultrafast measurement methodology using ultrashort pulse technology, and quantum life science that helps us to understand radiation effects and to develop new medicines. At the Harima site, using the two contract beamlines of SPring-8 and computer simulations, we are developing new technology to utilize synchrotron-radiation X-rays and carrying out state-of-the-art research in materials science. From FY2019, QST organized a new institute, the Institute for Quantum Life Sciences, under the direct control of the president, and two research groups related to this research field have been transferred to this new institute while keeping their location at KPSI. However, KPSI will continue to support all the research groups to maximize the results of QST.

In the laser science field at the Kizu site, we have developed an optically synchronized stable pump laser and a new optical parametric oscillator, which will become seed technologies toward next-generation high-power lasers. In laser-driven ion acceleration research, we have firstly revealed the relationship between laser intensity and accelerated ion energy by taking the effect of the spot size into account. In the field of life sciences, new findings have been obtained through attempts to directly observe DNA damages for single molecules. At the Harima site, we obtained several excellent results such as detailed observation of electronic excitation of copper-oxide superconducting substances using resonant inelastic X-ray scattering and theoretical investigation of the magnetic properties of substances on a triangular lattice system, which may include geometrical frustration. In addition, regarding the social implementation of optical technology, we are making efforts toward practical application of non-invasive blood glucose measurement and laser-based tunnel inspection technology.

KPSI will continue to fulfill its role as an open research center of the "science of light" and will contribute to quantum science and technology and the strategy for innovation in Japan. We appreciate your understanding and cooperation.

Good day, 2020
Director General of KPSI
Tetsuya KAWACHI

Activities of KPSI

関西光科学研究所の主な動き

【シンポジウム・研究会等の開催】

2019年6月12日

「光・量子ビーム科学合同シンポジウム 2019」
(阪大・銀杏会館、大阪府吹田市)

大阪大学と量研との間で締結された包括協定に基づき、合同シンポジウムを開催しました。参加者は約200名であり、招待講演・口頭発表、ポスター発表、若手ポスター賞表彰式、意見交換会が行われました。



左：シンポジウム開催案内版
右：若手ポスター発表賞表彰の様子

2019年7月8日

「レーザー・物質相互作用における非線形応答ミニワークショップ」(関西研、京都府木津川市)
CREST「光・電子融合第一原理ソフトウェアの開発と応用」とQ-LEAP(ALICE)「次世代レーザー」が主催する“物質とレーザーの非線形相互作用に関するミニワークショップ”が35名の参加者によって木津地区にて行われました。国内外の研究者が発表・議論を行いました。



左：ワークショップの様子、右：参加者集合写真 (ITBL 棟)

2019年8月30、31日

「SPring-8 シンポジウム 2019」(岡山県岡山市)

岡山大学において、「次の20年に向けての一步」と題して、SPring-8 が次の20年後も利用者にとって魅力的な放射光施設であり続けるための具体的な取り組みや仕組みをテーマとして開催されました。



シンポジウム会場の様子 (岡山大学、写真提供：SPring-8 シンポジウム 2019 事務局)

2019年12月4、5日

「第3回 QST 国際シンポジウム」(奈良春日野国際フォーラム薨、奈良県奈良市)

昨年に引き続き、奈良春日野国際フォーラム薨(奈良県奈良市)にて国際シンポジウムを行いました。今回のテーマは「Quantum Life Science (量子生命科学)」で、208名の参加者が集いました。Luke Lee 博士(カリフォルニア大学バークレー校/USA)、Murali Krishna Cherukuri 博士(NIH/USA)による基調講演をはじめ、国内外の研究者による5つのセッションの他、ポスター発表56件が行われました。



2020年1月10-12日

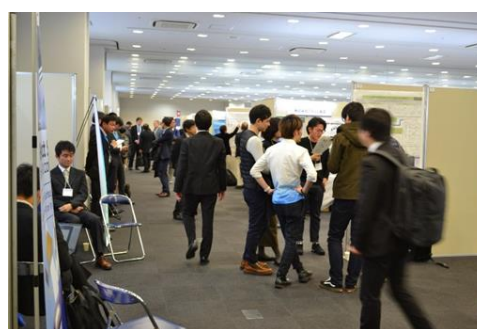
「第33回日本放射光学会年会・放射光科学合同シンポジウム」(愛知県産業労働センター)

本シンポジウムは放射光を利用した研究成果、放射光用の加速器、光源、ビームライン、測定器の技術開発、放射光施設運営も含めた放射光施設と利用に係る総合的な発表と議論の場となっています。量研からも、次世代放射光施設計画の企画講演や施設報告のほか、稲見上席研究員が発見した新しいX線磁気光学効果の理論的研究(小出博士研究員)や、同効果を応用した磁気光学顕微鏡開発(菅原技術員)の発表など、多数の発表が行われました。



左：メインホールの様子

(写真提供：JSR2020事務局)



右：ポスターセッションと企業展示の様子

(写真提供：JSR2020事務局)

2020年2月13、14日

「第3回 理研光量子工学研究センター・量研関西光科学研究所合同セミナー」(三重県伊勢市)

毎年RIKEN-RAPとQST-KPSIが合同で行っているセミナーを「伊勢かぐらばリゾート千の杜」にて開催いたしました。22名の参加者があり、レーザー開発から応用にいたる研究について、2日間にわたる

合宿形式のセミナーを行いました。



左：参加者集合写真、右：セミナーの様子

【施設公開】

第 27 回 SPring-8/SACLA 施設公開

4 月 27 日（土）に恒例の SPring-8/SACLA 施設公開が大型放射光施設 SPring-8（兵庫県佐用郡佐用町）で開催されました。施設公開では、普段なかなか入ることのできない蓄積リング棟の見学や、講演会の聴講、実験の体験ができるだけでなく、地元特産品などの販売も行われました。今年は親子連れや学生さんを中心に 2,056 名の方が参加されました。



展示実験を楽しむ来場者の皆様（播磨地区）

関西光科学研究所（木津地区）施設公開

10 月 27 日（日）に関西光科学研究所（木津地区）の施設公開を開催しました。1148 名の方々にご来場いただき、世界トップクラスの高強度レーザー施設見学や、光の実験ショー、高校生や大人も楽しめるサイエンスカフェ、木津南中学吹奏楽部の演奏会等を行いました。木津地区の施設公開は例年 10 月最終日曜日に行っております。



左：ふおとんくんがお出迎え、右：関西研（木津地区）施設公開当日のスタッフ集合写真

【主な出展等イベント】

QST 関西光科学研究所では、2019 年度も積極的にアウトリーチ活動を実施しました。「きつづ光科学館 ふおとん」の年間来場者は 50,963 人を達成しました。(ただし COVID-19 感染症対策のために 2020 年 2 月 27 日からは臨時休館中です。2020 年 3 月 31 日現在)

4 月 7 日 「第 42 回花と緑の見学会」出展 (QST 高崎量子応用研究所、群馬県高崎市)

7 月 7-10 日 「第 19 回 SPring-8 夏の学校」開催 (大型放射光施設 SPring-8、兵庫県佐用町)

7 月 13、14 日 「大阪科学技術館 テクノくん夏祭り 2019」サイエンスショー&科学工作 (大阪科学技術館、大阪府大阪市)

7 月 20、21 日 「姫路・桜山公園まつり 科学の屋台村」出展 姫路市桜山公園 (兵庫県姫路市)

7 月 25 日 「夏休み 2019 宿題自由研究大作戦」サイエンスショー&科学工作 (みやこメッセ京都、京都府京都市)

7 月 27、28 日 「青少年のための科学の祭典 2019 全国大会」出展 (科学技術館、東京都千代田区)

9 月 22 日 「核融合とレーザー 作る・体験する・学ぶ」サイエンスショー・科学工作 (大阪市中央公会堂、大阪府大阪市)

10 月 3、4 日 「京都スマートシティエキスポ 2019」、「第 13 回けいはんなビジネスメッセ 2019」同時開催への出展 (けいはんなオープンイノベーションセンター、京都府相楽郡精華町)

10 月 17 日 「播磨高原東中学校出前授業」(播磨科学公園都市、兵庫県たつの市)

10 月 31 日-11 月 2 日 「けいはんな情報通信フェア 2019」出展 (けいはんなプラザ、京都府相楽郡精華町)

2020 年 1 月 29-31 日 「第 19 回国際ナノテクノロジー総合展・技術会議 (nano tech 2020) 出展 (東京ビックサイト、東京都江東区)



左：第 19 回 SPring-8 夏の学校参加者の全体集合写真 (写真提供：高輝度光科学研究センター)



右：「核融合とレーザー 作る・体験する・学ぶ」サイエンスショー・科学工作の様子

User Facilities

主要な施設・装置

木津地区

○J-KAREN レーザー装置

【装置概要】

世界トップクラスの極短パルス超高強度レーザーです。30J のレーザーエネルギーを 30 フェムト秒（1 フェムトは 1000 兆分の 1）の時間に閉じ込めることにより 1000 兆ワットの超高強度を実現します。（右の写真は強力な励起レーザーの光で緑色に光っています。）

【装置性能】

- ・照射エネルギー：30 J/pulse
- ・コントラスト比： 10^{-12}
- ・波長：800 nm
- ・繰り返し：0.1 Hz
- ・パルス幅：30 フェムト秒
- ・集光強度： 10^{22} W/cm²

【主要な研究課題】

レーザーの高度化技術の開発、イオンおよび電子のレーザー加速技術の開発、高エネルギーコヒーレント X 線の発生等



○X 線レーザー実験装置

休止中

○QUADRA-T レーザーシステム

【装置概要】

1 秒間に 1000 発のレーザーパルスが繰り返せる高平均出力ピコ秒パルスレーザーです。中心周波数 0.3 THz の高強度テラヘルツパルスを発生することが可能です。

【装置性能】

- ・照射エネルギー：10 mJ/pulse
- ・波長：1030 nm
- ・繰り返し：1 kHz
- ・パルス幅：約 1 ピコ秒

【主要な研究課題】

高繰り返し高出力レーザー（パラメトリック増幅器等）の開発、高強度テラヘルツ光源の開発



播磨地区

播磨地区では大型放射光施設 SPring-8 に 2 本の QST 専用ビームラインを設置しているほか、日本原子力研究開発機構（JAEA）の専用ビームラインにも複数の放射光専用実験装置を常設しています。一方で、QST 専用ビームラインにも、JAEA の専用実験装置が常設されています。

○BL11XU (QST 極限量子ダイナミクス I ビームライン)

【装置概要】

SPring-8 標準の真空封止アンジュレータを光源とし、マルチ結晶交換システムを装備することで、広範囲のエネルギー領域の高輝度放射光 X 線を高効率に利用できるビームラインです。

【装置性能】

- ・光源：真空封止アンジュレータ
- ・エネルギー領域：6～70 keV
- ・分光結晶：Si(111)、Si(311)
- ・実験装置：放射光メスバウアー分光装置、共鳴非弾性 X 線散乱装置、及び表面 X 線回折計

1. 放射光メスバウアー分光装置

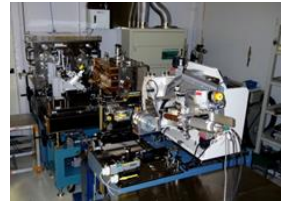
^{57}Fe 、 ^{61}Ni 等のメスバウアー核種を対象とした放射光メスバウアー分光が可能で、物質の電子、磁気状態から格子振動状態に関する情報などを得ることができます。

2. 共鳴非弾性 X 線散乱装置

2m 長アームに搭載した球面湾曲型集光式アナライザー結晶による背面反射を用いることで、高分解能の X 線分光を行い、散乱光の方位や入射光とのエネルギー差から、運動量移行を伴う固体内素励起が観察できます。

3. 表面 X 線回折計

分子線エピタキシー (MBE) チェンバーを搭載した表面構造解析用装置で、窒化物を含む半導体結晶などの成長過程を、X 線回折法を用いてその場観察・リアルタイム観察することができます。



【主要な研究課題】

金属薄膜の原子層単位での磁性探査、白金系燃料電池触媒の電子状態解析、半導体量子ドットや半導体多層膜の成長過程のリアルタイム解析

○BL14B1 (QST 極限量子ダイナミクス II ビームライン)

【装置概要】

偏向電磁石を光源とすることで、連続スペクトルを持つ白色 X 線や高エネルギーの単色 X 線が利用可能なビームラインです。全反射ミラーや分光結晶の曲げ機構によって、試料位置への集光が可能となっています。

【装置性能】

- ・光源：偏向電磁石
- ・エネルギー領域：白色 X 線 (5～150 keV)、単色 X 線 (5～90 keV)
- ・実験装置：高温高圧プレス装置、分散型 XAFS 測定装置 (JAEA) 及び κ (カッパー) 型回折計 (JAEA)

1. 高温高圧プレス装置

高温高圧の条件下にある試料を、白色 X 線を用いたエネルギー分散型 X 線回折法やラジオグラフィ法、単色 X 線を用いた XAFS (X 線吸収微細構造) 法や角度分散型 X 線回折法によって調べることができます。

【主要な研究課題】

高圧下での金属水素化物形成過程のその場観察



2. 汎用四軸 X 線回折計

令和 2 年 3 月に RI 実験棟から移設。令和 2 年度からビーム利用実験に向けて、試験調整等を行う予定です。

【主要な研究課題】

残留応力評価等、様々な研究に活用予定。



○BL22XU (JAEA 専用ビームライン) における放射光専用実験装置

1. 単色 X 線実験用高温高压プレス装置 (JAEA BL22XU)

高温高压下 (到達圧力 10 GPa (10 万気圧)、到達温度 2000 K 程度) の X 線回折測定や X 線吸収法を用いた密度測定、室温、1 MPa 未満の水素ガス雰囲気中でのその場 X 線回折観察、時分割 X 線回折測定が可能な装置です (令和 2 年 7 月に放射光物性研究棟に移設)。

2. ダイヤモンドアンビルセル回折計 (JAEA BL22XU)

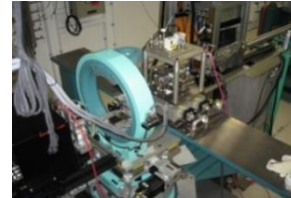
大型イメージングプレート検出器と高エネルギー X 線を利用することにより、高压下での単結晶 X 線回折及び粉末 X 線回折実験、X 線全散乱測定及び原子二体分布関数 (PDF) 解析が可能な装置です。

3. 大型 X 線回折計

共鳴 X 線散乱による電子軌道状態の観測、スペックル回折によるドメイン構造の研究、応力・歪み分布測定などの回折マッピングなど多目的に利用する四軸回折計です。

【主要な研究課題】

水素貯蔵合金の水素吸蔵過程の時分割その場 X 線回折測定、負の熱膨張材料、超伝導体、f 電子系化合物、コヒーレント X 線を利用したスペックル散乱によるナノドメイン観察。応力・歪みの 3 次元分布測定、等



施設の稼働実績

○木津地区

実施課題件数

装置名称	独自研究	受託研究	共同研究	施設共用
J-KAREN レーザー装置	3	3	4	4
X 線レーザー実験装置	0	0	0	0
QUADRA-T レーザーシステム	1	0	0	0
kHz チタンサファイアレーザー	8	1	1	0
X 線回折装置	1	0	1	0

○播磨地区

2019年度のSPring-8蓄積リングの運転時間は約5280時間で、放射光利用時間はそのうちの約4584時間でした。量研、原子力機構とも専用ビームラインでは10～20%弱程度の調整時間を除き、放射光利用時間で独自研究や受託研究、外部利用者への施設共用と研究支援を行っています。

実施課題件数

ビームライン	独自研究	受託研究	共同研究	施設共用
BL11XU	8	0	4	21
BL14B1	7	0	5	12
BL22XU	5	0	3	9

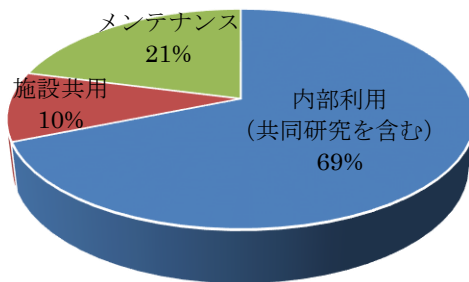
利用日数

ビームライン	独自研究	受託研究	共同研究	施設共用
BL11XU	81	0	28	61
BL14B1	33	0	17	38
BL22XU	0	0	23	24

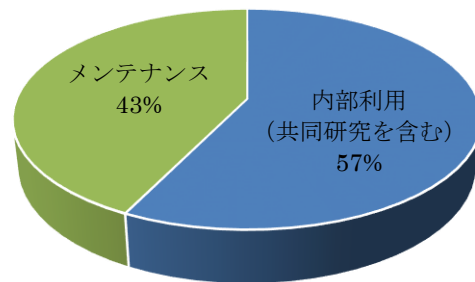
施設の利用状況

○木津地区

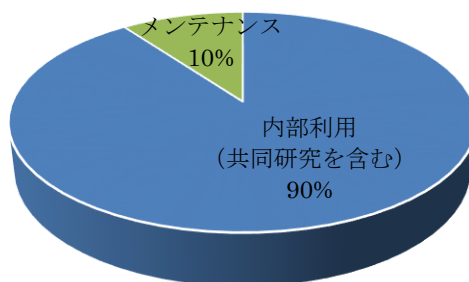
J-KAREN レーザー装置
(合計ビームタイム：1752時間)



QUADRA-T レーザー装置
(合計ビームタイム：232時間)

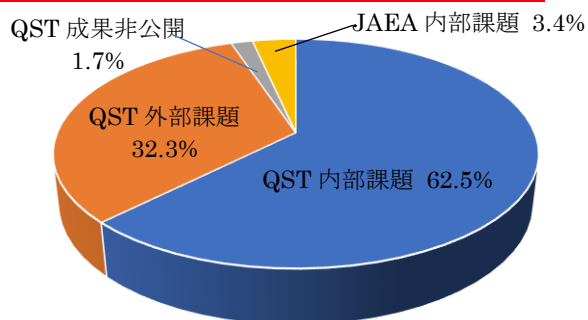


その他装置 (木津地区)
(合計ビームタイム：1390時間)



○播磨地区

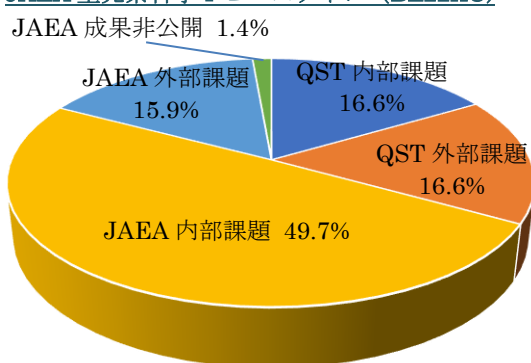
QST 極限量子ダイナミクス I ビームライン (BL11XU)



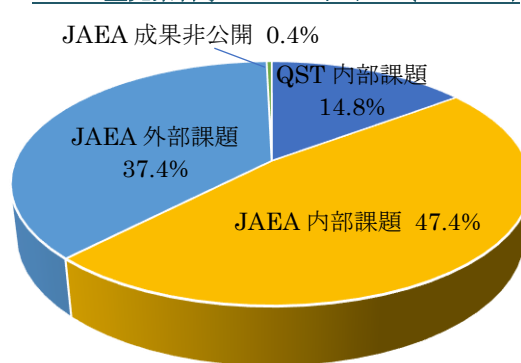
QST 極限量子ダイナミクス II ビームライン (BL14B1)



JAEA 重元素科学 I ビームライン (BL22XU)



JAEA 重元素科学 II ビームライン (BL23SU)



Research Highlights

Activities of Advanced Photon Research

Kiminori Kondo

Department of Advanced Photon Research



In the department of Advanced Photon Research, the primary research focus is the science and technology of advanced lasers. High-peak-power laser technology, high-repetition-rate and high-stability laser technology, and ultrashort-pulse technology are of particular importance. We develop these technologies in-house and apply them to various objects. The largest laser system in KPSI is the Petawatt (PW)-class high-peak-power laser J-KAREN-P. This system has been upgraded since obtaining the supplementary budget in FY2012, and the long commissioning operation term was completed two years ago. Internal users in KPSI and external users have used the system in PW-class operation mode. In this fiscal year, 30% of the total machine time has been shared to the external users. The extreme focused intensity of up to 10^{22} W/cm² on targets with extremely high-contrast suppression of the preceding optical component to the main pulse is now available. This extreme status of our high-power laser infrastructure is maintained by the laser facility operation office, advanced laser group, and high-intensity laser science group. The advanced laser group not only maintains J-KAREN-P to deliver laser pulses with the best conditions, but also develops and introduces new technology to maintain the world-leading class condition of J-KAREN-P. Dr. Miyasaka reports the development of the optically synchronized stable pump laser for optical parametric chirped pulse amplification (OPCPA) and Dr. Ogura reports the investigation on the recovery time of semiconductor saturable absorption, which is important for taking the high quality high peak power laser pulse. The high-intensity laser science group mainly studies laser-driven ion acceleration, laser electron acceleration, and relativistic high-order harmonic generation with J-KAREN-P in KPSI.

One of the most important applications is the development of a laser-driven secondary radiation source. An extremely high optical field can be formed with focusing extremely high peak power to an ultimately small spot size. Atoms and molecules exposed to this extremely high field are immediately ionized by field ionization. The corresponding optical intensity to the atomic unit is only 3×10^{16} W/cm², which is much lower than that generated with J-KAREN-P. The generated free electrons move along the extremely high optical field, then the ultra-relativistic quiver motion is induced. These energetic quivering electrons induce the generation of various secondary radiations. This means that there is a possibility of a compact energetic quantum beam source without conventional accelerator technology. If this technology is established and applied to various fields, a type of destructive innovation could occur. Dr. Dover explains the effect of small focus on electron heating and proton acceleration in ultra-relativistic laser-solid interactions, which is very important knowledge for designing the high field interaction experiment and for developing the laser driven ion accelerator. Laser driven electron acceleration is also an important topic related to this interaction. Dr. Kai describes the variation in electron emission time in weakly nonlinear laser wakefield. One of the most important applications of laser-driven energetic particles is the application to Quantum Scalpel, which is a new-generation heavy-ion cancer therapy machine planned to be developed within 7 years from now. Quantum Scalpel is one of the main projects in QST. The injector part of Quantum Scalpel is based on the laser-driven carbon accelerator. The JST-MIRAI R & D program (large-scale type) started in Nov. 2017. The aim of this program is to show a proof of concept (POC). In addition to an

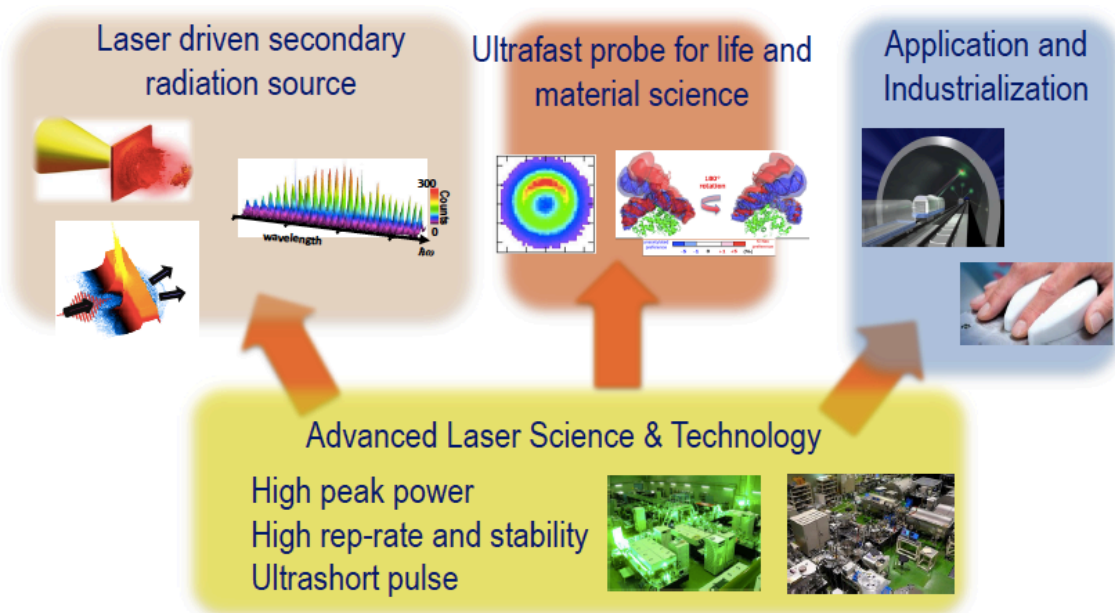


Fig. 1 Research and development of the department of Advanced Photon Research.

ion accelerator, a laser plasma electron accelerator is also under development in KPSI within the MIRAI program. Furthermore, particle acceleration and X-rays are generated with ultrashort high-peak-power lasers. Burst intensification by singularity emitting radiation (BISER) is the new laser-driven coherent X-ray generation scheme, which has been invented by KPSI. There is also a possibility of a keV-scale coherent X-ray source that doesn't use a gigantic linac like such as SACLA with BISER. The development of high repetition rate secondary sources is very important for the real application of these secondary radiation sources. In the MIRAI project, the demonstration of POC of the laser driven heavy ion injector must be shown by the end of FY2026. Therefore, the X-ray laser group once shut down the 0.1 Hz X-ray laser driver (TOPAZ) and started to develop the high quality 10 Hz X-ray laser driver. This system is established on the commercial base 10 TW/10 Hz CPA Ti:sapphire laser system. For taking the stable operation, the front end of this system is based on the 100 Hz LD pump solid state laser. By taking the double CPA structure, very high quality 30 TW laser pulses will be generated not only for 10 Hz X-ray laser operation, but also for the stable ion beam generation for the MIRAI project. As an application of the intense X-ray laser, Dr. Ishino reports the study on the mesoscopic polarization structure in the relaxor ferroelectrics $\text{Pb}[(\text{Mg}_{1/3}\text{Nb}_{2/3})_{1-x}\text{Ti}_x]\text{O}_3$.

The next important application of advanced laser science and technology is an ultrafast probe for life and material science. THz radiation is also mainly developed in the ultrafast dynamics group for material science. Until two years ago, the C-Phost project had been performed by the ultrafast dynamics group. Strong THz radiation is generated with a kHz 10-mJ ps laser system, QUADRA-T. These radiation and laser systems are used for various ultrafast dynamics research. Dr. Tsubouchi reports a study on the plane shockwave generation in liquid water using irradiation of THz pulses. Dr. Endo details the characterization of UV pulses by plasma-mirror FROG using a liquid-sheet jet of water. For life science applications, a bright and stable short pulse laser system has been developed and applied to the two-photon microscope for observing the neuron dynamics in mouse brains at NIRS. This research began to demonstrate one of the featured results by the unification of NIRS and JAEA three years ago. In

this fiscal year, for approaching a deeper component, a three-photon microscope is under development. Related to this development, Dr. Nagashima reports on the optical parametric oscillator pumped by the femtosecond Yb-doped fiber laser. Moreover, the ultrashort probe started to be upgraded to the attosecond regime to start attosecond science in KPSI. The related study of CPS laser fabrication has also been on going. These studies are supported by the Q-LEAP program which started two years ago. This project will be studied by the ultrafast dynamics group and the X-ray laser group. The X-ray laser group studies the interaction between intense X-rays and solid materials with the laser-plasma-based X-ray laser at KPSI and SXFEL at SACLA. The intense X-ray fabrication technology is an important fine structure fabrication technology, which has advanced to current laser fabrication technology. Dr. Dhin reports the strong excitation of silicone as a step towards sub-nanometer processing, which is very important for future processing.

In a sense, the most important application of our advanced laser science and technology is industrialization. In fact, from this fiscal year, the new SIP program, which follows the previous SIP program that finished two years ago, for the development of nondestructive tunnel inspection technology has started. This technology is being tested for its application to commercial technology at the venture company Photon-Labo. One of the key tools of the nondestructive tunnel inspection technology is the high-average-power high-repetition-rate intense laser technology. This technology is used for hitting the inner surface of the concrete tunnel to induce an acoustic wave inside the wall. To induce an acoustic wave of sufficient amplitude, a 5-J per pulse with a 50-Hz repetition rate system has been developed and successfully loaded onto an inspection vehicle. This technology is closely related to the development of high-average-power high-peak-power laser systems, which could be used in the laser-driven carbon ion injector in Quantum Scalpel. Medical applications are an additional important consideration. By using high power laser technology, a strong and compact infrared laser can be developed for various medical use including detecting blood glucose measurement. Additionally, Dr. Aoyama introduced the potential application to the field of pathology.

Investigation of recovery dynamics of a semiconductor saturable absorber for ultra-high-intensity lasers

Koichi Ogura

Advanced Laser Group, Department of Advanced Photon Research



The short-pulse high-intensity laser system J-KAREN-P [1] of the Kansai Institute of Photon Science is a petawatt-class laser system that can generate high-intensity light pulses with a pulse width of 30 fs, pulse energy of 40 J, and repetition rate of 0.1 Hz. The short-pulse high-intensity laser has pre-pulses. The intensity ratio between the main pulse and the pre-pulse is called a temporal contrast. The temporal contrast of J-KAREN-P is approximately 10^{12} . A high temporal contrast is required for accessing high-field physics in a desired target. The focus intensity of J-KAREN-P is up to 10^{22} W/cm². This laser system is used for high-energy ion-generation experiments [2], electron acceleration experiments [3], and X-ray harmonic generation experiments [4]. These experiments are supported by J-KAREN-P's high temporal contrast and focus intensity. The high temporal contrast is achieved by pulse cleaning methods in this laser system. One is a method with a temporal filter (a saturable absorber) and the other is a method using an optical parametric amplification method (OPCPA). Semiconductor-doped glass, RG850, is used as a saturable absorber to enhance the temporal contrast of the J-KAREN-P laser.

In this report, we report on the measurement of the recovery dynamics of the saturable absorber RG850 for a pulse cleaner. Saturable absorption is an example of a nonlinear optics effect. Saturable absorption can be described as a phenomenon where an initially dark piece of optical material becomes lighter when placed under a bright light. The saturable absorber RG850 absorbs a low-intensity pre-pulse, but transmits an intense main pulse of a short-pulse high-intensity laser beam. RG850 is a semiconductor-doped glass, being composed of a glass and small semiconductor crystals, and it has a fast response time.

RG850 is a material in which small crystalline semiconductor particles (CdS, CdTe, ZnS) are dispersed in silica-based glass. It is usually used as a color filter for light near 850 nm. The wavelength range of J-KAREN-P is around 775 nm to 825 nm with a center wavelength near 800 nm. The recovery dynamics of RG850 with a high laser intensity of 3 mJ/cm² have not reported.

The diameters of the crystals are up to approximately 100 nm. The crystal is also called a quantum dot. The crystal is made by mixing glass with the composite semiconductor material and keeping the glass at an appropriate temperature. When the quantum dots are irradiated with light, hole-electron pairs are generated in the quantum dots and recombine with a certain relaxation time.

The band gap of bulk CdTe is 1.44 eV. It corresponds to a wavelength of 861 nm. Photons with a wavelength shorter than 861 nm are absorbed. The smaller the size of a quantum dot, the larger the energy gap grows compared to the bulk band gap energy. Therefore, it is possible to absorb the light of J-KAREN-P.

The total carrier recombination lifetime is the summation of the surface recombination lifetime and bulk recombination

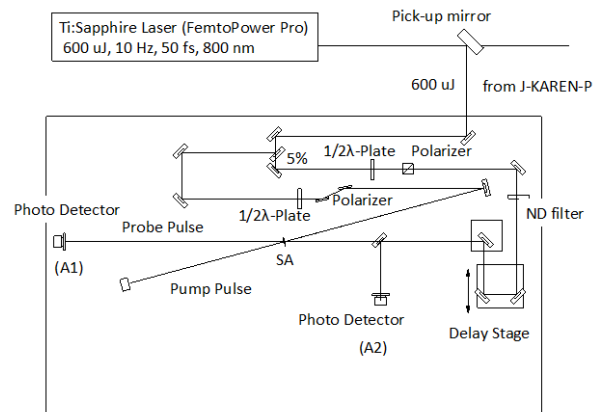


Fig. 1. Experimental setup.

lifetime [6]. The bulk recombination includes the radiative recombination and Auger recombination [6]. The bulk recombination lifetime is dependent on the carrier density, while surface recombination is not dependent on the carrier density [6]. It is related to the parameters of the semiconductor-doped glass (thermal diffusivity, *etc.*).

In this experiment, an ultrafast time-resolved pump-probe absorption technique is used to measure the time-dependent optical absorption of RG850. The experimental setup is shown in Fig. 1. In this method, the time resolution of the experiment depends on the pulse duration of the laser. In our case, the pulse duration is approximately 50 fs.

The laser (10 Hz, ~600 μ J, 50 fs) used in the experiment is a FemtoPower Compact Pro (Spectra-Physics), which is the front-end of the J-KAREN-P laser. The laser pulse was divided into pump pulses and probe pulses with a beam sampler. The energy of the pump pulse was changed with a wave-plate and polarizer system and neutral density filters.

The RG850 glass (1 inch diameter, 3 mm thickness) was irradiated with the pump beam (5 mm radius, 350 μ J energy). A delayed probe pulse was incident at the same position as the pump beam on the RG850. When the probe pulse closely followed the pump pulse (*i.e.*, with only a slight time delay), the maximum transmittance of the probe pulse was obtained. The laser was operated at 10 Hz. The RG850 glass had completely recovered within 100 ms.

The transmitted probe energy was detected with a silicon photodiode (A2). The probe pulse energy was monitored with another silicon photo diode (A1). We obtained a normalized transmitted probe pulse energy (A1/A2) from the two silicon photo detectors.

It was found that the fast recovery time constant of RG850 was approximately 10 ps and the slow recovery time constant was

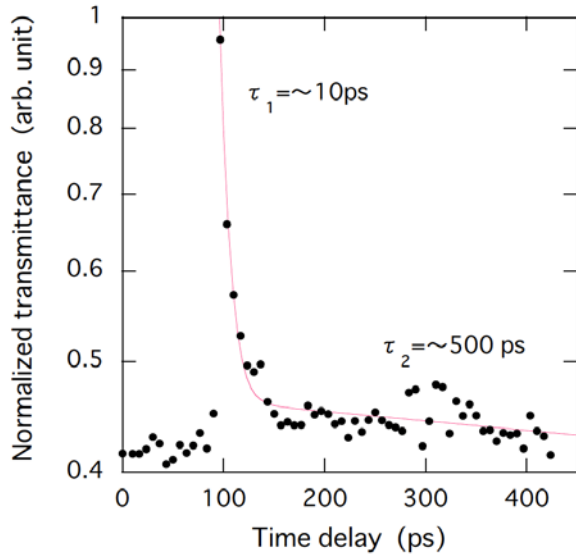


Fig. 2. Time dependence of normalized transmittance. Circles indicate experimental data. Red line is a fitted double-exponential function.

approximately 500 ps, as shown in Fig 2. Here, τ_1 corresponds to the bulk recombination lifetime and τ_2 corresponds to the surface recombination time [6]. The bulk recombination time is dependent on the carrier density. If the focus intensity increases, the bulk recombination time will decrease. However, damage to the glass might be produced at a higher focus intensity.

Acknowledgments

The author thanks H. Kiriya, Y. Miyasaka, A. Sagisaka, Y. Fukuda and A. Pirozhkov for fruitful discussions.

References

1. H. Kiriya, M. Mori, A. S. Pirozhkov, K. Ogura, A. Sagisaka, A. Kon, T. Zh. Esirkepov, Y. Hayashi, H. Kotaki, M. Kanasaki, H. Sakaki, Y. Fukuda, J. Koga, M. Nishiuchi, M. Kando, S. V. Bulanov, K. Kondo, P. R. Bolton, O. Stezak, D. Vojna, M. Sawicka-Chyla, V. Jambunathan, A. Lucianetti, and T. Mock, *IEEE Sel. Topics J. Quantum Electron (Invited Paper)* 21 (2015) 1601118.
2. A. S. Pirozhkov, Y. Fukuda, M. Nishiuchi, H. Kiriya, A. Sagisaka, K. Ogura, M. Mori, M. Kishimoto, H. Sakaki, N. P. Dover, K. Kondo, N. Nakani, K. Huang, M. Kanasaki, K. Kondo, and M. Kando: *Opt. Exp.* 25 (2017) 20486.
3. M. Nishiuchi, H. Kiriya, H. Sakaki, N. D. Dover, K. Kondo, A. S. Pirozhkov, A. Sagisaka, Y. Fukuda, K. Nishitani, T. Miyahara, K. Ogura, M. A. Alkhimova, T. A. Pikuz, A. Ya Faenov, Y. Watanabe, J. Koga, S. V. Bulanov, M. Kando, and K. Kondo: *Proc. SPIE* 10241 (2017).
4. A. S. Pirozhkov, M. Kando, T. Zh. Esirkepov, P. Gallegos, H. Ahmed, E. N. Ragozin, A. Ya. Faenov, T. A. Pikuz, T. Kawachi, A. Sagisaka, J. Koga, M. Coury, J. Green, P. Foster, C. Brenner, B. Dromey, D. R. Symes, M. Mori, K. Kawase, T. Kameshima, Y. Fukuda, I. Chen, I. Daito, K. Ogura, Y. Hayashi, H. Kotaki, H. Kiriya, H. Okada, N. Noshimori, T. Imazono, K. Kondo, T. Kimura, T. Tajima, H. Daido, P. Reajeev, P. McKenna, M. Borghesi, D. Neely, Y. Kato, and S. V. Bulanov: *New J. Phys.* 16 (2014) 093003.
5. M. A. Alkhimova, A. Y. Faenov, I. Y. Skobel, T. A. Pikuz, M. Nishiuchi, H. Sakaki, A. S. Pirozhkov, A. Sagisaka, N. P. Dover, K. Kondo, K. Ogura, Y. Fukuda, H. Kiriya, K. Nishitani, T. Miyahara, Y. Watanabe, S. A. Pikuz, M. Kando, R. Kodama, and K. Kondo: *Opt. Express* 25 (2017) 29501.
6. P. Srikrishna, "Dynamics of saturable absorption in the semiconductor-doped glass RG850" (2015) *College of Science and Health Theses and Dissertations*. 115.

Optically synchronized stable pump laser for optical parametric chirped pulse amplification

Yasuhiro Miyasaka



Advanced Laser Group, Department of Advanced Photon Research

The J-KAREN-P laser adopts the optical parametric chirped pulse amplification (OPCPA) as a pre-amplifier to achieve high temporal contrast [1]. Pulse energy is transferred from a pump pulse to a signal pulse by the optical parametric process if both the pulses exist simultaneously in a non-linear optical crystal under phase matching conditions. Reduction of timing jitter between the pump and signal pulses for the OPCPA is a key issue when obtaining stable amplified pulse energy and spectrum. The main source of sub-ns ~ ns timing jitter is electrical synchronization of different laser oscillators for pump and signal pulses. The timing jitter can be suppressed to less than 1 ps by optically synchronized OPCPA, which uses a single oscillator to eliminate the electrical timing jitter [2]. Pulse durations of 1-100 ps for the optically synchronized pump lasers generated from signal pulses have been reported because the pump pulses are developed for lasers with low-energy and few-cycles [3]. The pulse duration of signal pulses at the J-KAREN-P laser is stretched to ~1ns to avoid optics damages in subsequent amplifiers. An optically synchronized pump laser with a long pulse duration is desired for a more stable operation of the OPCPA in the J-KAREN-P laser. In this study, newly developed optically synchronized stable pump lasers with a maximum pulse duration of 330 ps at a wavelength of 532 nm is reported.

A schematic setup of the optically synchronized pump laser is shown in Fig. 1. Pulses from a Ti:sapphire oscillator (7 fs pulse duration and 80 MHz repetition rate) are focused into a photonic crystal fiber for spectrum broadening by the soliton self-frequency shift (SSFS) to obtain a wavelength of 1064 nm. The spectrum broadening depends on the intensity of the input pulse [4]. The intensity of the 1064 nm pulse is stabilized by an originally constructed feedback system, which is composed of a spectrometer and a half-wave plate mounted on a motorized rotation stage. Figure 2 shows the measured stability of the center wavelength with and without the feedback control. Here, the center wavelength is defined by the peak Gaussian fitting to the extended spectrum of around 1064 nm. The fluctuation of the center wavelength is stabilized to 0.2 nm (0.02%, RMS) over 2 hours by controlling the half-wave plate angle. The stabilized pulses are amplified to 130 mW by four stage Yb: fiber amplifiers, and are stretched to 1 ns by chirped fiber Bragg grating. Stability of the fiber output power is better than 0.2 % (rms) over 3 hours

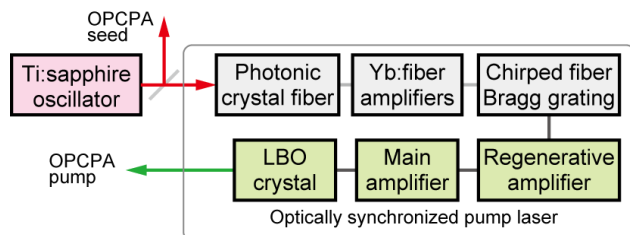


Fig. 1. Schematic setup of the optically synchronized pump laser.

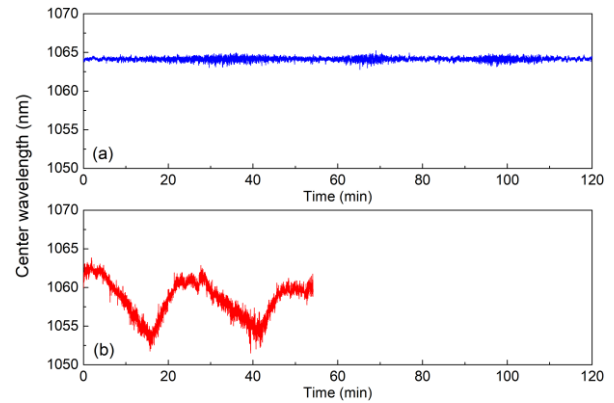


Fig. 2. Dependence of the center wavelength on time (a) with and (b) without the feedback control system.

with the feedback system. The fiber output pulses are collimated to a diameter of ~2 mm by an achromatic lens, and picked up by the Pockels cell to 10 Hz for amplification in the laser diode-pumped Nd:YAG regenerative and 2-pass main amplifiers. The regenerative amplifier is designed to set a beam diameter of ~2 mm on the Nd:YAG rod to avoid Fresnel diffraction from the rod edge. The input pulses are amplified to ~20 mJ after 10 round trips. The small signal gain per 1 round trip is as high as ~9. The stability of the amplified pulse energy is measured to be 0.3% (rms) over 2 hours. The output beam profile with a diameter of 2.3 mm at the intensity point, $1/e^2$, is obtained with a good Gaussian profile. The stably amplified pulses are sent to a 2-pass main amplifier after expanding the beam diameter to 4 mm at the intensity point, $1/e^2$. A serrated aperture with a diameter of 5 mm is placed after the beam expander to avoid Fresnel diffraction. The pulses are amplified to 200 mJ with the main amplifier with a stability of better than 0.2 % (rms) over 2 hours. The beam

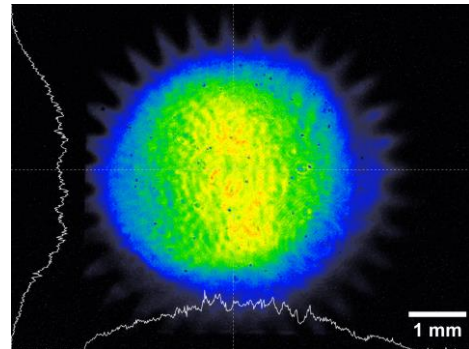


Fig. 3. Beam profile at 532 nm.

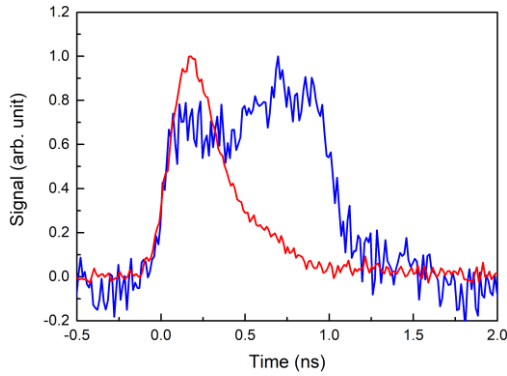


Fig. 4. Measured pulse duration (blue) before regenerative amplifier and (red) after frequency doubling.

profile on the serrated aperture is relayed to an LBO crystal to obtain a high efficiency of frequency doubling. The frequency doubled (532 nm) pulse energy is 130 mJ with a stability of 0.6 % over 2 hours. Figure 3 shows the 532 nm beam profile in the LBO crystal. The triangle shape surrounding the profile is the shadow of the serrated aperture. The center part on the profile at 532 nm is slightly stronger in the vertical direction. The pulse duration is measured by a 30 GHz oscilloscope and a biplanar phototube with the rise time of 60 ps. The pulse duration at the output of the fiber system is ~ 1 ns (FWHM), which corresponds to the specification of the FBG. However, the pulse duration becomes shorter after frequency doubling, as shown in Fig. 4. We consider that much of the pulse shortening is due to the waveform

distortion behavior of high gain amplification in the regenerative amplifier. After frequency doubling, the pulse duration of 330 ps (FWHM) is obtained at 532 nm. Further improvement of the pulse duration is needed to fully meet the J-KAREN-P system requirement.

Acknowledgments

The author thanks KIRIYAMA Hiromitsu, KISHIMOTO Maki, MORI Michiaki, KONDO Kotaro, KANDO Masaki and KONDO Kiminori for their sincere contributions.

References

1. H. Kiriya, A. S. Pirozhkov, M. Nishiuchi, Y. Fukuda, K. Ogura, A. Sagisaka, Y. Miyasaka, M. Mori, H. Sakaki, N. P. Dover, K. Kondo, J. K. Koga, T. Z. Esirkepov, M. Kando, and K. Kondo, "High-contrast high-intensity repetitive petawatt laser," *Optics Letters* **43**(11), 2595-2598 (2018).
2. C. Y. Teisset, N. Ishii, T. Fuji, T. Metzger, S. Köhler, R. Holzwarth, A. Baltuška, A. M. Zheltikov, and F. Krausz, "Soliton-based pump-seed synchronization for few-cycle OPCPA," *Optics Express* **13**(17), 6550-6557 (2005).
3. A. Vaupel, N. Bodnar, B. Webb, L. Shah, and M. Richardson, "Concepts, performance review, and prospects of table-top, few-cycle optical parametric chirped-pulse amplification," *Optical Engineering* **53**(5), 051507 (2014).
4. N. Ishii, C. Y. Teisset, S. Köhler, E. E. Serebryannikov, T. Fuji, T. Metzger, F. Krausz, A. Baltuška, and A. M. Zheltikov, "Widely tunable soliton frequency shifting of few-cycle laser pulses," *Phys. Rev. E* **74**, 036617 (2006).

Variation in electron emission time in weakly nonlinear laser wakefield acceleration



Kai Huang

High Intensity Laser Science Group, Department of Advanced Photon Research

Laser wakefield acceleration (LWFA) [1] is one of the most intensively studied fields in high energy density science (HEDS) because of the inherent high acceleration gradient and ultrashort acceleration structure. The secondary radiation sources [2] from LWFA possess the temporal characteristics of the accelerated electrons and are considered to be useful in the application of ultrafast pump-probe studies. The resolution of a pump-probe study is determined by the duration and jitter of the probe pulse. The single bunch duration of LWFA has been demonstrated to be at femtosecond (fs) level [3], which is consistent with the micrometer-scale wave bucket. For the aspect of timing jitter, it is assumed that the electrons are to be injected into the first bucket of the wakewave in the bubble regime [4]. Thus, they are always considered to be “jitter-free”. However, up to now, the timing information of laser wakefield accelerated electrons have not been real-time monitored. For theoretic concern, since laser wakewave is composed of a sequence of buckets, the possibility of electrons being injected into lateral buckets cannot be ignored. This issue has been paid little attention experimentally.

For the timing monitoring of electron beams, electro-optic (EO) sampling techniques have been widely used in conventional accelerators [5]. When an electron bunch passes by an EO crystal, the coulomb field residing in THz range acts as a DC bias. A probe laser propagating through the crystal will undergo Pockels effect, causing polarization rotation that records the electron temporal profile. This technique has the advantages of non-destructive and single-shot detection. By setting an angle between the propagation direction of the probe laser with the electron beam path, the electron longitudinal information can be transversely encoded to the laser profile. This is known as the “electro-optic (EO) spatial decoding technique”.

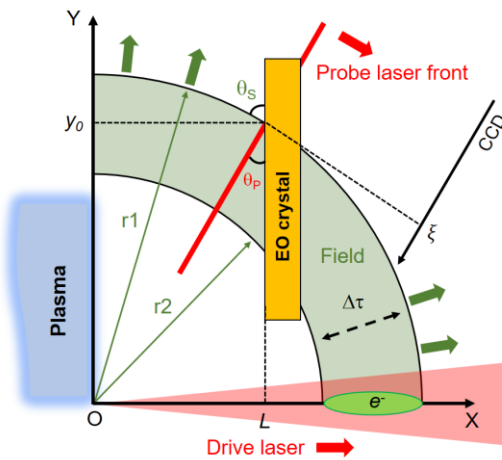


Fig. 1: EO spatial decoding model. The wavefront of the Coulomb field has a spherical shape with the center at the exit of plasma.

In a previous study, we introduced EO spatial decoding

technique to the LWFA study and discussed the methodology in detail [6]. We found that when placing the crystal very close to the plasma source, the wave-front of the Coulomb field had a spherical shape instead of the perpendicular plane wave model that was previously widely used. For such a special case, we derived a modified temporal mapping relationship: $c\Delta\tau = (1 + \sin\theta_s / \sin\theta_p) \cdot \tan\theta_p \Delta\xi$, where $\Delta\xi$ and $\Delta\tau$ represent the observed displacement on the CCD and the corresponding time difference, respectively. θ_s and θ_p are the incident angles of the Coulomb field and probe laser on the EO crystal surface, as illustrated in Fig. 1.

In this report, we present the observation of the plasma density dependent electron emission time variation by using the EO spatial decoding technique. The emission times of the electrons tended to be earlier with higher plasma densities, corresponding to a closer injection position relative to the drive laser pulse. The timing trend fitted well with a density down-ramp injection model. Our study suggests that for weakly nonlinear laser wakefield acceleration, jitter issues should not be ignored.

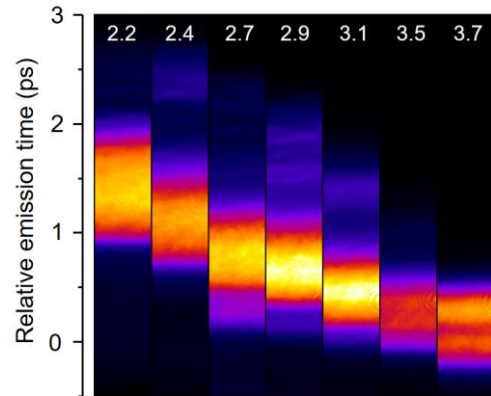


Fig. 2: Single shot EO signals vs. densities. The cases with plasma densities of {2.2, 2.4, 2.7, 2.9, 3.1, 3.5, 3.7} $\times 10^{19} \text{ cm}^{-3}$ are listed from left to right. Signals were generated from pure He gas. Multi-bunch structures were observed frequently at slightly higher plasma densities.

The experiment was performed with the JLITE-X laser system at the Kansai Photon Science Institute (KPSI), National Institutes for Quantum and Radiological Science and Technology (QST), Kyoto, Japan. In the experiment, the laser output is 4 TW with a pulse duration of 40 fs. The laser intensity on target was $I = 7 \times 10^{17} \text{ W/cm}^2$, corresponding to a normalized vector potential $a_0 \sim 0.57$, where $a_0 \sim 8.6 \times 10^{-10} \lambda_0 [\mu\text{m}]^{1/2} [\text{W/cm}^2]$. A 3 mm conical nozzle was used for electron generation. The crystal we used was a 50 μm thick GaP crystal placed at a position $(L, y_0) = (2.2 \text{ mm}, 1.5 \text{ mm})$ downstream of the exit of the target, see Fig. 1. The probe incident angle on the crystal surface was set to be $\theta_p = 44^\circ$.

A list of single-shot EO signals from pure helium (He) gas is shown in Fig. 2. With a moderate laser power of 4 TW, the laser wakefield acceleration worked in a weakly nonlinear mode. At higher plasma densities, the electron beams had earlier emission times. The signals had differences of nearly 1 picosecond (ps) for cases between the lowest and highest plasma density. Since the observed EO signal represented the relative timing of when the electron exited the plasma, the emission timing variation suggests that the injection position relative to the drive laser pulse varied with plasma densities. Since the detection was conductible in real-time, temporal multi-bunch structures were observed frequently during the experiment with much less efforts compared to previous literatures [7, 8].

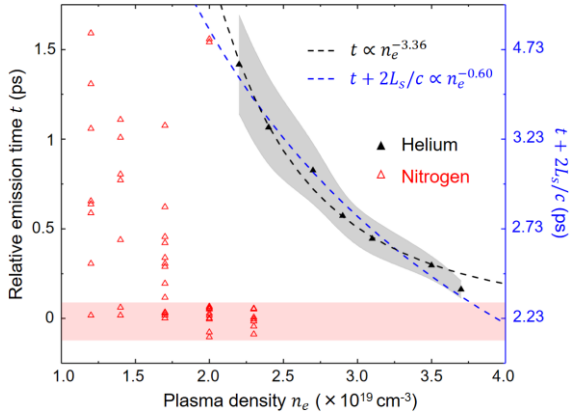


Fig. 3: Discussion of the density dependent emission time variation. The centers of the EO signals from He are illustrated by black solid triangles. The grey shadow in the figure denotes the standard deviation of the relative emission time at each density. The black and blue dashed curves are allometric fittings between $\{t, n_e\}$ and $\{t + L_s, n_e\}$, where $L_s = 484 \mu\text{m}$ is the measured plasma scale length of the density down ramp at the exit of the gas nozzle. The red triangles are the scattering plots of the peak of the signals from N_2 for background plasma densities of $\{1.2, 1.4, 1.7, 2.0, 2.3\} \times 10^{19} \text{ cm}^{-3}$. The signals in the red zone were taken as samples for relative “zero” timing determination.

To search for the physics behind the observed phenomena, we conducted statistics of 20 consecutive shots at each plasma density for pure He gas. The statistics and analysis are shown in Fig. 3. In the self-injection regime, the electron timing fluctuation decreased from 275 fs to 48 fs when increasing the density, as denoted by the black shadow. It suggested that wave breaking was forced to occur at higher plasma densities. We considered two candidate mechanisms [9, 10] which could be responsible for the observed emission time trend: (1) For the transverse wave breaking mechanism, the wave breaking timing relative to the drive laser has a relation with the density as: $t \propto n_e^{-5/6}$. However, a direct fitting between t and n_e showed $t \propto n_e^{-3.36}$ (see black dashed line in Fig. 3), which was far from the transverse wave breaking model. (2) For the density down-ramp injection mechanism, the relative injection timing is related with the density as: $t + 2L_s/c \propto n_e^{-2/3}$, which fitted well with the

experimental data, as illustrated by blue dashed line (with index of -0.60) in Fig. 3. The analysis showed that the density down-ramp might be responsible for the injection of the majority of electrons and the observed timing trend in our experiment [11].

The relative zero timing was determined by the using the nitrogen (N_2) gas target when ionization injection occurred. Simulations demonstrated that high energy electrons were injected into the first bucket at a background plasma density of $2.0 \times 10^{19} \text{ cm}^{-3}$ for the laser parameters used in the experiment [11]. Additionally, the experimental results of N_2 showed different timing behavior compared to that of He. At each plasma density, there were signals appearing near the “zero” timing. At plasma densities of $< 2 \times 10^{19} \text{ cm}^{-3}$, the EO signals covered a large range of timings. At $2.0 \times 10^{19} \text{ cm}^{-3}$, except for two shots with very late timings, the others were constrained in a region near the zero timing. At $2.3 \times 10^{19} \text{ cm}^{-3}$, no signals were observed with late timings. Based on both experiments and simulations, we take the mean timing value in the red zone in Fig. 3 as the relative zero emission time.

In summary, by introducing the EO spatial decoding technique to the experimental research of LWFA, we observed the plasma density dependent electron emission time variation in the weakly nonlinear condition. Measurements indicated that, in some occasions of LWFA, the electrons were not necessarily “jitter-free”. For application concerns, controlled injection mechanisms should be used to generate temporally stable electron bunches. The detection method in this report will be optimized for single-shot detailed measurement of the electron temporal profile and the investigation of the physics in the injection and acceleration processes.

Acknowledgments

The author acknowledges Prof. A. Zigler, Prof. P. Bolton, and Dr. A. Pirozhkov for fruitful discussions, and Prof. Hosokai and Dr. Sano for their encouragement. M. Kando conceived the research. H. Kotaki, M. Mori, Y. Hayashi, N. Nakanii, and M. Kando joined the experiment. T. Esirkepov, J. K. Koga, and S. V. Bulanov provided the theoretical supports. This work was funded by the ImPACT Program of the Council for Science, Technology and Innovation (Cabinet Office, Government of Japan) and the JST-Mirai Program Grant No. JPMJMI17A1, Japan.

References

1. T. Tajima and J. M. Dawson, *Phys. Rev. Lett.* 43, 267 (1979).
2. K. Huang et al., *Sci. Rep.* 6, 27633 (2016).
3. O. Lundh et al., *Nat. Phys.* 7, 219 (2011).
4. W. Lu et al., *Phys. Rev. Lett.* 96, 165002 (2006).
5. B. Steffen et al., *Phys. Rev. Accel. Beams* 12, 032802 (2009).
6. K. Huang et al., *Sci. Rep.* 8, 2938 (2018).
7. M. Heigoldt et al., *Phys. Rev. Accel. Beams* 18, 121302 (2015).
8. J. van. Tilborg et al., *Phys. Rev. Lett.* 96, 014801 (2006).
9. S. V. Bulanov et al., *Phys. Rev. Lett.* 78, 4205 (1997).
10. S. V. Bulanov et al., *Phys. Rev. E* 58, R5257 (1998).
11. K. Huang et al., *Phys. Rev. Accel. Beams* 22, 121301 (2019) (Editors’ Suggestion).

Effect of small focus on electron heating and proton acceleration in ultra-relativistic laser-solid interactions



Nicholas P. Dover

High Intensity Laser Science Group, Quantum Beam Science Directorate,
Kansai Photon Science Institute

State-of-the-art high-power lasers can now reach up to ~ 1 PW level and can be focused to intensities nearing 10^{22} W/cm². The resulting fields are so strong that the accelerating gradients are almost a billion times higher than those typically used in conventional particle accelerators. When such high intensities are focused onto solids, the fields strip electrons from the ions and accelerate them to relativistic energies within femtoseconds. The way in which the laser transfers energy to electrons, and the properties of the accelerated electrons, is a fundamental building block for numerous scientific applications, such as compact ion [1], x-ray [2], neutron [3] and for next-generation lasers, and gamma ray sources [4].

The electron acceleration by the laser is analytically difficult to calculate due to the complicated field structure caused by the tight focusing of the laser, the reflection of the laser from the front side of the target, and the electric and magnetic fields induced in the plasma at the front surface. The heated electrons typically have a thermal spectrum and are characterized by their temperature T_e . A number of simple analytical scaling laws have been developed to predict the variation of T_e with laser intensity I_L . One commonly used law is ponderomotive scaling, which estimates temperature to be equal to the electron transverse quiver energy in a plane wave [5]. Other scaling laws differ in details, but all of them predict that the electron temperature only depends on laser intensity, with no dependence on other laser parameters such as focal spot size. As there are only few experimental studies at relativistic intensities, and no reports from the current high intensity frontier, above 10^{21} W/cm², it is important to measure this experimentally. Furthermore, many applications also depend on other beam parameters such as the electron beam divergence, which has also not been clarified.

One important application that is dependent upon the parameters of the electron beam is the laser driven ion source, which can produce ultra-high peak current ion beams with very different properties compared to conventional sources. Sheath acceleration is one common mechanism that drives these sources. It involves the laser being focused onto a thin (~ 1 μm) foil. The laser accelerated electrons flow away from the focal spot into the target and, when reaching a target surface, generate a strong quasi-electrostatic space charge field that accelerates surface ions. As the electrons mediate the ion acceleration, it is of great interest to experimentally observe both the electron and ion beam and investigate the scaling to the highest intensities currently possible.

We investigated the acceleration of electrons and protons from ultra-high intense laser interactions with thin solid foils, as described in [6]. We found, for the first time, that the electron temperature depended not only on laser intensity but also on focal spot size, an effect which is only apparent at ultra-high laser intensities. We showed that for extremely small focal spots the electron cannot be accelerated over a sufficiently long distance to

gain a lot of energy, even though the accelerating fields may be higher. We also showed only a weak improvement in proton acceleration when using very tight focal spots due to a reduction in the acceleration time. Therefore, we have shown that further improvement of particle heating in laser-solid interactions may require higher laser energy, not just higher laser intensity.

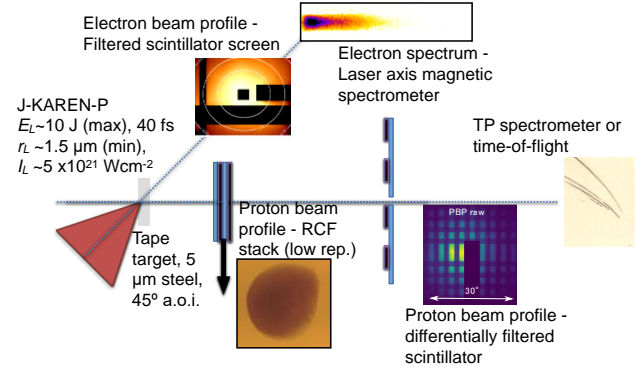


Fig 1: Experimental set-up of experiment at J-KAREN-P.

The experiment was performed at the J-KAREN-P facility at Kansai Photon Science Institute, QST, Japan [7, 8], as shown in Fig 1. The J-KAREN-P laser was focused onto a tape target with a 5 μm steel target which could be reeled to provide a new target for each shot, matching the laser repetition rate of 0.1 Hz. The contrast of the laser was measured using a 3rd order cross correlator, and was used to simulate the prepulse expansion using a hydrodynamics code (FLASH), showing the formation of a double-scale length plasma gradient at the front surface with exponential scale lengths of ~ 0.5 μm and 4 μm respectively [6]. The generated electron beam was measured using a filtered scintillator screen to observe the beam profile, and a magnetic spectrometer placed exactly along the laser's axis. The proton beam was measured by either a radiochromic film stack (RCF) at low repetition, or a combination of a scintillator diagnostic and a time-of-flight diagnostic measuring the beam profile [9] and the maximum proton energy, respectively.

The electron temperature as a function of intensity was measured in two different ways: firstly, with the smallest focal spot possible ($r_L = 1.5$ μm) and by varying the laser energy E_L on the target between ~ 1 J and 10 J, and secondly, by keeping the laser energy at 10 J and varying the target position with respect to laser focus, effectively changing the focal spot size r_L . The results are shown in Fig. 2a, along with the predictions from ponderomotive scaling. Although there is a reasonably good agreement between the experimental measurement and the ponderomotive scaling theory at low intensities and large focal spots, at high intensities the temperature appears to be suppressed compared to the scaling. Furthermore, there appears to be a

significant difference between the temperature for a fixed intensity when varying focal spot size or laser energy. In particular, the small focal spot size appears to result in a reduced temperature for the same intensity, which was not predicted by ponderomotive scaling or any other proposed electron temperature scaling law.

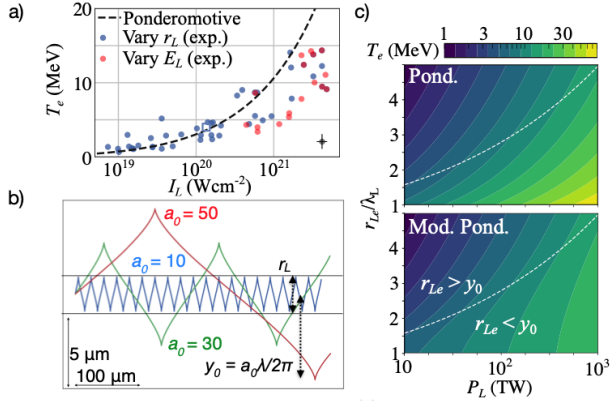


Fig 2: a) Scaling of electron temperature with intensity for varied focal spot size r_L and laser energy E_L , b) diagram showing electron motion in a plane wave for different normalized vector potentials, and the equivalent focal spot size, and c) predictions of our modified scaling model compared to the ponderomotive prediction as a function of laser power and focal spot size, where the white dotted line indicates the divergence of the two models. The experimental data used is the same as that published in [6].

To understand why this might be, firstly consider the trajectory of an electron being accelerated in a plane wave (Fig 2 b.). As the laser intensity, and the related normalized vector potential a_0 , increases, the distance travelled by the electron in a single cycle also increases. That is, even though the potential maximum quiver energy is higher, the electron needs a longer distance to reach that maximum energy. As shown for the experimental maximum intensity ($I_L = 5 \times 10^{21}$ Wcm⁻², $a_0 = 50$), the acceleration length far exceeds the focal spot size (given by the horizontal dotted lines). It is possible to analytically estimate the energy the electron can gain before it leaves the focal spot within the ponderomotive scaling framework (see [6] for details). Comparing ponderomotive scaling (top) and our new scaling (bottom), the resulting temperature suppression is shown in Fig. 2c. Above the point where the plane wave transverse acceleration length y_0 exceeds the $1/e$ focal spot size r_{Le} , the new scaling is identical to ponderomotive scaling (white dotted line). However, below this, the temperature is heavily suppressed, creating a stringent limit on the energies that the laser-heated electrons can reach. The predictions of the modified model in our experimental conditions at maximum intensity is ~ 12 MeV, which is in excellent agreement with the experimental results and numerical particle-in-cell simulations performed to elucidate the experiments.

We also measured the proton beam that was generated from the interaction and compared it to well-known scales [6]. At the highest intensity, the protons were accelerated up to energies of

30 MeV by the sheath acceleration mechanism. We varied the intensity in the same manner as described for the electrons above. There was a relatively good agreement with the electrostatic model developed by Schreiber [10] when varying the laser energy without the manipulation of any free parameters in the model. However, the scaling to larger focal spots underestimated the energies by orders of magnitude. We concluded that the Schreiber model was underestimating the acceleration time for larger focal spots. When the focal spot and the corresponding sheath is very small, the electrons that bounce back-and-forth between the front and rear surface only contribute once to the sheath. However, if the sheath is large, the same electron can contribute multiple times to the sheath, resulting in an effectively higher sheath lifetime. Therefore, there is an effective increase in the acceleration time with increasing focal spot size, so although the sheath field weakens significantly with decreasing intensity, it is partially compensated by the increasing acceleration time. We modified the acceleration time used in the Schreiber model to account for this and found significantly improved predictions of the experimental data.

In conclusion, we experimentally measured the effect of using a very small focal spot size to maximize laser intensity on the accelerated electron and proton beams. In both cases we found only a marginal improvement from using extremely tightly focused laser pulses. This creates an increase in the laser energy instead of decreasing the laser spot size as a method of boosting the parameters of the generated particle beams. This work is described in more comprehensive detail in the main manuscript [6].

Acknowledgments

The author would like to thank all the co-authors on the paper: M. Nishiuchi, H. Sakaki, Ko. Kondo, M. A. Alkhimova, A. Ya. Faenov, M. Hata, N. Iwata, H. Kiriya, J. K. Koga, T. Miyahara, T. A. Pikuz, A. S. Pirozhkov, A. Sagisaka, Y. Sentoku, Y. Watanabe, M. Kando and K. Kondo. The author is also grateful to the J-KAREN-P operations team for their support. This work was supported by a JSPS Postdoctoral Fellowship and Kakenhi project No. 15F15772, and partially supported by JST PRESTO Grant Number JPMJPR16P9 and Kakenhi 10K05506. The EPOCH code was in part funded by the UK EPSRC Grant Nos. EP/G054940/1, EP/G056803/1, EP/G055165/1 and EP/M022463/1. FLASH was developed by the DOE NNSA ASC and NSF-supported FCCS at the University of Chicago.

References

1. H. Daido *et al.*, Rep. Prog. Phys. **75**, 056401 (2012)
2. C. M. Brenner *et al.*, Plasma Phys. Contr. F. **58**, 014039 (2016)
3. M. Roth *et al.*, Phys. Rev. Lett. **110**, 044802 (2013)
4. C. P. Ridgers *et al.*, Phys. Rev. Lett. **108**, 165005 (2012)
5. S. C. Wilks *et al.*, Phys. Rev. Lett. **69**, 1383 (1992)
6. N. P. Dover *et al.*, Phys. Rev. Lett., **124**, 084802 (2020)
7. H. Kiriya *et al.*, Opt. Lett. **43**, 2595 (2018)
8. A. S. Pirozhkov *et al.*, Opt. Express **25**, 20486 (2017)
9. N. P. Dover *et al.*, Rev. Sci. Instrum. **88**, 073304 (2017)
10. J. Schreiber *et al.*, Phys. Rev. Lett. **97**, 045005 (2006)

Mesoscopic hierarchic polarization structure in the relaxor ferroelectrics PMN-x% PT



Masahiko Ishino

X-ray Laser Group, Department of Advanced Photon Research

Those studying relaxor ferroelectrics have been interested in their large dielectric response and utility for many dielectric devices. The advantageous properties of $\text{Pb}[(\text{Mg}_{1/3}\text{Nb}_{2/3})_{1-x}\text{Ti}_x]\text{O}_3$ (PMN-x% PT) have resulted in it becoming a popular material that has attracted interest [1]. It is well known that some macroscopic properties of a solid can never be resolved by simply considering the microscopic nature of the crystal structure and electronic states, instead originating inherently in the mesoscopic level hierarchy [2]. Mesoscopic polarization structures such as polar nanoregions (PNRs) [3] and polarization domain walls [4] are certainly of this form, connecting microscopic fundamental polarization structures with macroscopic practical dielectric properties.

The structural symmetry of PMN-x% PTs in the paraelectric phase is cubic; however, structural symmetry in the ferroelectric phase varies depending on PT concentration [5]. The structural symmetry in the ferroelectric phase around room temperature changes from rhombohedral to monoclinic and finally changes to tetragonal as the PT concentration increases. The morphotropic phase boundary (MPB) region appears between 31% PT and 37% PT concentration [6, 7]. It was reported that PNRs appear in PMN-x% PT below 30% PT and increase in size as the concentration of PT increases. Close to room temperature, the sizes of PNRs were estimated to be 1.3, 3.4, and 35 nm for 0%, 10%, and 20% PT samples, respectively [8]. The disappearance of the diffuse scattering indicates the appearance of long-range ferroelectric order, which is associated with macroscopic polarization domains [9]. Micrometer size macrodomains have been observed in PMN-30% PT samples at room temperature [10].

The origin of a large dielectric response for PMN-x% PT observed in the MPB region has been assigned to the polarization rotation [11]. Matsushita et al. observed a sudden sharp enhancement of the dielectric response around a PT concentration of 28%; however, the origin of this anomalous dielectric response is yet to be resolved [12]. The lower vicinity of the MPB region, where the PT concentration ranges from 28 to 30%, is a singular region, where PNRs disappear and polarization domains appear. A sudden increase in dielectric constants in this region cannot be explained by the polarization rotation model as applied to monoclinic phase, as the crystal symmetry in this region is the rhombohedral. Another mechanism is needed that is inherently based on the mesoscopic nature of the polarization structure. Cooling rate dependences of dielectric properties and domain size around 30% PT samples were reported in [23, 14]. Changes in ferroelectric domain walls with sample temperature were also investigated [15]. The motion of the domain boundary in dielectrics would contribute to its dielectric response [16]. Thus, the evolution of the mesoscopic secondary polarization structures of PMN-x% PT around 28% PT in cooling is crucially important for understanding the hierarchic nature of the relevant anomalous dielectric properties.

In the present study, we investigated the temperature evolution of domain structures at just below the MPB region under two different cooling rates: the thermal equilibrium

condition and the non-equilibrium condition [17]. PMN-x% PT samples with 26.6% PT, 27.8% PT, and 28.3% PT were grown in the [110] direction. The temperature T_m at which the dielectric constant of the sample attained its maximum (measured by an external field of 1 kHz) was 412 K for PMN-26.6% PT, 418 K for PMN-27.8% PT, and 421 K for PMN-28.3% PT, respectively. The structural symmetry of the PMN-26.6% PT sample crystal only transformed from cubic to rhombohedral at the structural phase transition temperature T_C . The structural symmetry of the PMN-27.8% PT and PMN-28.3% PT sample crystals varied from cubic to tetragonal at T_C , and the tetragonal symmetry transformed again to rhombohedral at the secondary transition temperature T_r . The appearance of the ferroelectric phase in the PMN-27.8% PT sample was confirmed by x-ray diffraction and capacitance measurements. The structural changes and the dielectric behaviors around the structural phase transition temperatures coincided. We confirmed the appearance and growth of polarization domains by speckle measurements using a coherent soft x-ray laser (SXRL) pulse. The SXRL beam is a suitable tool for investigating the fluctuation of the polarization domains using the picosecond speckle technique through the birefringence.

We observed speckle patterns for PMN-26.6% PT, PMN-27.8% PT, and PMN-28.3% PT samples observed at temperatures of 428 K (above T_m), 398 K (between T_m and T_r), and 353 K (below T_r) during cooling. The speckle patterns for PMN-26.6% PT at each temperature did not change, while the speckle patterns for PMN-27.8% PT and PMN-28.3% PT varied with temperature, which means that the visible polarization domains change their size and shape with temperature. The autocorrelation pattern obtained from the speckle pattern of PMN-28.3% PT showed few large domains. In contrast, the autocorrelation pattern of PMN-27.8% PT revealed ordered oblique stripe domains. Hereafter we concentrate on the investigation on the origin and the behavior of these ordered oblique stripe domains observed at PMN-27.8% PT.

Figure 1(a) and 1(b) show two series of observed coherent SXR speckle patterns for the PMN-27.8% PT at four different temperatures below T_C during cooling, which are for the thermal non-equilibrium and equilibrium conditions, respectively. Speckle patterns reflect the evolution of the distributions of polarization domains because the origin of the soft x-ray speckles is birefringence, and information on domain sizes and adjacent domain distances can be evaluated from a spatial autocorrelation function. Figure 1(c) and 1(d) show spatial images of autocorrelation functions derived from the speckle patterns shown in Figure 1(a) and 1(b), respectively. Irregularly shaped polarization domains, which appeared just below the phase transition temperature (403 or 402 K), evolved into oblique stripe-shaped periodic structures toward the [-110] direction. These domains are 90° domains with polarization directions of [010] and [100], which are parallel and perpendicular to the polarization of the incident SXRL beam. The domain shapes in Figure 1(c) are irregular and the domain boundaries are unclear. However, domain boundaries in Figure 1(d) become clear and the

width of each domain becomes narrower as the sample temperature decreases.

In PMN-29.5% PT, an appearance of excess heat capacity was reported [18]. The excess heat capacity means the existence of additional entropy. The evolution of stripe-shaped domains observed in PMN-27.8% PT during cooling in a thermal equilibrium condition can be recognized as a self-assembly process for polarization domains accompanied by a release in entropy. When the sample temperature decreases in the thermal equilibrium condition, fluctuations of polarizations are small, causing the presence of the stripe-shaped 90° polarization domains with narrower widths and sharp boundaries.

A simulation study indicated that the compressive strain induces an active fluctuation in the oblique 90° domain wall [4]. On application of an external electric field to the [010] direction, deformation of the unit cell takes place. Lattice constants in the (001) plane begin to elongate to the [010] direction and shrink to the [100] direction. As a result, compressive strain takes place toward [100] within the (001) plane. The stripe-shaped domain wall becomes easy to move by an external electric field. When an external electric field is applied to the [010] direction, the domain area relevant to the polarization direction increases. In this case, the domain wall shifts reversibly with little increase in free energy [19]. If the polarization area increases by the antiphase shift of parallel domain wall pairs and the ferroelectric thin films [20], the increase in the excitation energy of the polarization is suppressed as there is no need for the creation of new domain walls in this mode.

A schematic drawing of this situation is shown in Figure 2. A pair of domain walls faces the antiphase shift keeping with flat boundaries at the application of electric field. In this mode, relaxation of elastic strain is almost preserved while the electrostatic energy is reduced. If the shift of domain wall pairs occurs as a collective mode due to an external alternative electric field, then the suppressed shift energy of wall pairs is further decreased. Strong enhancement in dielectric coefficients in PMN-x% PT around a PT concentration of 28% can be recognized as evidence for collective excitation of the oblique 90° domain wall pairs when an external alternative electric field is applied. This peculiar response of the polarization domain walls to an external electric field is recognized as evidence for the hierarchical characteristics of the relevant mesoscopic polarization structure.

Acknowledgments

The synchrotron radiation experiments were performed at BL22XU of SPring-8 with the approval of the Japan Synchrotron Research Institute (JASRI) (Proposal No. 2012B3713). This work was supported by a JSPS Grant-in-Aid for Scientific Research (C) (Grant No. 16K05395). This work was supported in part by a CREST-JST program.

References

1. S. Zhang and F. Li, *J. Appl. Phys.* **111**, 031301 (2012).
2. D. Fu et al., *Phys. Rev. Lett.* **103**, 207601 (2009).
3. D. Viehland et al., *Appl. Phys. Lett.* **67**, 2471 (1995).
4. P. Chu et al., *Sci. Rep.* **4**, 5007(2014).
5. S. W. Choi et al., *Ferroelectrics* **100**, 29 (1989).
6. B. Noheda et al., *Phys. Rev. B* **66**, 054104 (2002).
7. A. K. Singh et al., *Phys. Rev. B* **74**, 024101 (2006).
8. M. Matsuura et al., *Phys. Rev. B* **74**, 144107 (2006).
9. Z. Guo et al., *Appl. Phys. Lett.* **91**, 081904 (2007).
10. F. Bai et al., *J. Appl. Phys.* **97**, 054103 (2005).
11. A. K. Singh and D. Pandey, *Phys. Rev. B* **67**, 064102 (2003).
12. M. Matsushita et al., *JFE Tech. Rep.* **6**, 46 (2005).
13. F. Yan et al., *Appl. Phys. Lett.* **81**, 4580 (2002).
14. H. Okino et al., *Jpn. J. Appl. Phys.* **44**, 7160 (2005).

15. S. Gorfman et al., *Proc. Natl. Acad. Sci. USA*, **115**, E6680 (2018).
16. D. D. Viehland and E. H. K. Salje, *Adv. Phys.* **63**, 267 (2014).
17. K. Namikawa et al. *Phys. Rev. B* **100**, 184110 (2019).
18. Z. Kutnjak et al., *Nature (London)* **441**, 956 (2006).
19. D. Damjanovic, in *The Science of Hysteresis*, edited by I. Mayergoyz and G. Bertotti (Elsevier, New York, 2005), Vol. 3, pp. 337–465.
20. N. A. Pertsev and A. Yu. Emelyanov, *Phys. Rev. B* **65**, 174115 (2002).

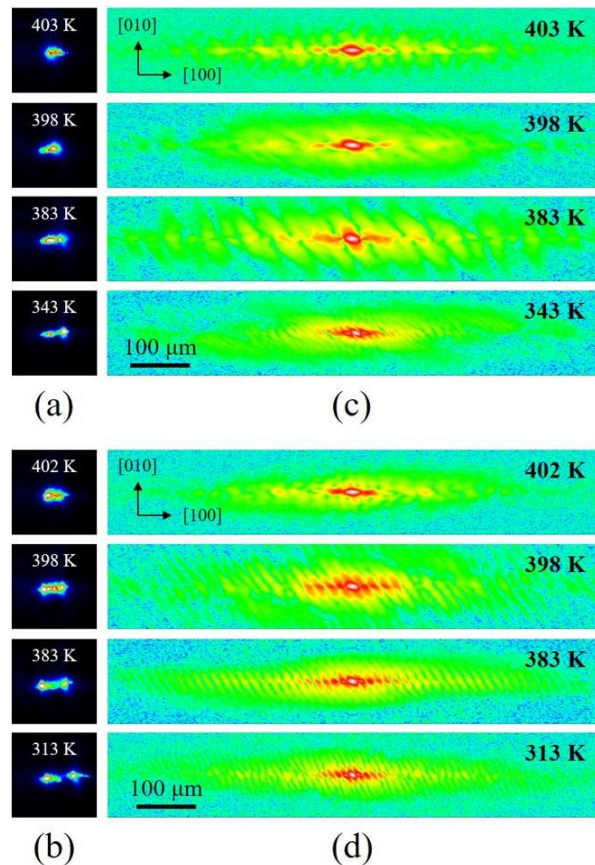


Fig. 1. Observed speckle patterns and calculated spatial correlation functions. (a)-(b) Coherent SXR speckle patterns for the PMN-27.8% PT sample measured under cooling in thermal non-equilibrium and equilibrium conditions, respectively. (c)-(d) Spatial autocorrelation functions obtained from the speckle patterns shown in (a) and (b), respectively.

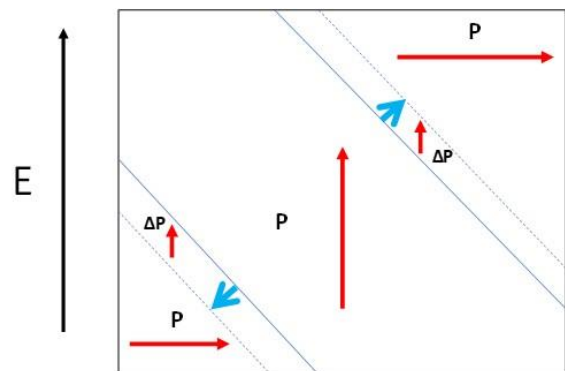


Fig. 2. Schematic model of the antiphase shift of domain walls under application of an electric field. Elastic strain is almost preserved at the antiphase shift of the domain walls.

Controlling Strong Excitation of Silicon as a Step towards Processing Materials at Sub-nanometer Precision



Thanh-Hung Dinh

X-ray Laser Group, Department of Advanced Photon Research

Introduction.

The interaction of a solid material with focused, intense pulses of high-energy photons or other particles (such as electrons and ions) creates a strong electronic excitation state within an ultra-short time and on ultra-small spatial scales. This offers the possibility to control the response of a material on a spatial scale of less than a nanometer¹ which is crucial for the next generation of nano-devices²⁻⁴.

To date, the nano-processing of matter has relied on techniques which utilize low-intensity radiation sources, such as lithography with high-energy beams of ions or electrons, extreme ultraviolet (EUV) photons or focused ion beam etching⁵. However, these techniques require multiple, time-consuming processing steps, and there are only a limited number of materials for which etchants and resists are available. Laser ablation is a promising alternative within the high-intensity regime, offering rapid processing with a feature resolution reaching the sub-micrometer through a direct removal of material^{6,7}. The main factors limiting the quality of these techniques are: (i) the spot size of the radiation beam, (ii) fast energy transport out from the primary interaction region. The constrained spot size of the beam (e.g., by the diffraction limit at the corresponding wavelength) limits the feature resolution of the processing. Energy transport out of the beam focus via secondary electrons leads to undesirable damages, decreasing the precision of the techniques (see Fig. 1). It also lowers the 'effective' dose absorbed by the material in the focus of the energetic photon (or particle) beam.

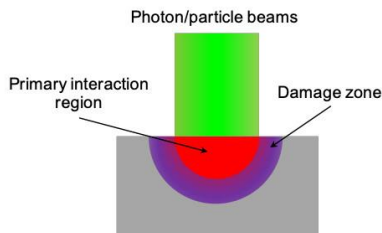


Fig.1 Schematic representation of a typical material processing.

The recent introduction of fourth generation light sources, x-ray free-electron lasers (XFELs) emitting intense light with wavelength down-to angstrom and a femtosecond pulse duration, offers new possibilities to investigate, and push, the limits of ultrahigh precision material processing. In contrast to conventional light sources including incoherent x-ray sources and optical lasers, XFELs can provide access to a strong electronic excitation state of solid materials within an unprecedented ultra-short time on ultra-small spatial scales. However, the dynamic response of a solid to nano-excitation in material processing is far from being fully understood due to a lack of experimental tools (e.g. light sources, detection techniques) precise enough to operate at the relevant temporal and spatial scales.

In this report, the author would like to introduce the recent

achievement of the QST-KPSI X-ray laser group on the field. Benchmarking a macroscopic experimental result against microscopic theoretical approaches reveals features of the nano-excitation in silicon material. We found the existence of an energy sink effect during ablation by means of rapid electron and energy transport which can suppress undesired hydrodynamical motions, allowing the silicon material to be directly processed with a precision reaching the observable limitation of an atomic force microscope.

Experimental results.

We created craters on the surface of a silicon substrate by focusing single femtosecond extreme ultraviolet pulses from the SPring-8 Angstrom Compact Free Electron Laser (SACLA). The laser spot, measured by knife-edge scanning, has a Gaussian-like energy profile with horizontal and vertical diameters of typically 8.5 and 10.5 μm at full width at half maximum (FWHM), respectively. The pulse duration of the SFXEL was measured to be approximately 70 fs FWHM by a correlation monitor. We used the photon energy of 92 eV (or the wavelength of $\lambda = 13.5$ nm) and 120 eV ($\lambda = 10.3$ nm) around the L-edge of the silicon. Note that the photon energy of 120 eV is above the L-edge of the silicon, which makes the attenuation length significantly (order of magnitude) shorter than in the case of 92 eV. We then investigated the resulting surface modification in the vicinity of the damage thresholds, establishing a connection to microscopic theoretical approaches, and, with their help, illustrated physical mechanisms for damage creation.

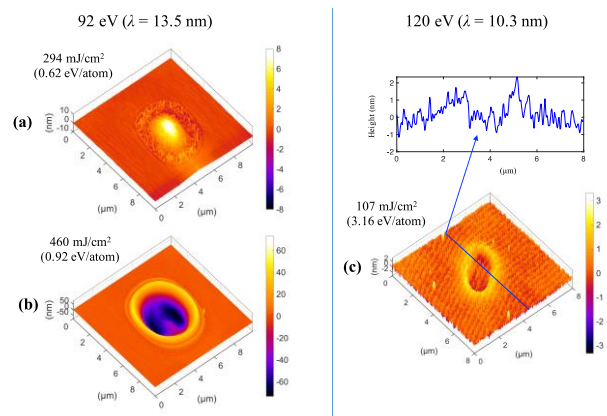


Fig.2 Surface modification of silicon in the vicinity of hole-formation thresholds for (a) 92eV and (b) 120 eV. These pictures were reconstructed from AFM data.

Figure 2 depicts the surface modification of silicon in the vicinity of the hole-formation thresholds. The threshold for the 92 eV photon was estimated to be of 418 mJ/cm^2 in fluence, or 0.89 eV/atom in the surface absorbed dose. In the case of 120 eV, the threshold was observed to be of 106 mJ/cm^2 in fluence, or

3.15 eV/atom in the surface absorbed dose. This dose is more than 3 times greater than that of the 92 eV data. As shown in Fig. 2 (b), the hole has been "drilled" by the 120 eV photon without any observable thermal cracks, surface roughness changes, or dome features, which were present in the case of the 92 eV (see Fig. 2 (a)).

Discussion and Conclusion.

Figure 3 shows typical timescales for physical phenomena associated with material processing using a femtosecond x-ray pulse. The x-ray induced modification of a solid material starts with photo-absorption resulting with damage of the electronic system at few-femtosecond scales. Significant modification or damage of the atomic system can only be observed at a scale later than sub-picosecond. (See detailed discussion in Ref. 1).

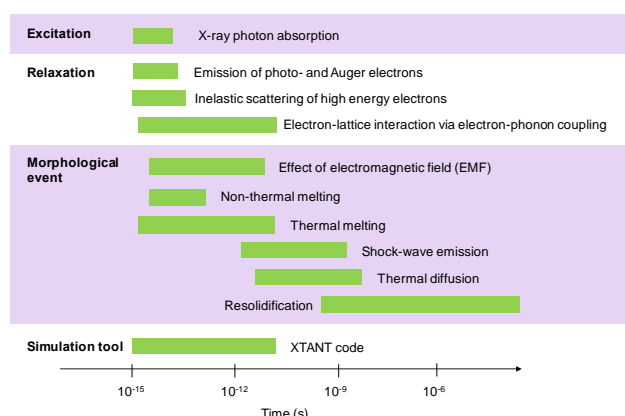


Fig.3 Timescales of physical processes following the interaction of a femtosecond x-ray pulse with solid materials.

The dose threshold of hole-formation for the 92 eV and 120 eV photon implied an existence of a rapid diffusion of the excited electrons and their energy, which leads to efficient cooling of the system. This increases the dose threshold for the damage, and provides a kinetic pathway for fast reorganization of the material. Such an energy sink effect would suppress undesirable phase transitions and keep a sharp boundary between the interaction region and the remaining part of the material as shown in Fig. 2 (b).

It is expected that an even greater energy sink effect can be achieved by reducing the photo-excited volume, after optimizing the incident photon energy and minimizing beam spot size. Note that the focal spots of the micrometer order in our experiment were two orders of magnitude greater than the attenuation length of the 120 eV photon. In contrast, irradiation with a laser spot as small as the attenuation length increases the gradient of deposited

energy as a function of the beam radius by two orders of magnitude along the radial axis. Consequently, the energy sink effect in the 2D system (axial and radial axis) becomes much greater, allowing the spatial scale of the damaged zone to significantly reduce. By scaling down the irradiated laser spot from micro- to nano-size using advanced x-ray optics^{8,9}, we expect that the direct machining with a sub-nanometer precision can be achieved.

In conclusion, we investigated the formation of damage and a crater in silicon substrates by focusing the femtosecond EUV pulse from the SACLA SXFEL as a proof of concept for high control in material processing for the next generation of nano-devices. Benefits for the radiobiological research on radio- and particle- therapy can also be anticipated. In parallel to experimental efforts, further development of simulation tools enabling long-timescale and large-spatial scale simulations of the processed materials is also necessary.

Acknowledgments

The author thanks M. Ishino, T. Kitamura, N. Hasegawa, T. Otobe, and M. Nikishino (QST), T. Higashiguchi (Utsunomiya Univ.), K. Sakaue (Univ. of Tokyo), M. Washio (Waseda Univ.), T. Hatano (Tohoku Univ.), A. Kon, Y. Kubota, Y. Inubushi, and S. Owada (RIKEN), N. Medvedev (IPP, Czech), and B. Ziaja (DESSY, Germany) for fruitful discussions.

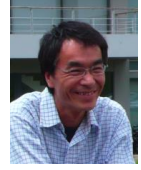
References

1. Dinh, T.-H. *et al.* Controlled strong excitation of silicon as a step towards processing materials at sub-nanometer precision. *Commun. Phys.* 1–9 (2019). doi:10.1038/s42005-019-0253-2
2. Barbry, M. *et al.* Atomistic near-field nanoplasmonics: Reaching atomic-scale resolution in nanooptics. *Nano Lett.* **15**, 3410–3419 (2015).
3. Kern, J. *et al.* Atomic-scale confinement of resonant optical fields. *Nano Lett.* **12**, 5504–5509 (2012).
4. Pauly, F., Cuevas, J. C., Natelson, D., Ward, D. R. & Hu, F. Optical rectification and field enhancement in a plasmonic nanogap. *Nat. Nanotechnol.* **5**, 1–5 (2010).
5. Chen, Y. & Pépin, A. Nanofabrication: Conventional and nonconventional methods. *Electrophoresis* **22**, 187–207 (2001).
6. Chichkov, B. N., Momma, C., Nolte, S., Von Alvensleben, F. & Tunnermann, A. T. Femtosecond, picosecond and nanosecond laser ablation of solids. *Appl. Phys. A* **63**, 109–115 (1996).
7. Kerse, C. *et al.* Ablation-cooled material removal with ultrafast bursts of pulses. *Nature* **537**, 84–87 (2016).
8. Mimura, H. *et al.* Breaking the 10 nm barrier in hard-X-ray focusing. *Nat. Phys.* **6**, 122–125 (2009).
9. Motoyama, H. & Mimura, H. Two-stage reflective optical system for achromatic 10nm x-ray focusing. *J. Phys. B At. Mol. Opt. Phys.* **48**, 244002 (2015).

Optical parametric oscillator pumped by femtosecond Yb-doped fiber laser

Keisuke Nagashima

Ultrafast Dynamics Group, Department of Advanced Photon Research



A synchronously pumped optical parametric oscillator (SPOPO) is a powerful tool for generating femtosecond and picosecond pulses. However, the pulse energies are on the order of nanojoules because of the high repetition frequency of several tens of megahertz. Higher pulse energies are needed and considerable work has been reported for increasing SPOPO pulse energies [1–8]. Here, we report the first demonstration of an SPOPO pumped by a femtosecond Yb-doped fiber laser operated in a burst mode. The burst-mode operation increases the pulse energy by limiting the total number of pulses [9–13].

We developed a Yb-doped fiber laser that featured chirped pulse amplification at a repetition rate of 100 kHz. Figure 1 shows the laser system, which consists of a mode-locked fiber oscillator, a pulse stretcher, a fiber pre-amplifier, a Pockels cell, a pulse stretcher, a fiber pre-amplifier, a Pockels cell, multi-stage fiber amplifiers, and a pulse compressor.

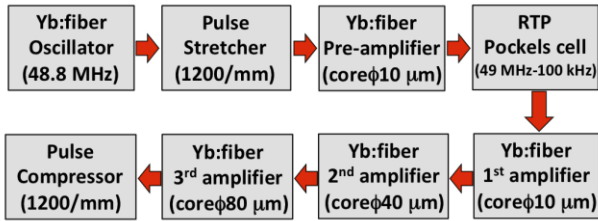


Fig. 1. Block diagram of the Yb-doped fiber laser system.

The repetition frequency of the mode-locked fiber oscillator was 48.8 MHz. Femtosecond pulses generated in the oscillator were stretched in the pulse stretcher and amplified in the pre-amplifier. Then, the repetition frequency was reduced from 48.8 MHz to 100 kHz by the Pockels cell (RTP-4-20, LEYSOP). The 100 kHz pulses were amplified in three-stage fiber amplifiers and were compressed in the pulse compressor. The core diameters of the Yb-doped fibers were 10 μm , 40 μm , and 80 μm in the three-stage amplifiers. Gold-coated 1200 groove/mm reflection gratings were used in both the pulse stretcher and pulse compressor. Self-phase modulation in the fibers was minimized by controlling the laser-diode pump power for each amplifier. The output pulses had a central wavelength of 1039 nm, a full-width at half-maximum (FWHM) spectral width of 7 nm, and a FWHM pulse length of 350 fs. The output power from the final amplifier was limited up to 2.5 W in the experiments.

Periodically poled materials have been used in many SPOPO experiments. They are MgO-doped periodically poled LiTaO₃ (MgO:PPLT) and MgO-doped periodically poled LiNbO₃ (MgO:PPLN). These materials offer several advantages for increasing pulse energy, such as high nonlinear coefficients and no spatial walk-off that can increase the nonlinear interaction length. MgO:PPLT was used here because it has a high tolerance to optical damage [14].

Figure 2 shows the optical configuration of the SPOPO, in which a fan-out MgO:PPLT crystal was used. The crystal was 1 mol% MgO-doped stoichiometric PPLT (manufactured by

OXIDE). The crystal surfaces had broadband anti-reflection coatings for the range of 1000–1700 nm. The crystal had a 11 mm length (propagation direction), a 2 mm height, and a 7 mm width. The effective width was 5 mm, where the poling period had a fan-out structure and changed over range of 29.3–32.4 μm . The dichroic mirror and the spherical lens were CaF₂ to prevent idler light absorption. The dichroic mirror had a transmission band of 1000–1100 nm and a reflection band of 1250–1700 nm. The output coupler had a constant transmission rate of 70% over the 1300–1700 nm range.

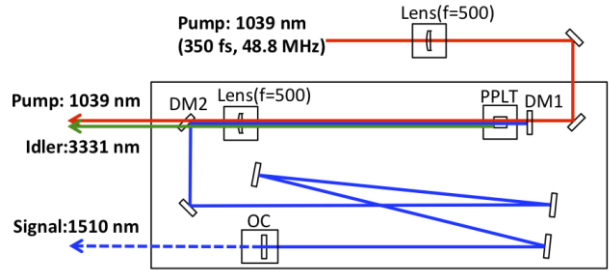


Fig. 2. SPOPO optical configuration. PPLT: MgO:PPLT crystal; DM1 and DM2: dichroic mirrors; OC: output coupler.

The SPOPO had an optical cavity length of 3.07 m, which gives a 48.8 MHz repetition frequency. The ends of the cavity were a dichroic mirror (DM1) and an output coupler (OC). In the cavity design, the signal light had a 0.18 mm radius at the DM1 and a 1.0 mm radius at the OC. The MgO:PPLT crystal was placed in the immediate vicinity of the DM1.

In the experiments, the signal wavelength was tunable in the range of 1450–1700 nm. We adjusted the signal wavelength to 1510 nm, which was generated in coincidence with the 3331 nm idler wavelength. The corresponding poling period of the MgO:PPLT was 30.3 μm . In the crystal, the group indices at the signal, idler, and pump wavelengths were 2.161, 2.193, and 2.185, respectively [15]. Therefore, the signal pulse was faster than the pump pulse and, conversely, the idler pulse was slower than the pump pulse. We used the 11 mm long MgO:PPLT crystal because the interaction length for the parametric conversion increased with crystal length.

The pump and signal pulses were respectively measured by the Si photo-detector with a 0.35 GHz bandwidth and the InGaAs photo-detector with a 5 GHz bandwidth. The sampling frequency of the oscilloscope was 10 GHz for both detectors. Figures 3(b) and (c) show the waveforms of the pump and signal pulses during SPOPO operation. The number of pump pulses was $N = 5$ and the average pump power was 1.7 W. The horizontal axis started from the 100 kHz oscilloscope trigger. The fifth pump pulse was at $t = 124$ ns and the fifth signal pulse was at $t = 145$ ns. The first signal pulse was not observed and the second was barely detected at $t = 83$ ns.

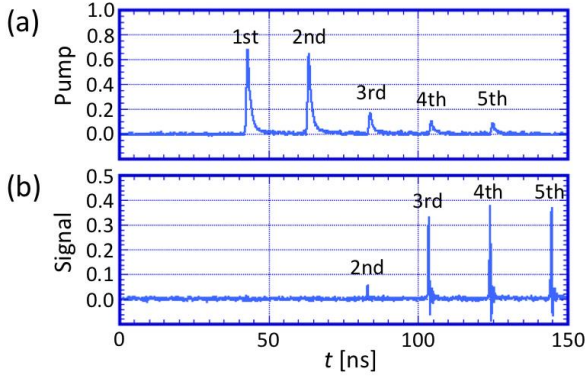


Fig. 3. Waveforms of the pump and signal pulses with SPOPO operation with $N = 5$: (a) pump pulses and (b) signal pulses.

Figure 4(a) shows the fifth signal pulse energy E_{sig} as a function of the pump pulse energy E_{pump} . These pulse energies were measured by the photo-detectors, which were calibrated by power-meters. We generated a signal pulse with energy greater than $1 \mu\text{J}$ when $E_{\text{pump}} > 2.4 \mu\text{J}$, and the energy was $1.5 \mu\text{J}$ when $E_{\text{pump}} = 4.8 \mu\text{J}$. This is the highest pulse energy reported for femtosecond pulses obtained from an SPOPO. The energy efficiency $E_{\text{sig}}/E_{\text{pump}}$ was 38% at $E_{\text{pump}} = 3.4 \mu\text{J}$ and 32% at $E_{\text{pump}} = 4.8 \mu\text{J}$. The maximum pump intensity on the crystal was 8.3 GW/cm^2 , which was considerably lower than that in a previous experiment with a high pump intensity on MgO:PPLN [16]. We observed no damage in the crystal and no parametric generation except for the SPOPO signal.

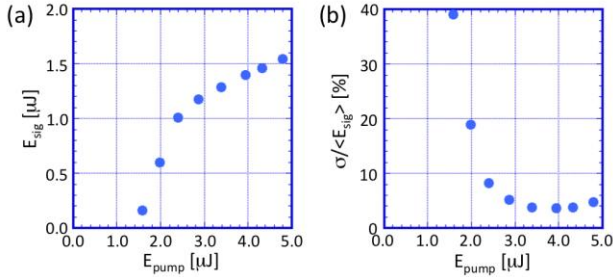


Fig. 4. (a) Energy of the fifth signal pulse as a function of the pump pulse energy. (b) Standard deviation divided by the average value of the signal pulse energy as a function of the pump pulse energy.

Figure 4(b) plots pulse-to-pulse energy fluctuations of the fifth signal pulses as a function of the pump pulse energy E_{pump} . Here, we use the average value of the fifth signal pulse energy as $\langle E_{\text{sig}} \rangle$ and the standard deviation as σ . We use the value of $\sigma / \langle E_{\text{sig}} \rangle$ as an indicator of the pulse-to-pulse fluctuation. (The pulse-to-pulse fluctuation of the pump pulses was approximately 1%.) This fluctuation was caused by the optical parametric noise, which becomes a seed of the signal pulse. The statistical properties of

the signal pulse fluctuation were described in our most recent report [17].

In summary, we demonstrated an SPOPO pumped by a burst-mode Yb-doped fiber laser, which had 100 kHz pulse trains with a finite number of pump pulses that could be controlled by a Pockels-cell gate. We obtained a signal pulse energy of $1.5 \mu\text{J}$ with a $4.8\text{-}\mu\text{J}$ pump pulse. Pulse-to-pulse fluctuations could be suppressed for as few as five pump pulses.

Acknowledgments

The authors thank M. Maruyama and M. Tsubouchi for their support, and T. Otobe, N. Ishii, T. Endo, and H. Akagi for their valuable discussions.

References

1. T. P. Lamour, L. Kornaszewski, J. H. Sun, and D. T. Reid, *Opt. Express* **17**, 14229 (2009).
2. T. Südmeyer, E. Innerhofer, F. Brunner, R. Paschotta, T. Usami, H. Ito, S. Kurimura, K. Kitamura, D. C. Hanna, and U. Keller, *Opt. Lett.* **29**, 1111 (2004).
3. F. Kienle, P. S. Teh, S.-U. Alam, C. B. E. Gawith, D. C. Hanna, D. J. Richardson, and D. P. Shepherd, *Opt. Lett.* **35**, 3580 (2010).
4. T. Petersen, J. D. Zuegel, and J. Bromage, *Opt. Express* **25**, 8840 (2017).
5. C.-K. Min and T. Joo, *Opt. Lett.* **30**, 1855 (2005).
6. L. Xu, H.-Y. Chan, S.-U. Alam, D. J. Richardson, and D. P. Shepherd, *Opt. Lett.* **40**, 3288 (2015).
7. T. P. Lamour and D. T. Reid, *Opt. Express* **19**, 17557 (2011).
8. L.-J. He, K. Liu, Y. Bo, Z. Liu, X.-J. Wang, F. Yang, L. Yuan, Q.-J. Peng, D.-F. Cui, and Z.-Y. Xu, *Opt. Lett.* **43**, 539 (2018).
9. H. Kalaycioglu, K. Eken, and F. O. Ilday, *Opt. Lett.* **36**, 3383 (2011).
10. H. Kalaycioglu, Y. B. Eldeniz, O. Akcaalan, S. Yava, S. K. Gürel, M. Efe, and F. O. Ilday, *Opt. Lett.* **37**, 2586 (2012).
11. X. Li, S. Zhang, Y. Hao, and Z. Yang, *Opt. Express* **22**, 6699 (2014).
12. H. Kalaycioglu, O. Akcaalan, S. Yava, S. Y. B. Eldeniz, and F. O. Ilday, *J. Opt. Soc. Am. B* **32**, 900 (2015).
13. P. Elahi, S. Yilmaz, Y. B. Eldeniz, and F. O. Ilday, *Opt. Lett.* **39**, 236 (2014).
14. N. E. Yu, S. Kurimura, Y. Nomura, and K. Kitamura, *Jpn. J. Appl. Phys.* **43**, L1265 (2004).
15. M. Nakamura, S. Higuchi, S. Takekawa, K. Terabe, Y. Furukawa, and K. Kitamura, *Jpn. J. Appl. Phys.* **41**, L465 (2002).
16. Y. Deng, A. Schwarz, H. Fattahi, M. Ueffing, X. Gu, M. Ossiander, T. Metzger, V. Pervak, H. Ishizuki, T. Taira, T. Kobayashi, G. Marcus, F. Krausz, R. Kienberger, and N. Karpowicz, *Opt. Lett.* **37**, 4973 (2012).
17. K. Nagashima, Y. Ochi, and R. Itakura, *J. Opt. Soc. Am. B* **36**, 3389 (2019).

Plane photoacoustic wave generation in water using irradiation of terahertz pulses

Masaaki Tsubouchi

Ultrafast Dynamics Group, Department of Advanced Photon Research



Pressure wave generation is one of the important processes induced by irradiation of strong laser light in condensed media. When the medium strongly absorbs laser light with short pulse duration, the energy of the light is confined in a small volume and subsequently released as a pressure wave via the thermoelastic effect. In the linear absorption region, a photoacoustic wave is generated by light absorption and propagated at the speed of sound in the medium. Photoacoustic waves have been applied in water for non-invasive tomographic imaging for biomedical issues.

The visible or near-infrared (IR) laser lights used in previous studies transmit through water. Therefore, alternative light absorbers (black rubber, dye molecules, *etc.*) or plasma generation are required in conventional methods, as shown in Fig. 1(a). However, it is possible to damage tissues by the use of dyes or focusing strong laser light.

In this study, we propose THz-light-induced plane photoacoustic wave generation.¹ The THz light is completely absorbed very close to the surface of water with a penetration depth of 10 μm , as shown in Fig. 1(b). The strong absorption induces a rapid and local pressure increase followed by effective photoacoustic wave generation without any absorber. The strong absorption of the THz light also realizes plane photoacoustic wave propagation. Because according to Huygens' principle, a large-area excitation source is required for plane wave propagation, efficient energy conversion from the light to the pressure wave is necessary. A plane wave is superior to a spherical one for practical use because a plane wave can be delivered without intensity drop over long distances (Fig. 1(b)), and geometrical control such as reflection and focusing onto the target can be easily carried out. In addition, the low photon energy (4 meV at 1 THz) of the THz light does not induce any ionization, dissociation, or structural changes in the molecules.

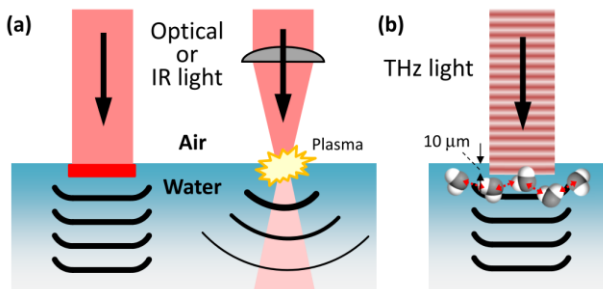


Fig. 1. Mechanisms of pressure wave generation at the air-water interface. (a) An optical or IR laser generates pressure waves via an additional light absorber or plasma generation by a strong laser. (b) A THz laser, by contrast, can directly generate plane waves from a relatively weak field with a loose focus.

We demonstrate the photoacoustic wave generation with THz light provided by a free-electron laser (FEL) and detect it

using the shadowgraph imaging method with 10 ns time and 15 μm spatial resolutions. The characteristics of the THz photoacoustic wave are investigated by observing the spatiotemporal evolution.

For the THz light source to generate the photoacoustic wave, we employed the THz-FEL on the L-band electron linear accelerator (LINAC) at the Research Laboratory for Quantum Beam Science, Institute of Science and Industrial Research, Osaka University. Linearly polarized THz macropulses are generated by the THz-FEL at a repetition rate of 5 Hz with the highest pulse energy of 50 mJ. Figure 2(a) shows a THz macropulse structure measured with a fast pyroelectric detector. The macropulse contains a train of around 150 micropulses separated at 36.9 ns intervals (27 MHz repetition). The highest micropulse energy was estimated to be 350 μJ , which is far and away the largest THz-FEL micropulse energy reported in the world. The temporal width of the micropulse was measured to be 1.7 ps by an electro-optic sampling technique. The center frequency was 4 THz, which corresponds to a lower frequency edge of the absorption band due to the intermolecular vibration in water. At this frequency, the absorption coefficient of water is 800 cm^{-1} , which implies that more than 99.7% of irradiated energy is absorbed within 0.1 mm of the surface.

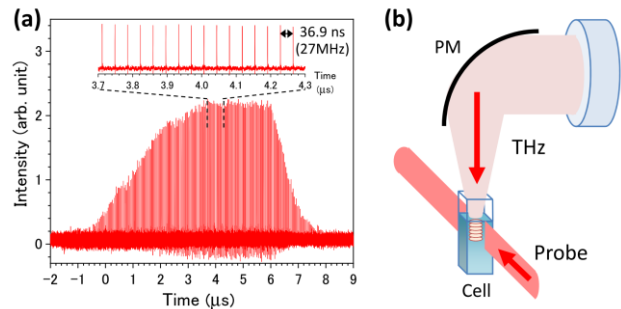


Fig. 2. (a) Macropulse structure containing a train of approximately 150 micropulses. Inset shows the enlarged micropulse train with an interval of 36.9 ns (a repetition rate of 27 MHz). (b) Experimental setup for generating and probing the THz-FEL-induced photoacoustic wave. PM: off-axis gold-coated parabolic mirror with a focal length of 50 mm; cell: quartz sample cell on a lab jack to adjust the focus diameter of the THz light on the air-water interface.

Figure 2(b) shows a schematic diagram of the photoacoustic wave generation and observation system. The THz light passing through a polycrystalline diamond window from the evacuated FEL system into air was loosely focused on the distilled water sample using a gold-coated off-axis parabolic mirror with a 50 mm focal length. To evaluate the spot size of the THz pulse on the water surface, we used the knife-edge method and estimated it to be 0.7 mm at full width at half maximum. The input pulse energy was attenuated with THz attenuators (TYDEX), which contained wedged silicon wafers with different attenuation levels.

A two-dimensional cross-section image of the photoacoustic wave was observed using the shadowgraph technique, which clearly shows an inhomogeneous density distribution in transparent media. In the shadowgraph image, the signal intensity depends on the second derivative of the refractive index, which is related to pressure and density via the Gladstone–Dale relation. Therefore, the shadowgraph is sensitive to the pressure, that is, the photoacoustic wave. As a probe light, a CW diode laser (LDM670, Thorlabs) with an output wavelength of 670 nm irradiates the distilled water in the quartz sample cell with a thickness of 10 mm. The probe light was incident on the water sample perpendicular to the shockwave propagation and was imaged by a $4f$ -type lens system onto the image-intensified CCD of a Princeton PI-MAX3 camera. The image capturing system was synchronized to the timing of the FEL macropulse generation, and gated with a time duration of 10 ns. The time gate was electronically scanned with the delay generator in the PI-MAX3 system. In this system, we observed time evolution of THz-light-induced phenomena from a nanosecond to a millisecond time scale with a time resolution of 10 ns.

Figure 3(a) shows a shadowgraph image of a water sample irradiated by the THz-FEL with an average micropulse energy of 20 μJ . This energy corresponds to a power density of 3.1 GW/cm^2 with a pulse width of 1.7 ps and a beam diameter of 0.7 mm. A stripe pattern is clearly seen in the image. Each horizontal line corresponds to a pulse front of photoacoustic waves induced by the THz micropulse train in the single macropulse shown in Fig. 2(a). An adjacent photoacoustic wave is that generated by the adjacent THz pulse. Thus, the propagation of the photoacoustic wave in water can be obtained from a single captured image. One remarkable feature is the plane wave front. The plane wave is generated from the plane source with loosely focused THz-FEL light, because its beam width of 0.7 mm is much larger than the thickness of the wave front, $\sim 5 \mu\text{m}$. The nature of the plane wave causes the long-distance propagation of the photoacoustic wave, as explained in Fig. 1(b). We emphasize that the photoacoustic wave reaches 3 mm in depth, which is 100 times longer than the skin depth of water for THz light. This result indicates that the energy of the THz light can be delivered into the water by the photoacoustic wave as mechanical energy. The spacing between wave fronts shown in Fig. 3(a) is 55 μm on average, which corresponds to the distance travelled by the photoacoustic wave in the time intervals of the THz pulse train, 36.9 ns. Thus, we can estimate the speed of the photoacoustic wave in water to be 1491 m/s, which is the same as the sound velocity in distilled water at 23 $^{\circ}\text{C}$.

Figure 3(b) displays a series of photoacoustic waves measured by scanning the gate timing of the CCD camera. The amplitude is obtained from the horizontal sum of the pixel intensities in each row of the shadowgraph image. The

photoacoustic waves arise at the air–water interface with time intervals of 36.9 ns and propagate with the velocity of sound deeper into the water.

The large absorption coefficient of the THz light means that the penetration depth in water is considerably shorter than 1 mm. Therefore, the THz light can directly affect molecules or biological tissues only within a submillimeter range. In previous studies, THz-light-induced DNA damage to a human skin sample with a thickness of less than 0.1 mm has been examined and discussed. THz-light-induced photoacoustic waves will potentially be able to probe and control chemical reactions and biological structures beyond the penetration depth.

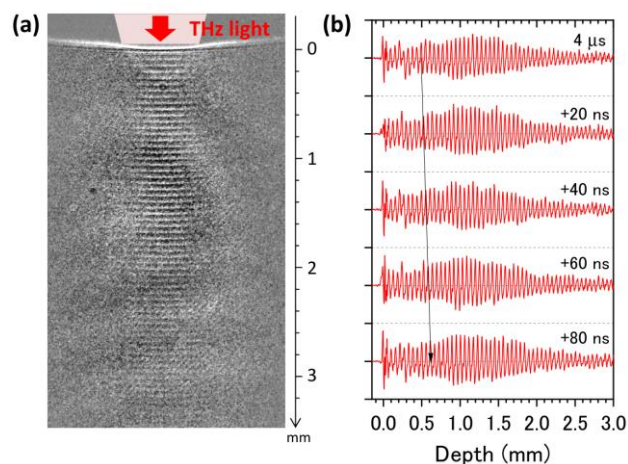


Fig. 3. (a) Snapshot image of a train of photoacoustic waves induced by the THz-FEL with a frequency of 4 THz and an average micropulse energy of 20 μJ . This image was taken with a time gate of 10 ns. (b) Wave amplitudes as a function of depth measured by scanning the gate timing of the image intensifier in the CCD camera. The amplitude is obtained from the horizontal sum of the pixel intensities in each vertical pixel of the image. The black arrow shows the propagation of a single photoacoustic wave.

Acknowledgments

The author thanks Prof. M. Nagai (Osaka Univ.), Dr. H. Hoshina (RIKEN), and Prof. G. Isoyama (Osaka Univ.) for valuable discussions and comments. The author is grateful for the financial support of QST President’s Strategic Grant (Creative Research).

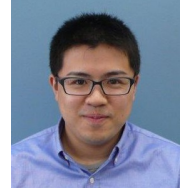
References

1. M. Tsubouchi, H. Hoshina, M. Nagai, and G. Isoyama, <https://arxiv.org/abs/1911.04674>

Characterization of UV pulses by plasma-mirror FROG using a liquid-sheet jet of water

Tomoyuki Endo

Ultrafast Dynamics Group, Department of Advanced Photon Research



We have developed an all-optical technique based on time-resolved reflection spectroscopy to characterize ultrashort laser pulses [1–3]. Ultrafast switching of a plasma mirror formed by focusing near-infrared (NIR) intense laser pulses on a fused silica plate was used as a gate function in a frequency-resolved optical gating (FROG) trace. Since all the optics employed in this plasma-mirror FROG (PM-FROG) technique are reflective optics, pulse shapes can be characterized without requiring post-analysis to remove material dispersions. The PM-FROG technique was successfully applied to pulse characterization in the vacuum ultraviolet (VUV) region.

In previous studies, since a fused silica plate was employed as a target sample, the applicable repetition rate of the laser system was limited to 10 Hz by the speed of mechanical movement to avoid the effects of ablation damage on the target surface. In this study, we employ a liquid-sheet jet of water as a target instead of a solid to extend the applicable repetition rate to 1 kHz or more. The liquid-sheet jet provides an optically flat surface for each laser shot without mechanical operation of the target. Another concern was that the VUV waveform obtained by PM-FROG was not compared with one by another method. Here, we employ an ultraviolet (UV) pulse and compare the results obtained by PM-FROG and another established technique to demonstrate the validity of the PM-FROG technique.

The details of the experimental setup for producing a liquid-sheet jet were described elsewhere [4, 5]. Briefly, a peristaltic pump, a pulsation damper, and a slit-type nozzle are used to produce a flat-sheet jet of water with a flow rate of approximately 60 mL/min. The thickness of the liquid sheet is evaluated to be 8 μm by measuring the spectral interference between reflected UV pulses from the front and back surfaces. The output of a Ti:sapphire chirped pulse amplification system is introduced to a β -barium borate (BBO) crystal to generate the second-harmonic pulses. The residual fundamental NIR pulse and the second-harmonic UV pulse are separated by a dielectric mirror, which reflects the UV pulse and transmits the NIR pulse. The time delay between two pulses is controlled by a translational stage. The NIR and UV pulses are co-linearly combined again by another dielectric mirror and focused on the surface of the liquid-sheet jet of water by using a concave mirror with an effective focal length of 150 mm. Both NIR and UV pulses are horizontally polarized. A small incident angle of $\sim 5^\circ$ and a $4f$ image-relay setup are employed to reduce the effects of fluctuations in the orientation and curvature of the surface of the liquid-sheet jet due to residual pulsation of the pump. The spectra of the reflected UV pulse are recorded as a function of the time-delay τ between the NIR and UV pulses. The obtained FROG signal may be expressed as:

$$I_{\text{sig}}(\omega, \tau) = \left| \int_{-\infty}^{\infty} E(t - \tau) r(t) e^{-i\omega t} dt \right|^2,$$

where ω and $E(t)$ are the angular frequency and the complex electric field amplitude of the UV pulse, respectively, and $r(t)$ is the complex reflection coefficient of the plasma mirror.

The measured FROG trace is shown in Fig. 1(a). In the negative time-delay region where the UV pulse comes first, the

contribution of the Fresnel reflection of unexcited water on the liquid-sheet surface is observed. The signal intensity decreases slightly and then increases dramatically. This indicates that the refractive index of the liquid-sheet surface is decreased as a result of plasma formation as described by the Drude model. Qualitatively speaking, the refractive index of water, n_{water} , decreases and approaches that of air ($n_{\text{air}} \approx 1$) as the plasma density increases, hence the reflection coefficient becomes zero. As the refractive index further decreases to $n_{\text{water}} < 1$, the reflection coefficient begins to increase.

The least-squares generalized projections algorithm (LSGPA) [6] is adopted to reconstruct the FROG trace. To avoid convergence to a local minimum, the initial guess of the second-order dispersion of the UV pulse is obtained from the slope of the line along minimum values at each frequency component. When a Fourier-transform-limited pulse is radiated at a plasma mirror, all the frequency components are reflected simultaneously. This corresponds to a slope of zero. When a positively chirped pulse is reflected by a plasma mirror, the effective time-delay of each frequency increases as the frequency increases. As a result, the PM-FROG trace shows an earlier rise at a higher frequency. As shown in Fig. 1(a), the initial guess of the second-order dispersion is estimated to be -163 fs^2 from the slope.

The PM-FROG trace is successfully reconstructed by the LSGPA, as shown in Fig. 1(b). The retrieved temporal waveform and corresponding spectrum of the UV pulse are shown in Fig. 2. The full-width at half-maximum of the pulse duration is evaluated to be 52 fs by a Gaussian fit, which shows the pulse is almost

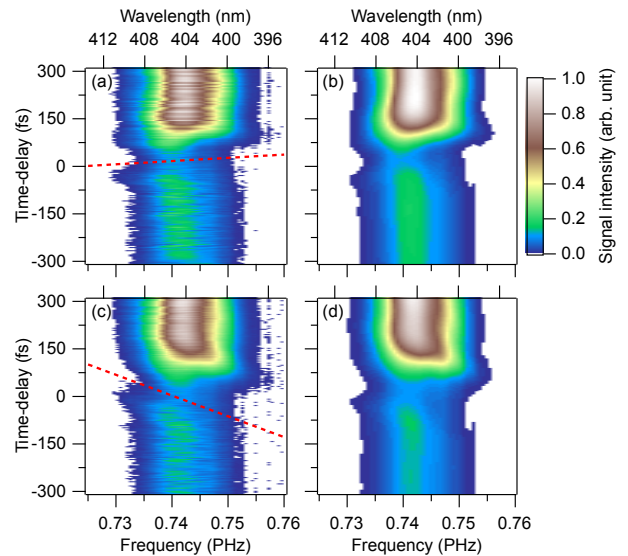


Fig. 1. (a) Measured FROG trace. The red dotted line is a linear fit for minimum values at each frequency in the FROG trace. (b) Reconstructed FROG trace by the LSGPA from (a). (c) Same as (a), but with the transmission of a fused silica plate (10 mm thick). (d) Same as (b), but from (c).

Fourier-transform-limited. The obtained spectrum is consistent with one measured by another spectrometer. Since there are no transmission optics in the PM-FROG setup, the PM-FROG technique would be applicable to pulse characterization of short-wavelength pulses without post-subtraction of material dispersions from the obtained phase.

To demonstrate pulse characterization of chirped pulses, a fused silica plate (10 mm thick) is introduced to add a chirp to the UV pulse. The measured FROG trace with the transmission of the fused silica plate is shown in Fig. 1(c). The slope of the red dotted line changes compared to that without the fused silica plate, showing that the PM-FROG trace reflects the second-order dispersion of the UV pulse as described above. The initial guess of the second-order dispersion for the chirped UV pulse is evaluated to be 1043 fs^2 from the slope. The reconstructed PM-FROG trace is shown in Fig. 1(d). The temporal waveform and corresponding spectrum of the chirped UV pulse are shown in Fig. 2. The pulse duration becomes longer than that without the fused silica plate and is estimated to be 60 fs. As shown in Fig. 2(b), the spectral phase shows a clear effect of the spectral dispersion by the fused silica plate. The second-order dispersions with and without the 10 mm fused silica plate are evaluated to be $903.5 \pm 60.7 \text{ fs}^2$ and $-61.7 \pm 36.6 \text{ fs}^2$, respectively, by using a polynomial fit at the central frequency of 0.743 PHz. The group velocity dispersion (GVD) of fused silica is measured to be $96.5 \pm 7.2 \text{ fs}^2/\text{mm}$.

Another established pulse characterization technique, SD-FROG, is also performed to demonstrate the validity of the results obtained by PM-FROG. A non-collinear SD-FROG setup is employed for a single-shot measurement in this study. In this SD-FROG setup, the UV pulse transmits a beam splitter (fused silica, 3 mm thick) to make a replica. Therefore, the second-order dispersion caused by the fused silica plate has to be subtracted from the retrieved spectral phase through post-analysis to obtain the actual waveform. The second-order dispersions measured by SD-FROG with and without the fused silica plate are evaluated to be $930.1 \pm 207.7 \text{ fs}^2$ and $66.4 \pm 215.3 \text{ fs}^2$, respectively, which are consistent with the values measured by PM-FROG within the error. The GVD of fused silica is evaluated to be $86.4 \pm 29.9 \text{ fs}^2/\text{mm}$ by SD-FROG.

The GVDs obtained by PM-FROG and SD-FROG are consistent with the value in the literature ($96.2 \text{ fs}^2/\text{mm}$) of the GVD of fused silica [7]. These results indicate that PM-FROG can be used to characterize the waveform of the Fourier-transform-limited pulse, as well as of chirped pulses. The results by PM-FROG using the liquid-sheet jet of water are as reliable as the results by SD-FROG.

We demonstrated a pulse characterization technique based on time-resolved reflection spectroscopy for a high-repetition

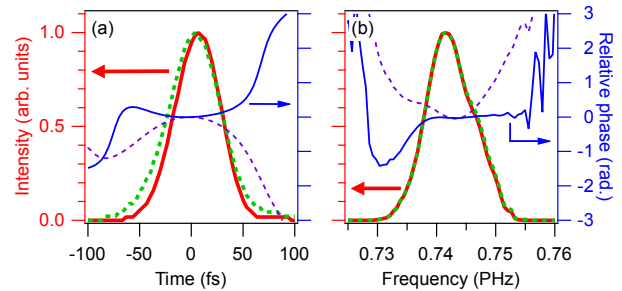


Fig. 2. (a) Temporal waveform and (b) corresponding spectrum of the UV pulse retrieved from Figs. 1(a) and (c) by the LSGPA. The dashed and solid lines correspond to the results with and without transmission of a fused silica plate (10 mm thick), respectively.

laser system. From the flow rate of the liquid-sheet jet, the applicable repetition rate of this technique would be extended to 100 kHz without a major update. By employing a liquid target instead of a solid target, the applicable repetition rate could be extended up to 10^4 times. In addition, although we did not discuss this detail in this paper, the time-dependent complex reflection coefficient of the plasma mirror, $r(t)$, can be also retrieved from the PM-FROG trace. The PM-FROG technique would be a powerful tool not only to characterize a waveform, but also to investigate the plasma dynamics and ionization dynamics of a liquid.

Acknowledgments

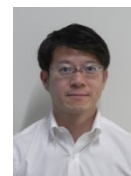
The author thanks Drs. R. Itakura and M. Tsubouchi for their contributions, Drs. T. Nakajima and K. Nagashima for valuable discussion, and Y. Hagihara for technical support. This work has been supported by the following funding sources: Japan Society for the Promotion of Science (JSPS) (KAKENHI 17H02802); Research Foundation for Opto-Science and Technology; Ministry of Education, Culture, Sports, Science and Technology (MEXT) (Q-LEAP ATTO JPMXS0118068681); and Institute of Advanced Energy, Kyoto University (ZE30B-37).

References

1. R. Itakura et al., *Opt. Express* **23**, 10914 (2015).
2. R. Itakura et al., *High Power Laser Sci. Eng.* **4**, e18 (2016).
3. R. Itakura et al., *Opt. Lett.* **44**, 2282 (2019).
4. M. Kondoh et al., *Opt. Express* **22**, 14135 (2014).
5. T. Endo et al., *Opt. Lett.* **44**, 3234 (2019).
6. J. Gagnon et al., *Appl. Phys. B* **92**, 25 (2008).
7. I. H. Malitson, *J. Opt. Soc. Am.* **55**, 1205 (1965).

Potential application of infrared lasers in the fields of pathology

M. Aoyama¹⁾, T. Morioka^{2,3)}, K. Yamakawa¹⁾



¹⁾ Medical Laser Applications Group, Department of Advanced Photon Research

²⁾ Department of Radiation Effects Research, NIRS, ³⁾ Institute for Quantum Life Science

QST has developed various “quantum beams” for materials science, and some of these are beginning to be applied in life science. Spectroscopy has contributed greatly to the understanding of the physical sciences as it was able to provide information on the structure of the elements and molecules that make up every subject of both the physical and biological sciences. Infrared (IR) spectroscopy has been widely applied to detect the vibrational characteristics of chemical functional groups in diverse materials (Fig.1) [1,2]. Mid-infrared (MIR) microscopic imaging has become an essential tool for detecting and characterizing the molecular components of biological specimens. The analytical technique allows for the molecular imaging of complex samples by measuring the absorption of MIR radiation between 2.5 and 14 μm by the vibrational transitions of covalent bonds. The advantage of this technique is the production of unique images that show the spatial distribution of proteins, lipids, carbohydrates, cholesterol, nucleic acids, and phospholipids. In addition, MIR has advantages of efficiency and adaptability for noninvasive investigation of the chemical compositions of cells and tissues using a reagentless procedure and without staining. Therefore, the MIR has been a fruitful regime for medical research.

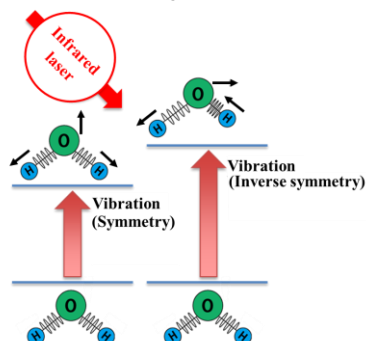


Fig.1. IR laser energy is absorbed by vibration of various biomolecules.

Pathology is the study and diagnosis of diseases through the examination of organs, tissues, and cells. Disease diagnosis by pathology generally involves gross and microscopic visual examination of tissues and cells with specialized stains employed to visualize specific proteins. Certain visualization techniques, such as special staining, immunohistochemistry, and electron microscopy, have expanded the means by which pathologists can diagnose diseases. However, these techniques require complicated processes and considerable time, and it is difficult to visually detect biochemical changes using them. Therefore, development of a simple analytical technique is desired. MIR spectroscopy has a potential for application to visualization tools to aid pathologists in assessing tissue specimens.

In this study, we investigate the discrimination of normal tissue and malignant tumors (hematopoietic tumor and epithelial tumor) using the MIR laser. In addition, we attempt to detect non-cancerous lesions (ischemic lesions). In our laboratory, an MIR microscopic system was constructed for the analysis of

tissue specimens (Fig. 2).

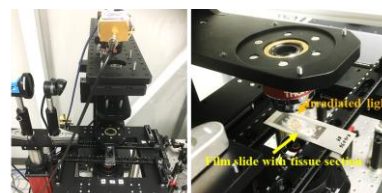


Fig.2. MIR microscopic system developed by our laboratory.

1. Hematopoietic tumor

The hematopoietic tumor invading the liver and normal liver tissue of a mouse was analyzed, and its absorbance was compared with that obtained from an unstained tissue specimen (Fig. 3). In Figure 3a, blue and red circles indicate the three different measurement sites by MIR microscopy in normal liver tissue and hematopoietic tumor, respectively. Figure 3b illustrates the MIR spectra of the normal liver tissue and hematopoietic tumor from three different sites in normal (Normal 1–3, blue circles) and tumor (Tumor 1–3, red circles) areas, and shows that the spectral patterns in the tumor (red lines) differed from those in the normal tissue (blue lines). The most changes in absorbance were observed in the two different regions (green double-headed arrows, Fig. 3b). Next, we conducted microscopic mapping of the hematopoietic tumor to obtain information on the absorbance of tumor cells. The infiltrated hematopoietic tumor area for the mapping was determined by examining the MIR microscopic field (Fig. 3c) compared with the corresponding histopathological view (Fig. 3e). Figure 3d displays the MIR absorbance map of the hematopoietic tumor infiltrated into the liver. The color classification based on the MIR absorbance changes segments three main parts: hematopoietic tumor and normal liver tissue, represented by the red and green ends, respectively, and the

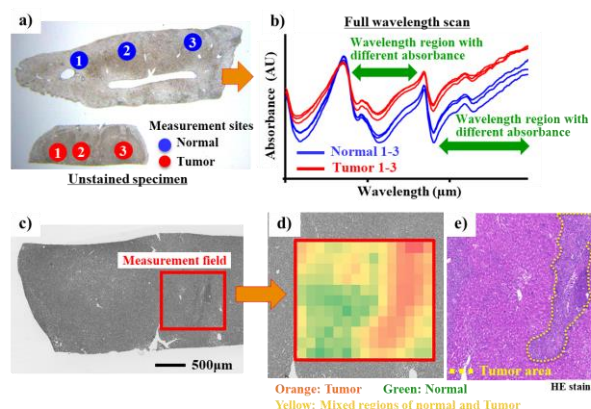


Fig.3. The spectra and visible image from unstained tissue specimens by MIR microscopy in hematopoietic tumor sample.

- Optical micrograph of the unstained tissue specimens of normal liver and hematopoietic tumor invading the liver.
- The corresponding absorbance MIR spectra of the unstained same tissue at three different sites in normal and tumor areas.
- The red line square is irradiation area of MIR laser.
- The MIR imaging of tumor and normal tissue.
- Histological finding of irradiated area in hematopoietic tumor and normal liver tissue.

mixed regions of the tumor cell and normal liver tissue, indicated by yellow color.

2. Epithelial tumor

A malignant epithelial tumor including benign hematopoietic tumor lesions and normal liver tissue was analyzed by comparing the cell absorbance with that obtained from an unstained tissue specimen (Fig. 4). Figure 4b illustrates the MIR spectra of the three different color areas (green, blue and red color circles) indicated in Figure 4a. The MIR spectra show that the spectral patterns in the normal (green lines), benign tumor (blue lines), and malignant tumor areas (red lines) differ from each other (Fig. 4b). The largest change in absorbance was observed in the one different region (purple double-headed arrow, Fig. 4b). Next, microscopic mapping was conducted for malignant and benign tumors as well as the normal liver tissue to obtain information on the absorbance of each cell using wavelength showing different absorbance of each other. The malignant epithelial tumor and benign tumor areas were determined by examining the MIR microscopic field (Fig. 4c) compared with the corresponding histopathological views (Fig. 4e). Figure 4d displays the MIR absorbance map of malignant epithelial tumor, benign hematopoietic tumor, and normal liver tissue. The color classification based on the MIR absorbance changes segments four main parts: malignant epithelial tumor, benign hematopoietic tumor, normal liver tissue, and central vein, represented by the pink, green, red, and white ends, respectively.

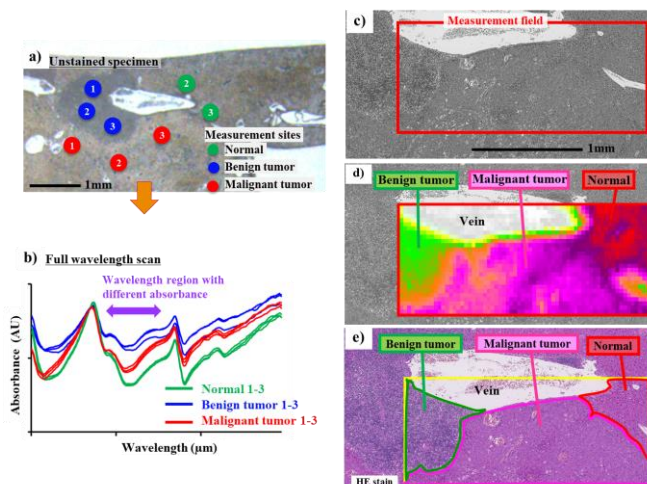


Fig.4. The spectra and visible image from unstained tissue specimens by MIR microscopy in epithelial tumor sample.

- Optical micrograph of the unstained tissue specimens of normal liver, and benign and malignant tumors.
- The corresponding absorbance MIR spectra of the unstained same tissue at three different sites in normal and tumor (benign and malignant tumors) areas.
- The red line square is irradiation area of MIR laser.
- The MIR imaging of normal tissue, vein, and benign and malignant tumors.
- Histological finding of irradiated area in normal liver tissue, vein, and benign and malignant tumors.

3. Non-cancerous lesion (ischemic lesion)

We also examined the discrimination between non-cancerous lesion and normal tissue using the MIR laser. In Figure 5a, the blue and red circles indicate the three different measurement sites by MIR microscopy in the normal muscle and ischemic lesion, respectively. Figure 5b illustrates the MIR spectra of the normal muscle (blue lines) and ischemic lesion (red lines) from three different sites, and shows that the spectral patterns in the ischemic lesion differ from those in the normal muscle. The maximum changes in absorbance are observed in the two different regions (purple double-headed arrows, Fig. 5b). Next, we tried to detect collagen deposit using the picrosirius red stain. The collagen fibers were observed especially around the ischemic lesions (Fig. 5c). Figure 5d displays the MIR absorbance map of the ischemic lesion (necrotic area), collagen

deposit, and normal muscle tissue. The color classification based on the MIR absorbance changes segments three main parts: necrotic area, collagen deposit, and normal muscle tissue, represented by orange, pink, and purple ends, respectively.

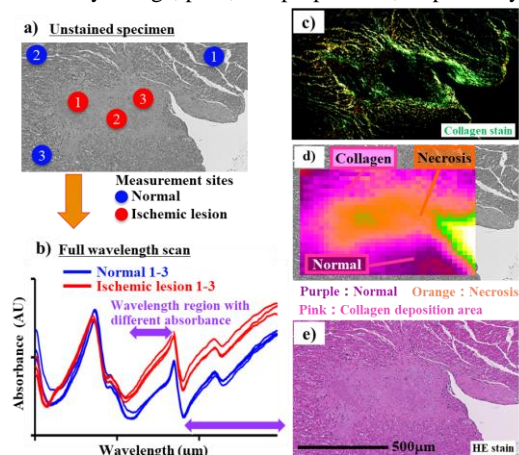


Fig.5. The spectra and visible image from unstained tissue specimens by MIR microscopy in non-cancerous lesion sample.

- Optical micrograph of the unstained tissue specimens of normal muscle and ischemic lesion.
- The corresponding absorbance MIR spectra of the unstained same tissue at three different sites in normal and ischemic areas. The purple double-headed arrows indicate the wavelength region with different absorbance between normal tissue and ischemic lesions.
- The polarized light microscopic view of ischemic lesion stained by picrosirius red. The collagen fibers around the ischemic lesion are easily identified as a green color in the view.
- The MIR imaging of normal muscle, collagen deposit and necrotic area.
- Histological finding of irradiated area in normal muscle, collagen deposit and necrotic area.

Our results suggest that the MIR spectroscopic technique is useful for the diagnosis and discrimination of the differences among lesions such as tumor, non-cancerous lesion and normal tissues based on the MIR absorbance changes. Although there are several advantages of MIR spectroscopy, it is not yet known whether the spectral information from our device can satisfy the pathological diagnostic requirements and assist pathologists in diagnoses. Thus, further investigation and improvements of our MIR spectroscopy are necessary to make these approaches applicable to routine histopathological analysis. In addition, *in vivo* diagnostic tools using the MIR laser are highly required in many fields of medicine. These include endoscopy for guidance of surgical interventions to delineate lesion margins or to replace random biopsies of suspicious tissues by targeted biopsies, which would reduce unnecessary tissue excisions and biopsy-associated risks, or for a detection device in a much earlier stage of carcinogenesis. Future improvements in the MIR laser technology and data analysis will further extend the biomedical applicability and finally result in the implementation of these innovative techniques in the medical field.

Collaborators

K. Ogawa⁴), T. Imaoka^{2,6}), A. Yokoya^{5,6}), and S. Kakinuma²)
 2) Department of Radiation Effects Research, 4) Light Touch Technology Inc., 5) Tokai Quantum Beam Science Center, 6) Group of Quantum and Cellular Systems Biology, QST Advanced Study Laboratory

Acknowledgments

We thank Ms. M. Kaminishi, Y. Nishimura, and M. Shinagawa from the Department of Radiation Effects Research for the preparation of histological samples.

This research is supported by QST President's Strategic Grant (Creative research).

References

- Meier R.J. 2005. *Chem Soc Rev* 34:743-52
- Grasselli J.G., Mehicic M., Mooney J.R. 1986. *Fresen Z Anal Chem* 324:537-43

Research Activities at the Synchrotron Radiation Research Center

Yoshinori Katayama
Synchrotron Radiation Research Center



At the Synchrotron Radiation Research Center (SRRC), we continue to develop a wide range of x-ray techniques for investigating the structural and electronic properties of matter, using as major equipment the two QST beamlines at SPring-8, a large synchrotron radiation facility. As well as precise measurements of high-quality crystalline samples, we have been concentrating on developing techniques that are applicable to inhomogeneous materials, which play important roles in determining the functions of many practical materials. We aim to gain fundamental understanding of functional materials such as semiconductors, superconductors, magnetic materials, dielectric materials, and hydrogen storage materials. The equipment that we develop is open for public use, and in 2019, we accepted forty-one research proposals as a member institute of the Nanotechnology Platform Japan [1].

The SRRC consists of three experimental groups, one theory group, and a beamline operation office (Table 1). The research activities of each research group are summarized below.

Highly brilliant synchrotron/FEL x-ray/VUV facilities are being constructed throughout the world at a rapid pace. In the **Coherent X-ray Research Group**, to stay at the forefront of synchrotron/FEL science, we continue to develop advanced measurement/analysis techniques for the effective use of these new advanced light sources. The use of spatially coherent x-rays from highly brilliant synchrotron/FEL light sources has made it possible to visualize the inhomogeneity inside matter. We are now constructing an apparatus for Bragg coherent x-ray diffraction imaging (Bragg-CDI) and applying it to the study of inhomogeneous structures of sub-micrometer sized ferroelectrics crystals [2].

With the goal of exploiting the temporal coherence and intensity offered by next-generation light sources at short wavelengths, we are aiming to develop new nonlinear and quantum optical techniques using simple atomic systems. We used SACLA's soft x-ray beamline to observe the phenomenon of 'superfluorescence' at extreme ultraviolet wavelengths for the first time. To extend to even shorter wavelengths and for improved pulse control, we are developing a source of superfluid liquid helium droplets for use at SACLA. The new source can also provide an 'ultracold nano laboratory' for studying isolated molecules with synchrotron radiation.

Using a surface x-ray diffractometer coupled with a molecular beam epitaxy chamber, we have carried out in situ measurements of crystal truncation rod (CTR) scattering to investigate the atomic structure of gallium nitride surfaces under growth conditions. From CTR profile analysis, we could experimentally confirm the existence of a pseudo 1x1 structure,

and determine the structure parameters (interlayer distance, coverage, and temperature factor).

The research objectives of the **High Pressure Science and Stress Research Group** are (i) the development of experimental techniques for in-situ measurements under extreme conditions, including high pressure, compressed hydrogen gas environments, and elasto-plastic stress fields, and (ii) fundamental and applied studies of advanced functional materials using the above-mentioned techniques. Group members focus on the study of the nano- to meso-scaled structures of functional materials, and the high-pressure synthesis of novel hydrogen-rich compounds. In order to advance the investigation of the nano- to meso-scaled structures, the group has closely collaborated with the Coherent X-ray Research Group.

Metal-hydrogen systems are a primary research target of this group. In-situ x-ray and neutron diffraction experiments on the Fe-H system at high-pressure revealed the formation of hcpFeH_x, which was absent from the conventional phase diagram [1]. The high-pressure synthesis and crystal structure determination of novel aluminum-based hydrogen-containing compounds have proceeded, and some novel compounds have been synthesized.

Some functionalities of materials arise from not only their periodic crystalline structures but also the local structures. The atomic pair-distribution function (PDF) is one of the powerful tools available to study the local structure. The PDF helped reveal that the enhancement of the negative thermal expansion of Bi(Ni,Fe)O₃ was induced simultaneously by two different kinds of mechanisms [2,3]. Additionally, the local structure of photocatalytic ferric oxide stabilized on mesoporous silica was revealed by the obtained PDF [4].

As a new research direction in this fiscal year, we began to investigate x-ray irradiation effects on tumors for Auger therapy. Tumor spheroids containing Gd-loaded nanoparticles were irradiated by synchrotron radiation monochromatic x-rays. Complete destruction of the tumor spheroid was observed when x-rays with $E = 50.25$ keV, which is just above the Gd K-absorption edge, were used. The result indicates that Auger electrons play a key role for tumor destruction [5].

Furthermore, one group member joined the JSPS KAKENHI Grant-in-Aid for Scientific Research on Innovative Areas "Hypermaterials" project, which started in FY2019, as a co-investigator.

In many functional materials and devices, ranging from high-Tc superconducting oxides to spintronics devices, the spin degrees of freedom of electrons play important roles. In the **Magnetism Research Group**, in order to unveil the functionality of such materials and devices, advanced x-ray spectroscopic techniques, such as nuclear resonant scattering (NRS), resonant

inelastic x-ray scattering (RIXS), and x-ray magnetic circularly polarized emission (XMCPE), are developed. For NRS, frequency-domain synchrotron Mössbauer spectroscopy has been performed by a nuclear Bragg monochromator and nuclear resonance energy analyzers. The micro-Mössbauer beam has realized unique experimental methods including gamma-ray diffraction and total reflection as well as ultra-high-pressure measurements. RIXS has been applied to study electronic states of 5d transition-metal compounds in which strong spin-orbit coupling opens up a new frontier of correlated electron systems. New optical elements for Re L_3 -edge were installed and excitations of 5d electrons in some Re compounds were measured. XMCPE is a brand-new magnetic spectroscopy in the hard x-ray regime, which has the distinctive feature of a large flipping ratio ($\sim 10\%$) for Fe $K\alpha$ emission. A scanning magnetic microscope using XMCPE has been developed. As a new direction, adaptive design of experiment (ADoE) by Gaussian process modeling is being developed for high-throughput x-ray spectroscopy experiments. The introduction of prior knowledge to the ADoE is revealed to enhance the efficiency of the experiment.

The **Condensed Matter Theory Group** develops advanced simulation methods based on quantum mechanics, for investigating theoretically condensed matter by using supercomputers such as K-computer, and performing numerical simulations aimed at understanding various properties of materials such as magnetism, high- T_c superconductivity, and catalytic activity. Furthermore, this work is supported by experiments using x-rays from, for example, SPring-8. Current activities include (i) the development of advanced simulation techniques based on first principles path integral molecular dynamics for investigating the nuclear quantum effects of hydrogen-containing materials such as clathrate hydrates, (ii) the

development of a numerically exact diagonalization method to investigate time-resolved spectroscopies in the Hubbard model describing high- T_c superconductor cuprates, which can provide new insights into their electronic properties, (iii) the development of computational codes to analyze material properties probed by quantum beams, for example, dynamical spin correlations observed by neutron scattering on frustrated magnets [7], RIXS from chiral-lattice materials, and XMCPE from ferromagnets, and (iv) theoretical investigations using large-scale numerical exact diagonalization of quantum spin systems such as the $S = 2$ antiferromagnetic chain and the Shastry-Sutherland model, which exhibit some novel quantum phases like the symmetry protected topological phase [9].

In FY2019, some experimental apparatuses were rearranged. Operation of the cubic-type multi-anvil press at the first station of BL22XU, a JAEA beamline, was terminated and it was transferred to the materials science research facility for off-line use. The large x-ray diffractometer, which had been operated in the RI Laboratory, replaced it. JAEA transferred their κ -type diffractometer from BL14B1, a QST beamline, to the RI Laboratory for studies on fuel debris in the future.

References

1. <http://www.kansai.qst.go.jp/nano/>
2. K. Ohwada *et al.*, Jpn. J. Appl. Phys. **58**, SLLA05 (2019).
3. A. Machida, *et al.*, Sci. Rep. **9**, 12290 (2019).
4. Y. Sakai, *et al.*, Chem. Mater. **31**, 4748 (2019).
5. T. Nishikubo, *et al.*, J. Am. Chem. Soc. **141**, 19397 (2019).
6. Y. Ide, *et al.*, Chem. Sci. **10**, 6604 (2019).
7. K. Matsumoto, *et al.*, Sci. Rep. **9**, 13275 (2019).
8. T. Nomura *et al.*, J. Phys. Soc. Jpn. **89**, 024704 (2020).
9. T. Sakai *et al.*, Phys. Rev. B **100**, 054407 (2019).

Table 1. Groups at the Synchrotron Radiation Research Center.

Group	Coherent X-ray Research Group	High Pressure Science and Stress Research Group	Magnetism Research Group	Condensed Matter Theory Group
Members	K. Ohwada(GL), J. Harries, T. Sasaki, (M. Takahasi)	T. Watanuki (GL), A. Machida, H. Saitoh, A. Shiro, (R. Yasuda)	T. Inami (GL), T. Mitsui, K. Ishii, T. Ueno, A. Koide, (A. Agui)	(T. Sakai (GL)), T. Ikeda, K. Tsutsui, T. Nomura
Typical Techniques & apparatuses	Coherent x-ray scattering  Surface x-ray diffraction  Quantum optics in EUV region	High-pressure and high-temperature x-ray diffraction  Pair distribution function analysis 	Mössbauer spectroscopy  Resonant inelastic x-ray scattering  X-ray magnetic circularly polarized emission	First-principles molecular dynamics simulations, Numerical calculations 
Research objective	nitride semiconductors, ferroelectrics	hydrogen containing materials, negative thermal expansion materials	magnetism, spintronics, high- T_c superconductivity, adaptive design of experiment	hydrogen containing materials, high- T_c superconductivity, catalysis, magnets
Beamline Operation Office/Y. Katayama(Section Manager), Y. Teraoka, Y. Kai, K. Sugawara				

Structural analysis of III-V compound semiconductors by *in situ* synchrotron X-ray reciprocal space mapping

Takuo Sasaki



Coherent X-ray Research Group, Synchrotron Radiation Research Center

InGaAs is among the few materials with a wide-range band gap that is easily controlled by tuning the In/Ga compositional ratio. By virtue of these properties, InGaAs is an attractive material for heterojunction transistors, light emitting diodes, and sub-cells of multi-junction solar cells. However, appropriate foreign substrates for InGaAs growth are lacking, and thus InGaAs films are usually grown on GaAs(001). The lattice mismatch between InGaAs and GaAs(001) results in a high density of threading dislocations that degrade the cell performance. To overcome this challenge, thick (approximately several microns) buffer layers must be inserted between the film and the substrate, which is time-consuming and costly. Thin InAs films grown on GaAs(111)A substrates present only misfit dislocations at the hetero-interfaces, with no threading dislocations in the films. Moreover, the in-plane lattice parameters of the InAs can be controlled by varying the InAs thickness [1-3]. Hence, InAs/GaAs(111)A is expected to be a virtual substrate replacement for GaAs(001), and can potentially reduce the density of the threading dislocations and the crystal growth duration. For this reason, the strain evolution and indium composition variation in the InGaAs/InAs/GaAs(111)A structure should be analyzed in detail. Such an analysis would provide important knowledge for designing device structures.

Various *in situ* characterization techniques such as x-ray topography, scanning tunneling microscopy (STM), reflection high-energy electron diffraction (RHEED), and optical stress sensors have ever been employed to investigate the strain evolution. However, the changing strain, indium composition, and crystal quality during the growth of InGaAs film can be characterized by *in situ* synchrotron x-ray reciprocal space mapping (*in situ* RSM). Several InGaAs films grown on GaAs(001) substrates have been investigated by this technique [4]. The present study performs an *in situ* RSM of InGaAs films grown on GaAs(111)A [5].

The *in situ* RSM was carried out at the SPring-8 (Beamline 11XU) synchrotron radiation facility using a surface x-ray diffractometer directly coupled to a molecular beam epitaxy (MBE) apparatus, as shown in Fig. 1. The GaAs(111)A $\pm 0.3^\circ$ substrates were mounted on molybdenum blocks and loaded into the MBE chamber. After removing the native oxide layers and growing the GaAs buffer layers, the GaAs(111)A was overgrown with a 100 nm-thick $\text{In}_{0.67}\text{Ga}_{0.33}\text{As}$ layer (Sample A) or a 4 monolayer (ML)-thick InAs layer (Sample B). During growth of the InGaAs layer, the diffracted x-ray signals were collected by a two-dimensional x-ray detector (PILATUS 100K). The measuring time for each RSM was sixteen seconds, corresponding to an InGaAs film growth of 5.9 Å in thickness. This high-speed measurement is comparable to the growth time of a single atomic layer. The energy of the incident x-rays was 10 keV and the beam size was $(0.1 \times 0.1) \text{ mm}^2$.

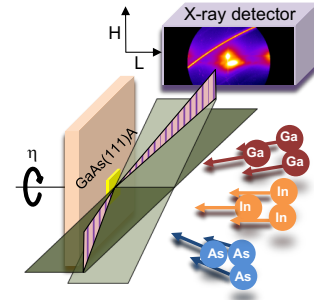


Fig. 1. Schematic illustration of *in situ* RSM during the growth of InGaAs on the GaAs(111)A substrate.

Fig. 2 illustrates the structures of Sample A and B and the typical RSMs of the samples at different growth times. Based on the GaAs-101_{hex} reflections, the RSMs were projected onto the H-L ([100]-[001]) coordinates. The diffraction peaks of the InGaAs layer in both samples were fit by two-dimensional Gaussian functions, thus obtaining the peak positions.

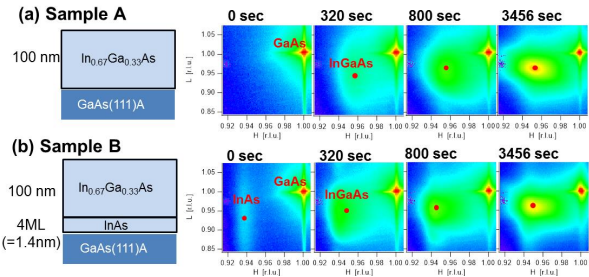


Fig. 2. Schematics of the sample structures and typical RSMs as functions of growth time for (a) Sample A and (b) Sample B.

The variations in the InGaAs lattices were characterized in detail through two different analyses. The first analysis estimated the indium composition and relaxation behaviors (see Fig. 3). Assuming that the InGaAs lattices always deform elastically, the lattice constants ($a_0^{\text{In}_x\text{Ga}_{1-x}\text{As}}$ and $c_0^{\text{In}_x\text{Ga}_{1-x}\text{As}}$) and Poisson's ratio ($\sigma^{\text{In}_x\text{Ga}_{1-x}\text{As}}$) can be determined by Vegard's law. The indium composition (x) was calculated from the measured lattice parameters of InGaAs ($a_m^{\text{In}_x\text{Ga}_{1-x}\text{As}}$ and $c_m^{\text{In}_x\text{Ga}_{1-x}\text{As}}$) using Eq. (1) and (2),

$$\frac{a_m^{\text{In}_x\text{Ga}_{1-x}\text{As}} - c_0^{\text{In}_x\text{Ga}_{1-x}\text{As}}}{c_0^{\text{In}_x\text{Ga}_{1-x}\text{As}}} = \frac{1}{\sigma^{\text{In}_x\text{Ga}_{1-x}\text{As}}} \frac{a_m^{\text{In}_x\text{Ga}_{1-x}\text{As}} - a_0^{\text{In}_x\text{Ga}_{1-x}\text{As}}}{a_0^{\text{In}_x\text{Ga}_{1-x}\text{As}}} \quad (1),$$

and

$$\sigma^{\text{In}_x\text{Ga}_{1-x}\text{As}} = \frac{c_{11}^{\text{In}_x\text{Ga}_{1-x}\text{As}} + 2c_{12}^{\text{In}_x\text{Ga}_{1-x}\text{As}} + 4c_{44}^{\text{In}_x\text{Ga}_{1-x}\text{As}}}{2c_{11}^{\text{In}_x\text{Ga}_{1-x}\text{As}} + 4c_{12}^{\text{In}_x\text{Ga}_{1-x}\text{As}} - 4c_{44}^{\text{In}_x\text{Ga}_{1-x}\text{As}}} \quad (2),$$

where c_{11} , c_{12} , and c_{44} are the elastic coefficients of $\text{In}_x\text{Ga}_{1-x}\text{As}$. The relaxation (R) of InGaAs on GaAs(111)A is then given by Eq. (3),

$$R = \frac{a_m^{GaAs} - a_m^{In_xGa_{1-x}As}}{a_0^{GaAs} - a_0^{In_xGa_{1-x}As}} \times 100 \quad (3),$$

where a_0^{GaAs} is the a -axis lattice parameter of GaAs at the growth temperature (4.01 Å). The second approach estimates the lattice distortion from the c_m -to- a_m ratio. This analysis simplifies the lattice-distortion characteristics at any indium composition. Fig. 3 shows the evolution of the lattice distortion parameter, $c_m/\sqrt{6}a_m$ as a function of the InGaAs thickness for Sample A and B. When $c_m/\sqrt{6}a_m$ is equal to one, the InGaAs lattices are ideal with no distortions or elastic strains.

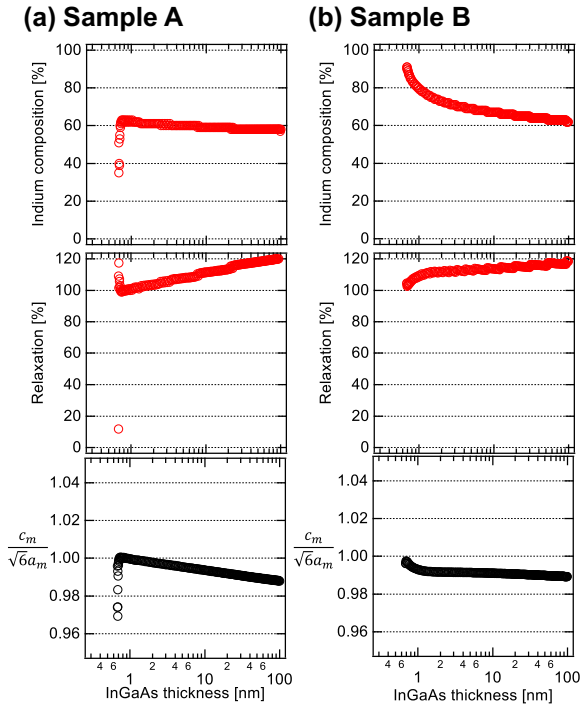


Fig. 3 Evolution of the indium composition, relaxation, and lattice distortion parameter $c_m/\sqrt{6}a_m$ with increasing InGaAs thickness in (a) Sample A and (b) Sample B.

Anomalous shrinkage of the c -axis lattice parameter was observed only in the initial growth phase of Sample A. As shown in Fig. 3(a), the indium composition of this sample was low during the initial growth phase, and rapidly increased until the InGaAs layer was approximately 1 nm thick. Moreover, the relaxation in the early growth phase exceeded 100%, indicating an elastic tensile strain in the InGaAs lattices. Alternatively, the initial $c_m/\sqrt{6}a_m$ was less than one, implying three possible

phenomena: the above-mentioned elastic tensile strain, expansion of the a -axis lattice parameter, or shrinking of the c -axis lattice parameter. Even at low indium compositions, the lattice parameters of InGaAs are always greater than those of GaAs. Therefore, elastic tensile strain is unlikely in the InGaAs lattices, contradicting the assumption of Fig. 3(a) (i.e., that the InGaAs lattices are elastically deformed). During the actual initial growth with a constant indium composition prior to relaxation, a sub-unity $c_m/\sqrt{6}a_m$ can be explained by the expanding lattice parameter along the a -axis or the shrinking lattice parameter along the c -axis of the InGaAs lattices. The former option is nearly eliminated by the existence of GaAs; the a -axis lattice parameter of InGaAs should be the identical to that of GaAs prior to relaxation, limiting anomalous expansion of the a -axis lattice parameter. Therefore, it is likely that only the c -axis lattice parameter shrinks prior to relaxation. Subsequently, the InGaAs lattices are gradually relaxed with a constant indium composition during the initial growth (up to ~ 1 nm). A similarly anomalous shrinkage of the c -axis lattice parameter in the initial growth of InAs/GaAs(111)A was observed in a previous RHEED analysis [6].

In contrast, for Sample B, general elastic deformation with no anomalous distortion appeared during the initial growth of InGaAs. As shown in Fig. 3(b), the indium composition was high in the initial growth phase, and approached the nominal indium composition. Moreover, the relaxation behavior indicates a gradual increase in the elastic tensile strain during the InGaAs growth. Accordingly, $c_m/\sqrt{6}a_m$ decreased slightly near 0.99. These findings suggest that the initial InGaAs lattices grown on InAs/GaAs(111)A cause an elastic tensile strain that gradually increases with decreasing indium composition. Therefore, controlling the InAs growth thickness on GaAs(111)A may be insufficient for growing lattice-matched InGaAs, as it ignores the varying indium composition during the initial growth. This inference provides important knowledge for device design.

References

1. H. Yamaguchi, M. R. Fahy, and B. A. Joyce, Appl. Phys. Lett. **69**, 776 (1996).
2. H. Yamaguchi, J. G. Belk, X. M. Zhang, J. L. Sudijono, M. R. Fahy, T. S. Jones, D. W. Pashley and B. A. Joyce, Phys. Rev. B **55**, 1337 (1997).
3. T. Mano, K. Mitsuishi, N. Ha, A. Ohtake, A. Castellano, S. Sanguinetti, T. Noda, Y. Sakuma, T. Kuroda, and K. Sakoda, Cryst. Growth Des. **16**, 5421 (2016).
4. T. Sasaki, H. Suzuki, A. Sai, J.-H. Lee, M. Takahashi, S. Fujikawa, K. Arafune, I. Kamiya, Y. Ohsihita, and M. Yamaguchi, Appl. Phys. Express **2**, 085501 (2009).
5. T. Sasaki and M. Takahashi, J. Cryst. Growth **512**, 33 (2019).
6. A. Ohtake and M. Ozeki, Phys. Rev. Lett. **84**, 4665 (2000).

In-situ x-ray and neutron diffraction investigation on the formation process of a new phase of iron hydride



Akihiko Machida and Hiroyuki Saitoh

High Pressure Science and Stress Research Group, Synchrotron Radiation Research Center

Iron hydride (FeH_x) has been studied for half a century as a typical transition metal hydride and as a candidate for a hydrogen reservoir inside the Earth. Since FeH_x is stable under high pressures, its temperature (T)-pressure (P) phase diagram and crystal structures have been investigated in the high- T and high- P region with hydrogen up to approximately 1700 K and 20 GPa [1-6]. Three types of structures have been reported on FeH_x : a body centered cubic (bcc), a face centered cubic (fcc) and a double hexagonal close packed (dhcp) metal lattice. The bcc and fcc phases are a solid solution of hydrogen for $x < 1.0$, whereas the dhcp phase is a monohydride for $x \sim 1$. However, hexagonal close-packed (hcp) FeH_x is absent in the conventional phase diagram of the Fe-H system despite the hcp structure being the stable structure of the Fe metal in the same T - P range [7].

Previously, FeH_x was formed by reacting excess hydrogen with Fe in a high-pressure cell, and the phase stability for FeH_x in equilibrium with hydrogen fluid has been investigated. It is considered that the hydrogenation reaction with the excess hydrogen causes the formation of the fcc- and dhcp- FeH_x . When Fe reacts with a lesser amount of hydrogen, a different hydride phase may appear.

In this study, we have investigated the structural properties of the Fe-H system to explore the formation of the hcp- FeH_x at x - T - P conditions using synchrotron radiation (SR) x-rays and neutrons [8]. In-situ SR x-ray diffraction experiments are suitable to find the structural transition at various P - T conditions; however, they are unable to obtain information on the hydrogen atoms located at interstitial sites. On the other hand, neutron diffraction experiments are able to investigate the crystal structure including the site occupancy of hydrogen (deuterium) atoms. Hence, in-situ neutron diffraction under high- T and high- P conditions is the most powerful method to determine the crystal structure of metal hydrides.

In-situ x-ray diffraction experiments were carried out using the high-pressure and high-temperature apparatus installed at BL14B1, SPring-8 [9]. X-ray diffraction profiles were collected using the energy dispersive method. High- P and high- T were generated using a cubic-type multi-anvil press. The pure iron flakes were mixed with BN powder at a volume ratio of 2:3 and compacted into a disc with a size of 0.5 mm in diameter and 0.2 mm in thickness. The sample disc was loaded into the sample capsule with a compacted AlH_3 disc, which served as an internal hydrogen source. The internal hydrogen source, AlH_3 , decomposed into fluid H_2 and Al upon heating above 800 K. In-situ neutron diffraction measurements were carried out using the high-pressure neutron diffractometer PLANET [10] installed at BL11 at the Materials and Life Science Experimental Facility (MLF), J-PARC. High- P and high- T were generated using a six-axis multi-anvil press [11]. The cell assembly for the high- P neutron diffraction measurements was essentially the same as that used for SR x-ray diffraction. A compacted Fe disc with a size of 3 mm in diameter and 2.5 mm in thickness was loaded into the sample capsule with a compacted deuterium source AlD_3 . Details

of the hydrogenation cell, and the in-situ SR x-ray diffraction and neutron diffraction techniques are described elsewhere [6,9].

To prevent the transformation from fcc- FeH_x to dhcp- FeH_x , we controlled the amount of the internal hydrogen source AlH_3 , which was reduced to an H/Fe molar ratio of approximately 0.6. Figure 1 shows the SR x-ray diffraction profiles of FeH_x ($x \sim 0.6$) during the cooling process from 1063 K to 298 K at the initial P of approximately 7 GPa. After formation of the fcc- FeH_x at 1073 K, T was decreased at 10 K/min. The x-ray diffraction profile changes at around 797 K indicate formation of the hcp- FeH_x . With further decrease of T , the hcp- FeH_x becomes dominant at around 500 K and decomposes into bcc-Fe and dhcp-FeH at 434 K.

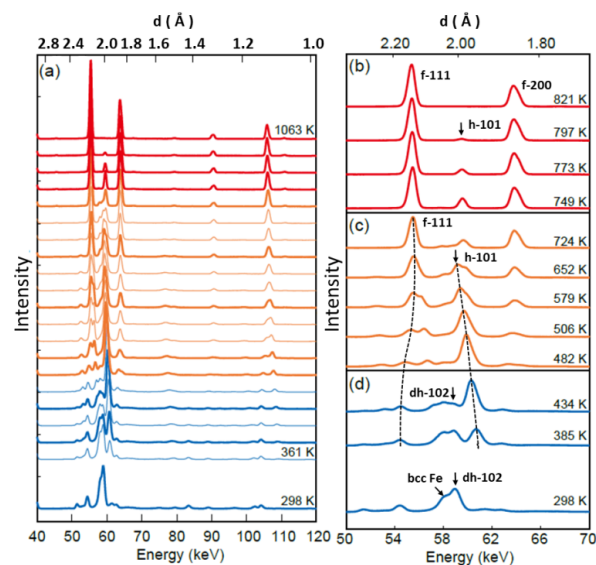


Figure 1. X-ray diffraction profiles of FeH_x during cooling. (a) Overall, (b) fcc-dominant, (c) hcp-dominant, and (d) dhcp-dominant regions, respectively [7].

To determine the occupation site and occupancy of hydrogen (deuterium) atom, the neutron diffraction experiment was performed at high- T and high- P . After the formation of the fcc- FeD_x at 1073 K and 6.0 GPa, T was rapidly decreased to 673 K and the hcp- FeD_x was successfully obtained. T was further decreased to 573 K and finally to 300 K. We analyzed the neutron diffraction profiles by the Rietveld method. The results of Rietveld refinements of the neutron diffraction profiles measured at 673 K-5.1 GPa and 573 K-4.8 GPa by using the hcp structural model reveal that the deuterium atoms randomly occupy the octahedral interstitial sites with occupancies of 0.48.

The series of SR x-ray and neutron diffraction experiments reveal the presence of hcp- FeH_x and its stable P - T region.

Additionally, our results elucidate the crystal structure of hcp-FeH_x including the occupied site and occupancy of hydrogen atoms. We also find that the volume expansion ratio by the hydrogen atom and hydrogen solubility properties of the hcp-FeH_x are different from fcc- and dhcp-FeH_x. From a structural point of view, the fcc, hcp, and dhcp metal lattices can transform into each other by changes in the stacking sequence of the metal planes (Fig. 2). The special arrangements of the interstitial sites also change along this structural transformation. The octahedra consisting of Fe atoms are connected to neighboring octahedra by corner sharing in the fcc lattice and by face-sharing in the hcp lattice. In the dhcp lattice, both corner- and face-sharing are present. The differences in the arrangements of the interstitial sites would influence the hydrogenation properties. This suggests that the bonding state between the hydrogen atom and the surrounding Fe atoms would depend on the lattice structure.

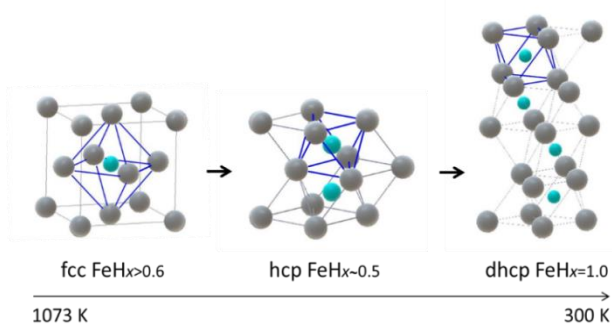


Figure 2. Crystal structures of fcc, hcp, and dhcp-FeH_x. The grey and blue spheres stand for the Fe and H atoms, respectively [8].

Acknowledgments

This work was performed in collaboration with K. Aoki (the University of Tokyo), T. Hattori and A. Sano-Furukawa (JAEA), K. Funakoshi (CROSS), T. Sato, and S. Orimo (Tohoku University). This work was performed under the Inter-university Cooperative Research Program of the Institute for Materials Research, Tohoku University, proposal numbers 16K0075 and 17K0018, and was partially supported by the Grants-in-Aid for Scientific Research, grant numbers JP24241032, JP25220911, and JP18H05224 of the Japan Society for the Promotion of Science.

References

1. Y. Fukai, *Nature* **308**, 174 (1984).
2. K. Sakamaki, *et al.*, *Phys. Earth Planet. Inter.* **174**, 192 (2009).
3. V. E. Antonov, *et al.*, *Scr. Metal* **16**, 203 (1982).
4. V. E. Antonov, *et al.*, *J. Phys. Condens. Matter* **14**, 6427 (2002).
5. Y. Fukai, *et al.*, *J. Alloy Compd.* **348**, 105 (2003).
6. A. Machida, *et al.*, *Nat. Commun.* **5**, 5063 (2014).
7. S. Klotz, *et al.*, *Appl. Phys. Lett.* **93**, 091904 (2008).
8. A. Machida, *et al.*, *Sci. Rep.* **9**, 12290 (2019).
9. H. Saitoh, *et al.*, *Chin. Sci. Bull.* **59**, 5290 (2014).
10. T. Hattori, *et al.*, *Nucl. Instrum. Methods Phys. Res. Sect. A* **780**, 55 (2015).
11. A. Sano-Furukawa, *et al.*, *Rev. Sci. Instrum.* **85**, 113905 (2014).

Charge excitations in electron-doped cuprate superconductors observed with resonant inelastic x-ray scattering: comparison of Cu K -edge with Cu L_3 -edge



Kenji Ishii

Magnetism Research Group, Synchrotron Radiation Research Center

Low-energy electron dynamics in high- T_c cuprates is characterized by the motion of charge and spin. Among the various experimental techniques for studying the electron dynamics, resonant inelastic x-ray scattering (RIXS) has gained immense attention because of its ability to measure electronic excitation spectra with momentum resolution and element selectivity [1,2]. Cu K - and L_3 -edges are mostly used for the RIXS study of the cuprates. Energy resolution has been improved significantly in the last two decades and it reaches a few tens of meV at best at the edges. While spin excitation (single spin-flip process) is allowed only at the L_3 -edge, charge excitation can be observed at both edges.

In the electron-doped cuprate $\text{Nd}_{2-x}\text{Ce}_x\text{CuO}_4$ (NCCO), momentum-dependent charge and spin are indeed observed in the K - [3-5] and L_3 -edge RIXS spectra [5-7]. Magnitude of the experimentally observed dispersion is respectively on the order of the transfer energy ($t \sim 0.4$ eV) and the exchange interaction ($J \sim 0.1$ eV) in the terminology of the t - J model, even though different interpretations, intraband particle-hole excitations [3,5] and a certain mode associated with a symmetry-breaking state [6], were proposed for the charge excitations. Recently, the charge excitations in the L_3 -edge RIXS were found to depend not only on the in-plane momentum but also on the out-of-plane one and ascribed to a plasmon mode [7] which was proposed theoretically [8,9]. In order to further investigate the character of the charge excitations, for example, contrasting behavior at high temperature within a slight difference of carrier concentration (~ 0.02 electron per Cu atom) [6], it is important to verify whether the same excitation is observed at the two edges because each edge has a suited energy-momentum range for observing the excitations. In Ref. [5], the charge excitations at the K -edge are compared with those at the L_3 -edge. However, the comparison is made only at a few momentum points and the out-of-plane momentum is not considered. In this report, we compare in-plane momentum dependence of the Cu K -edge RIXS to that of Cu L_3 -edge RIXS at an equivalent out-of-plane momentum and conclude that the momentum-dependent charge excitations in the Cu K -edge RIXS spectra are the same as those in the L_3 -edge.

RIXS experiments were performed at BL11XU of SPring-8. Incident x rays were monochromatized by a Si(111) double-crystal monochromator and a Si(444) channel-cut monochromator, and horizontally scattered x rays were analyzed in energy by a Ge(733) analyzer. Experimental geometry was the same as that in the previous studies [3,5]; π -polarized incident photons with 8991 eV were irradiated on the ab -plane of NCCO, but the energy resolution of 100 meV was improved compared with the previous studies [3-5]. All the spectra were taken at 10 K. We use Miller index (H , K , and L) of the body-centered-tetragonal crystallographic unit cell for momentum transfer (\mathbf{Q}).

Figure 1 shows the Cu K -edge RIXS spectra of NCCO. A

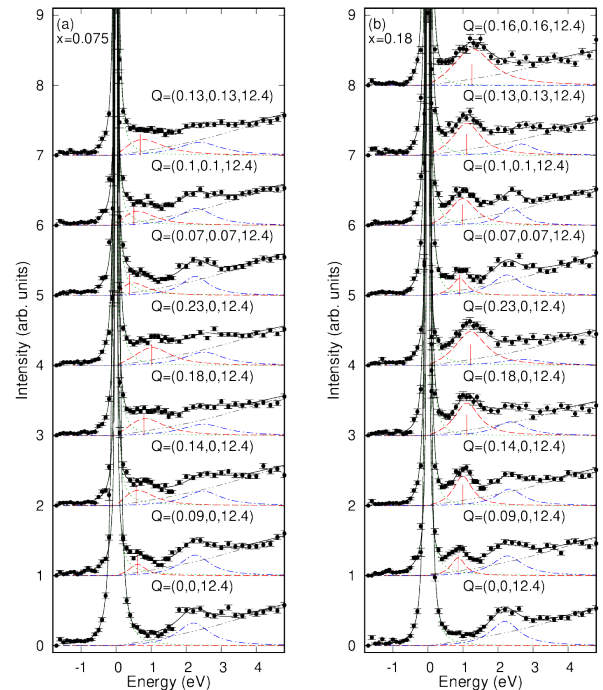


Figure 1: Cu K -edge RIXS spectra of NCCO for (a) $x=0.075$ and (b) $x=0.18$. Filled circles are the experimental data and lines are the fitting results of elastic scattering (dotted green), momentum-dependent charge excitation (dashed red), interband excitation across the charge-transfer gap (dot-dashed blue), tail of high-energy excitation (dot-dot-dashed gray), and sum of the all components (solid black). Peak position of the momentum-dependent charge excitation is indicated by a vertical bar in each spectrum.

peak at 2 eV and a momentum-dependent feature below the peak are consistent with the previous work [3], but the improved energy resolution enables us to observe the latter more clearly, especially at low in-plane momenta (H , K). The 2-eV peak is an interband excitation across the charge-transfer gap and it is also observed in parent Nd_2CuO_4 [4]. By contrast, the momentum-dependent feature appears when electrons are doped. We fit the spectra by the sum of elastic scattering, the momentum-dependent charge excitation, the interband excitation, and a tail of high energy charge excitation peaked around 6 eV [10]. The experimental resolution is considered for the momentum-dependent charge excitation and the interband excitation. Filled circles in Figs. 2(a) and (b) are the peak position and width (full-width at half maximum) of the momentum-dependent feature

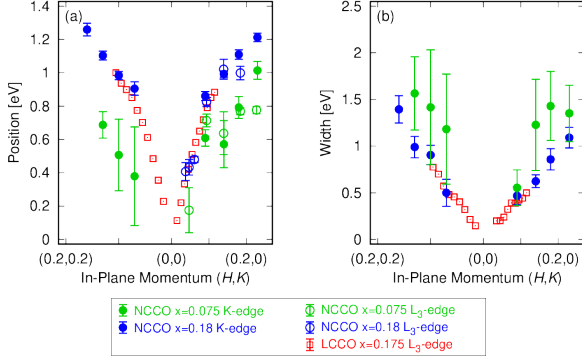


Figure 2: Peak position and width of the momentum-dependent charge excitations in the electron-doped cuprates. Filled circles are the fitting results of the Cu K -edge RIXS in Fig. 1. Open circles and squares are those of the Cu L_3 -edge taken from Refs. 5 and 7, respectively. The width cannot be evaluated reliably in the spectra of Ref. 5 because the tail of the excitation overlaps considerably with the spin and dd excitations due to the low-energy resolution and the experimental condition that is suitable for observing the spin excitations.

obtained from the fitting analysis, respectively. Because the intensity of the feature is approximately proportional to the carrier density, the feature of $x = 0.075$ forms continuum-like spectral shape in contrast to the salient peak in $x = 0.18$. It makes the fitting analysis of $x = 0.075$ difficult; this is the reason for the error being larger than at $x = 0.18$.

Open circles in Fig. 2 (a) are the peak positions in our Cu L_3 -edge study [5], where the crystals from the same batch as this work were used. Momentum transfer along the c^* -direction (L) varies between 1.55 and 1.65 and it is almost equivalent to that in the present data in Fig. 1, considering that the dispersion is folded at even numbers of L [7]. The peak positions are consistent between the Cu K - and L_3 -edges. In addition, we plot the peak positions of $\text{La}_{2-x}\text{Ce}_x\text{CuO}_4$ (LCCO) of $x = 0.175$ and $L = 1.65$ (open squares) taken from a recent study with high energy resolution at the Cu L_3 -edge [7]. Although thin films were used for LCCO, the positions of LCCO $x = 0.175$ agree very well with those of bulk NCCO $x = 0.18$.

Figure 2 shows comparison of the peak width between the K -edge and the L_3 -edge. The momentum dependence of the width of LCCO $x = 0.175$ at the L_3 -edge is connected smoothly to that of NCCO $x = 0.18$ at the K -edge. This implies that the broadening of the peak comes from intrinsic electronic properties of the cuprates rather than some effects in the RIXS process. While momentum-independent lifetime of electron is phenomenologically considered in a theoretical study [9], RIXS can provide experimental data to discuss microscopic origin of the broadening quantitatively.

The excellent agreement of the peak position and width between NCCO $x = 0.18$ and LCCO $x = 0.175$ proves that the momentum-dependent charge excitation in the Cu K -edge RIXS spectra has the same origin as the dispersive mode observed at the Cu L_3 -edge. Our result approves the complementary use of

the two edges for exploring the charge excitations throughout the energy-momentum space. In general, the L_3 -edge is advantageous for the excitations at low energy due to weak elastic scattering while it has limitation of the accessible Brillouin zone. In the case of cuprates, huge dd excitations above 1.5 eV hampers the observation of the charge excitations at the energy. By contrast, the K -edge does not have the shortcomings of the L_3 -edge, but it is difficult to measure the inelastic signal at very low energy. Even though the lower limit in the energy resolution of this study is 0.4–0.5 eV, we will have change to access lower energy if the best resolution (25 meV) is achieved [11]. For hole-doped cuprates, oxygen K -edge is another edge for RIXS as demonstrated very recently [12]. Large dispersion (~ 1 eV) of the charge excitations should be responsible for the metallic conductivity which is a necessary condition for the occurrence of the superconductivity. The remaining issues, such as material dependence and its relation to superconductivity, will be examined by complementary use of RIXS at the edges.

Another finding is that the peak position of the charge excitations shifts to higher energy with increasing electron doping. Although the data of $x = 0.075$ scatter, Fig. 2(a) shows that the peak position of $x = 0.18$ is higher in energy than that of $x = 0.075$. Such doping dependence has been reported in the previous study on L_3 -edge RIXS [7] as a character of plasmon excitation and we confirm it here at the K -edge. Note that doping dependence was measured at a higher in-plane momentum in the previous studies at the K -edge [3,4]; it just shows an increase in the intensity with increasing doping. It may indicate that the high-energy shift is limited at a low in-plane momentum and the doping effect of the charge excitations changes at a certain momentum.

In summary, we performed a Cu K -edge RIXS study of NCCO and analyzed the momentum-dependent charge excitations below the charge transfer gap. The peak position and width agree quite well with those at the Cu L_3 -edge and we conclude that the same charge excitations are observed at the two edges.

Acknowledgments

The author thanks M. Kurooka, Y. Shimizu, M. Fujita, K. Yamada, and J. Mizuki for their collaboration on this work and T. Tohyama and H. Yamase for fruitful discussion on the charge excitations in the cuprate superconductors.

References

1. L. J. P. Ament *et al.*, Rev. Mod. Phys. **83**, 705 (2011).
2. K. Ishii, *et al.*, J. Phys. Soc. Jpn. **82**, 021015 (2013).
3. K. Ishii *et al.*, Phys. Rev. Lett. **94**, 207003 (2005).
4. K. Ishii *et al.*, AIP Conf. Proc. **850**, 403 (2006).
5. K. Ishii *et al.*, Nat. Commun. **5**, 3714 (2014).
6. W. S. Lee *et al.*, Nat. Phys. **10**, 883 (2014).
7. M. Hepting *et al.*, Nature **563**, 374 (2018).
8. A. Greco *et al.*, Phys. Rev. B **94**, 075139 (2016).
9. A. Greco *et al.*, Commun. Phys. **2**, 3 (2019).
10. J. P. Hill *et al.*, Phys. Rev. Lett. **80**, 4967 (1998).
11. D. Ketenoglu *et al.*, J. Synchrotron Radiat. **22**, 961 (2015).
12. K. Ishii *et al.*, Phys. Rev. B **96**, 115148 (2017).

Analysis of magnetic properties of triangular-lattice magnet NiGa₂S₄



Takuji Nomura

Condensed Matter Theory Group, Synchrotron Radiation Research Center

Magnetic properties of an antiferromagnet with a regular triangular lattice unit have been studied with considerable interest, since such a lattice structure with geometrical frustration generally prohibits conventional collinear spin configurations and may realize exotic spin states such as spin liquids. Among regular-triangular lattice magnets, NiGa₂S₄ has been considered as a possible realization of a novel exotic magnetic state with the spin quantum number $S = 1$ [1]. The crystal lattice of NiGa₂S₄ is constructed by stacking NiS₂ layers, each of which is a two-dimensional regular triangular-lattice formed by Ni atoms, separated by a pair of GaS layers. Based on both theoretical and experimental investigations [2], it has been revealed that the electronic and magnetic properties are dominated by the Ni d- e_g electrons near the Fermi energy. If the electron repulsive interaction among the e_g electrons is sufficiently strong, the system should be a Mott insulator with $S = 1$. Then, the nearest-neighbor spins should be coupled with an antiferromagnetic Heisenberg spin interaction $J_1 < 0$.

Results from several experiments suggest that NiGa₂S₄ exhibits unconventional magnetic properties [2]: Among them, neutron scattering revealed that the magnetic correlation evolves below a temperature T^* of approximately 8 K to yield the spatial spin configuration characterized by $\mathbf{Q} = (0.15(5), 0.15(5), 0)$ [3]. Here, it should be noted that this spin configuration is different from the so-called 120-degree ordering conventionally expected for regular triangular-lattice antiferromagnets with nearest-neighbor spin coupling. This led many researchers to take the unusual view that the long-range third nearest-neighbor spin interaction J_3 dominates over the first nearest neighbor J_1 , i.e., $|J_1| < |J_3|$, in contrast to the usual intuition that J_1 is the largest $|J_1| > |J_3|$. More remarkable is that the correlation length, which is estimated from the peak width of the magnetic Bragg peak, does not diverge even at several mK, i.e., no long-range ordering can be attained even at the lowest temperature. The effective magnitude of spin moment at the Ni site was observed to be much reduced ($S = 0.51$) by approximately 49% from $S = 1$. The origin of this significant reduction has been attributed to quantum fluctuations. These observations have clearly distinguished NiGa₂S₄ from conventional magnets.

In this report, a theoretical analysis of these characteristic magnetic properties of NiGa₂S₄ is given, following [4]. First, a DFT-based first-principles electronic structure calculation is performed to obtain the precise electronic structure. Since a band structure calculation is generally not suitable to investigate arbitrary complex spin orderings, we construct a Hubbard-type model by fitting based on the so-called maximally localized Wannier functions (MLWFs). The results of the calculated bands, the fitting, and MLWFs are displayed in Fig. 1. Thus, the 17-orbital (five Ni-d and twelve S-p orbitals) tight-binding model is obtained. Through adding the Ni-site Coulomb interaction (U , U' , and J) to this free-electron model, a Hubbard-type model with a realistic electronic band structure is obtained. To determine the most stable spin configuration, the Hartree-Fock (mean-field) approximation is applied to this model, allowing for spiral ordering states with an arbitrary pitch

vector \mathbf{Q} , where spin moments are given by $\mathbf{m}(\mathbf{r}) = |\mathbf{m}|[\cos\mathbf{Q}\mathbf{r}, \sin\mathbf{Q}\mathbf{r}, 0]$ and are determined by a numerical self-consistent calculation. The most stable ordering state is the one giving the lowest stabilization energy. The calculated stabilization energies as a function of \mathbf{Q} are displayed in Fig. 2 (a) for several strengths of the electron interaction parameter U . As a result, while the conventional 120-degree ordering ($\mathbf{Q} = K = (1/3, 1/3, 0)$) is obtained for weak interaction ($U = 1.6$ eV), the uniform ferromagnetic state ($\mathbf{Q} = \Gamma = 0$) is obtained for strong interaction $U \geq 2.8$ eV. For the intermediate $U = 2$ eV, $\mathbf{Q} = (0.15, 0.15, 0)$ gives the most stable state, which is consistent with the neutron scattering experiment. This value of $U = 2$ eV is quantitatively consistent with our preliminary estimation using the Bethe-Salpeter equation. The calculated ordering spin configuration is depicted in Fig. 2 (b).

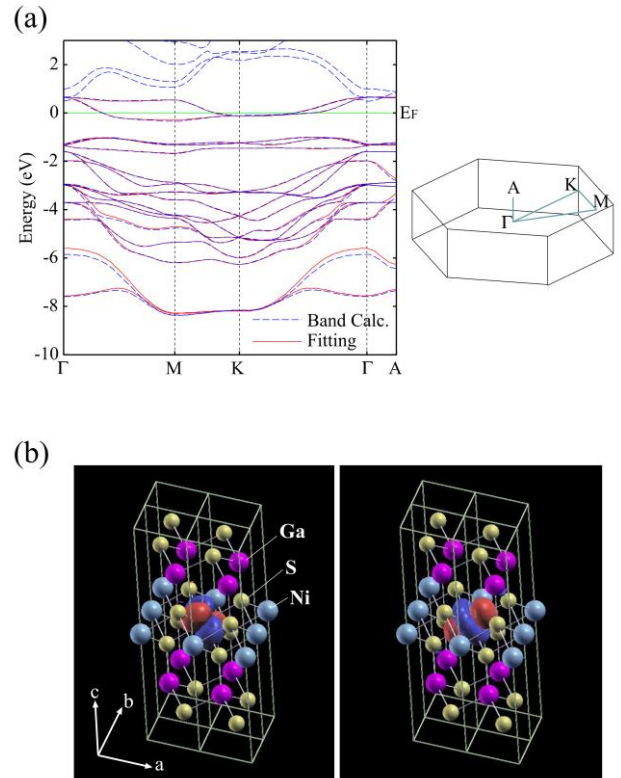


Fig. 1 (a) Calculated electronic band structure and tight-binding fit using MLWFs. On the right, the first Brillouin zone and a symmetry path are depicted. (b) The e_g -type MLWFs at the Ni site.

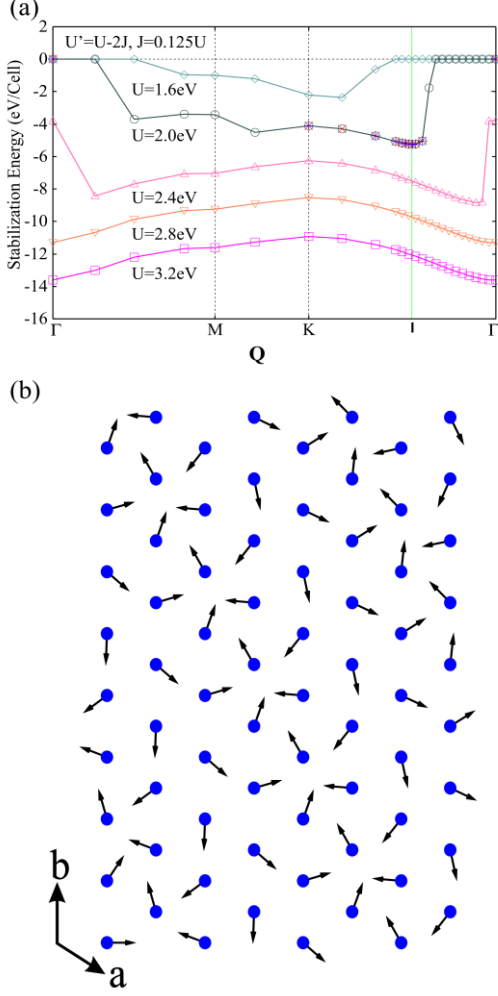


Fig. 2 (a) Calculated stabilization energies for various spin configurations characterized by the wave vector \mathbf{Q} . The vertical solid line indicates the spin configuration $\mathbf{Q} = (0.15, 0.15, 0)$ corresponding to the experimental observation. (b) The calculated most stable spin ordering pattern with $\mathbf{Q} = (0.15, 0.15, 0)$ is depicted, where the filled blue circles represent Ni atoms forming a regular triangular lattice.

The magnitude of the calculated spin moment is $|m| = 1.16\mu_B$, corresponding to $S = 0.58$, which does not significantly deviate from the observed value of $S = 0.51$. Our calculation suggests that this significant reduction of spin moment from $S = 1$ does not originate from exotic quantum fluctuations, instead originating from the Ni-S covalent nature. Based on the mean-field results, we estimated the Heisenberg spin exchange interactions J_n , up to ninth nearest neighbors. According to the results, the first nearest-neighbor J_1 is the largest and ferromagnetic ($J_1 > |J_3| > 0$), in contrast to the results of previous studies based on the localized ionic picture.

Furthermore, the dynamical spin correlation function $S(\mathbf{q}, \omega)$ was calculated (averaged over spin orientations: $S(\mathbf{q}, \omega) = [2S_{ab}(\mathbf{q}, \omega) + S_c(\mathbf{q}, \omega)]/3$) in the magnetic state within the random phase approximation (RPA). The calculated results are displayed in Fig. 3. Here it should be noted that the excitation spectrum is quite different from that of conventional spin waves. In Fig. 3 (b), the experimental peak positions observed by neutron scattering are overlaid onto the calculated intensity map of $S(\mathbf{q}, \omega)$ for comparison. From the results, at low energies below 1.5 meV, the central spectral peak at $\mathbf{q} = \mathbf{Q}$, accompanied by a

pair of weak satellites, originates from the out-of-plane component $S_c(\mathbf{q}, \omega)$, while above 1.5 meV, only the pair of satellites remain, which originate from the in-plane component $S_{ab}(\mathbf{q}, \omega)$. Thus, our results suggest that the magnetic excitation structure is anisotropic and is more complex than usual antiferromagnets. To confirm these results on the spectral properties of $S(\mathbf{q}, \omega)$, further advanced measurements are needed to carefully resolve the in-plane and out-of-plane components, using sufficiently polarized neutron scattering with high-quality single crystals.

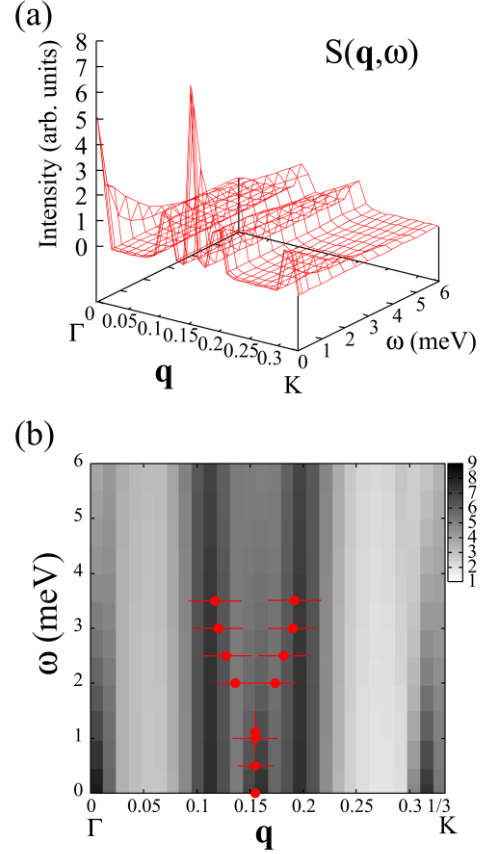


Fig. 3 (a) Calculated spin excitation spectrum $S(\mathbf{q}, \omega)$. (b) The intensity map of $S(\mathbf{q}, \omega)$ is overlaid with the neutron scattering data (plots with error bars) for comparison [3].

Acknowledgments

The author is grateful to Dr. Kenji Yoshii and Mr. Yuji Yamamoto for their contributions.

References

- [1] S. Nakatsuji, Y. Nambu, H. Tonomura, O. Sakai, S. Jonath, C. Broholm, H. Tsunetsugu, Y. Qiu and Y. Maeno, *Science* **309**, 1697 (2005).
- [2] For a review, S. Nakatsuji, Y. Nambu, S. Onoda, *J. Phys. Soc. Jpn.* **79**, 011003 (2010).
- [3] C. Stock, S. Jonas, C. Broholm, S. Nakatsuji, Y. Nambu, K. Onuma, Y. Maeno, and J.-H. Chung, *Phys. Rev. Lett.* **105**, 037402 (2010).
- [4] T. Nomura, Y. Yamamoto and K. Yoshii, *J. Phys. Soc. Jpn.* **89**, 024704 (2020); arXiv:1912.05720.

Construction of a 3 GeV synchrotron radiation facility for soft X-ray application

Utsumi Wataru



Institute for the Advanced Synchrotron Light Source

1. Introduction

The Japanese government has recently decided to build a new 3 GeV-class synchrotron radiation facility in the “Aobayama new campus” of Tohoku University shown in Fig. 1, which is in the Northeast area, Japan. It is a high brilliance light source, electron accelerator system combined with a linear accelerator and a 3 GeV storage ring, which offers highly brilliant lights over a wide spectrum ranging from VUV to X-rays. The key concept of the new synchrotron radiation facility is an “advanced and stable light source to create innovations in science and technology”.

The role in the construction of the facility in the collaboration of public-private regional partnerships has been decided in advance including financial responsibility: QST is responsible for the accelerators, and the partner comprised of the private and regional counterparts is responsible for the buildings, utility and land preparation. Out of the 28 beamline ports of the storage ring, three and seven are dedicated for the first-phase beamlines built by QST and the partner, respectively.

2. Accelerator development

The storage ring of the facility consists of 16 magnet cells with each magnet cell consisting of four bending magnets to bend electron beams, ten quadrupole magnets to focus the electron beam, and ten sextupole magnets to correct aberration.

Since the storage ring has been designed to realize high brilliance reducing the size of the electron beam such as to $6\ \mu\text{m}$ (vertical) and $120\ \mu\text{m}$ (horizontal) with a strong magnet field and is also designed for the storage ring to be compact, high alignment accuracy of the magnet cells and high uniformity of the magnetic fields are required.

We have manufactured a prototype of a half-cell of the magnets shown in Fig. 2, which is constituting the storage ring, and have tested the alignment procedure and magnetic field measurement. In order to achieve a high alignment accuracy, we have employed a vibrating wire monitor, which is a method to monitor vibration of metal wires due to Lorentz force in the magnet field, finding that an alignment accuracy of several microns has been achieved.

In order to achieve a high uniformity of the magnetic fields, we

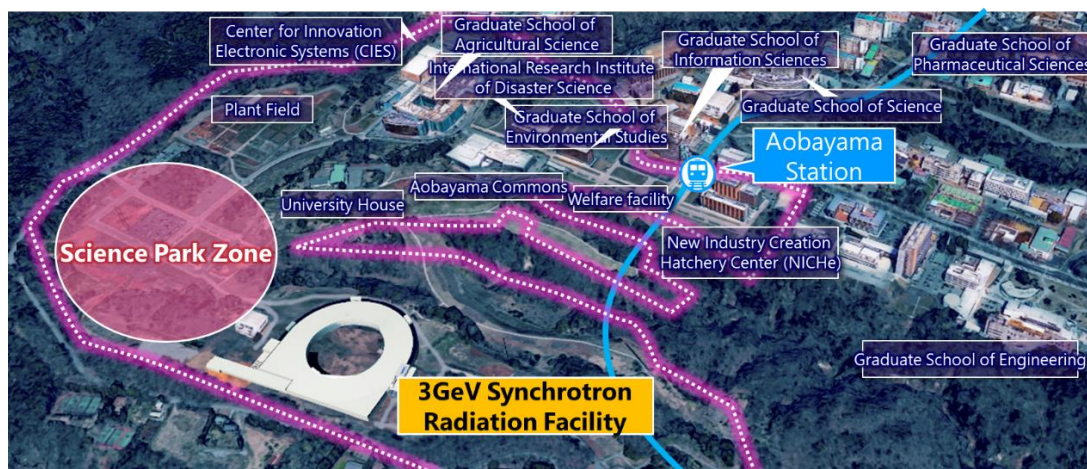


Fig. 1 Construction site of the 3 GeV synchrotron radiation facility



Fig. 2 Prototype of the half-cell of the 3 GeV storage ring

have employed the stretched wire method, which is a method to monitor induced current in the metal wire swept in the magnetic field, finding high uniformity of the magnetic field such as less than 0.1% slope within ± 8 mm.

3. Beamline lineup

Each cell of the storage ring lattice has two straight sections, one of which is 5.44 m and the other is 1.64 m long. Except for four straight sections used for the RF cavities and electron-beam injection, there are 28 sections available for insertion devices. While gap-tunable undulators are placed at the longer straight sections, the shorter straight sections are used for placement of fixed-gap multipole wigglers serving as wide-spectrum light sources.

QST and the partner organized a joint committee to decide the lineup of ten first-phase beamlines. The committee recommended a lineup of ten first-phase beamlines including three public beamlines constructed by QST and seven beamlines that are run in the framework of the coalition concept by the partner.

The public beamlines, which were selected according to the

criteria of high-impact scientific outcomes, are listed in Table 1. These three beamlines will provide both academic and industrial users with a platform for major spectroscopic techniques, such as spin- and angle-resolved photoemission spectroscopy, magnetic circular dichroism and resonant inelastic scattering, opening the way for comprehensive understanding of electronic states of materials.

4. Summary

The project to build a new synchrotron radiation facility has started in 2019 and is scheduled to start operation in 2023. At the beginning, ten beamlines will be operating.

The project is driven by collaboration between QST and the partner with shared responsibility between the two parties. The blue lines representing the development of accelerators and three beamlines show the tasks assigned to QST, and the orange lines representing the construction of the main building and the satellite building, land preparation and the construction of seven beamlines show the partner's tasks.

Table 1. List and specification of the public beamlines

BL Number	BL name	Planned experiments	Insertion device	Energy range (polarization)	Energy resolution	Beam size
BL-VIII	Soft X-ray nanoscale photoemission spectroscopy	<ul style="list-style-type: none"> Nanoscale spin-resolved angle-resolved photoemission spectroscopy 	APPLE undulator	0.05-1.0 keV (circular polarization) 0.05-1.0 keV (horizontal linear polarization) 0.05-1.0 keV (vertical linear polarization)	$E/\Delta E = 10,000-30,000$	50 nm-10 μm
BL-IX	Soft X-ray nanoscale absorption spectroscopy	<ul style="list-style-type: none"> X-ray magnetic circular dichroism X-ray magnetic linear dichroism X-ray magneto-optical Kerr effect X-ray linear dichroism X-ray ferromagnetic resonance spectroscopy 	Segmented APPLE undulator	0.18-2 keV (circular polarization) 0.13-2 keV (horizontal linear polarization) 0.18-2keV (vertical linear polarization)	$E/\Delta E > 10,000$	50 nm-10 μm
BL-X	Soft X-ray superhigh-resolution resonant inelastic scattering	<ul style="list-style-type: none"> Superhigh-resolution resonant inelastic X-ray scattering 	APPLE undulator	0.25-1.0 keV (circular polarization) 0.25-1.0 keV (horizontal linear polarization) 0.25-1.0 keV (vertical linear polarization)	$E/\Delta E > 150,000$	< 500 nm

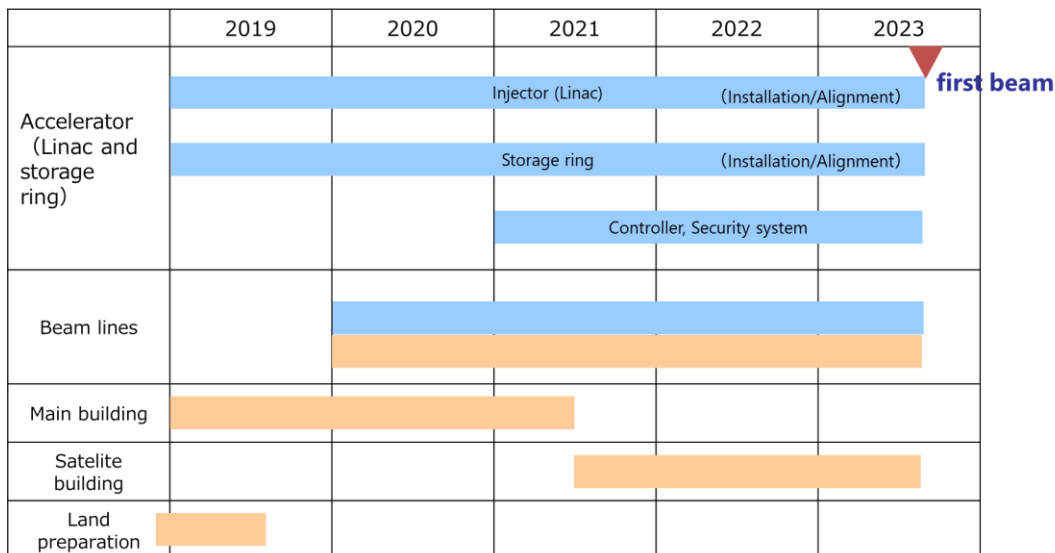
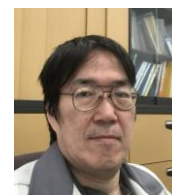


Fig. 3 Schedule of constructing the 3 GeV synchrotron radiation facility

Research Activities of Institute of Quantum Life Science at KPSI



Naoya Shikazono

Institute for Quantum Life Science

Quantum life science has emerged to explore the new frontiers in biology from the perspective of the level of quantum to describe dynamics and functions of cells and organisms. The Institute of Quantum Life Science at QST was established in April 2019 to pioneer a new field in life sciences. Investigations at the Institute of Quantum Life Science are expected to proceed through two approaches: one is to determine whether quantum mechanics plays an essential role in biological systems, and the other approach is to apply the knowledge of quantum science and its technologies to measure physical and chemical parameters, such as temperature, pressure, and pH, at nanoscales inside the cells, or of measurements of the structure and dynamics of biomolecules at an unprecedentedly minute level. Using the above two approaches, the goal of the Institute of Quantum Life Science is to discover the very basic principles of life and to apply the knowledge that is developed during the course of investigation to medical sciences and social activities (Fig. 1). The field of quantum life science is envisaged to produce unanticipated discoveries that will expose the existence of quantum phenomena in nature, ultimately leading to their exploitation in novel knowledge and technologies available to benefit the society. At KPSI, three research groups in the Institute of Quantum Life Science are carrying out their research by conducting experiments and computer simulations (Fig. 1).

The Molecular Modeling and Simulation group aims to understand the *in vivo* function of biomolecules from the atomic level. The group uses computer simulation and bioinformatics together with results obtained by experiments such as crystallographic and scattering data obtained by various types of radiation (X-rays, neutrons, and electrons) and cryo-electron microscopy. The main research target is to determine how the dynamics of protein/DNA/RNA complexes relates with essential cellular functions, such as transcription, translation, replication, and repair. The group has been working on the detailed structure of nucleosomes and has found a clue on why post-translational modifications have such a strong effect on the relaxing and tightening of the nucleosome structure. Another topic that the group has been engaged in is the repositioning of the nucleosome. Nucleosomes are dynamic entities that are repositioned along DNA by chromatin remodeling processes. Nucleosomes repositioned by remodelers often collide with each other and form an intermediate structure called “overlapping dinucleosome.” Using molecular dynamics simulation, the group has revealed the solution structure of the overlapping dinucleosome, in which two nucleosomes are associated. In the overlapping dinucleosome structure, the unusual “hexasome” nucleosome, composed of histone hexamer lacking one H2A-H2B dimer from the conventional histone octamer, was found to contact the canonical “octasome” nucleosome, and the two nucleosomes intimately associate with each other (1). The detailed dynamic structure of overlapping dinucleosome provides important information to understand how nucleosome repositioning occurs during chromatin remodeling, which is a fundamental process for cells to properly

operate and function under various circumstances. This valuable finding is described in detail in the report below.

The main goal for the DNA Damage Chemistry group is to clarify the nature of DNA damage induced by various agents, especially by ionizing radiation. The group aims to utilize new experimental techniques that can unveil the structure of DNA damage as well as damage recognition by DNA repair enzymes at nanometer scales. The group is currently focusing on “clustered DNA damage”, in which two or more DNA lesions are located within one–two helical turns of DNA (within several nanometers along the DNA). Clustered DNA damage is considered to be refractory to repair, and thus, one of the most critical damages induced by ionizing radiation; however, its presence and microstructure has been elusive, as few experimental methods were able to provide some information on spatial distribution of DNA lesions. The group has developed a novel method to detect localized DNA damage by using fluorescence resonance energy transfer (FRET). FRET is known to occur usually within 10 nm. The level of localization of DNA damage was quantified by FRET after labeling DNA damage (abasic sites) by fluorescent dyes. The level of clustering of damage, indicated by the FRET efficiency, increased by ionizing radiation depending on the density of ionization or excitation. The group has proposed another approach for measuring the level of localization of DNA damage, which will be visualized. Atomic force microscopy (AFM) has the resolution at the nanometer/subnanometer scale, so it enables the direct visualization of DNA. The group has labeled DNA damage (abasic sites) by attaching aldehyde reactive probes with biotin to abasic sites, and further binding streptavidin to biotin. The large molecular size of streptavidin enables detection by AFM. Abasic sites are directly induced and further revealed by treating the DNA by DNA glycosylases after irradiation. The result is the first to reveal the complexity of the clustered DNA damage (2). The details of this significant work are shown later in this report.

Mechanism of Mutagenesis group has a goal to elucidate the underlying mechanisms of the induction of mutations, which are strongly relevant to cancer and evolution of life. One aspect of research of the group focuses on the events at very early stages at around femtoseconds to picoseconds within a space in the scale of nanometers after energy transfer from ionizing radiation, especially from ion particles. Using Monte Carlo simulations, the group has demonstrated that, when water is exposed to densely ionizing ion particles, some of the secondary electrons ejected from water molecules cannot escape and are trapped within the electric potential created by the ionized water molecules. This result leads to a realization that the radial dose near the track of a densely ionizing ion particle is much higher than previously thought. This highly localized energy deposition is considered to produce high yield of clustered DNA damage, and thus is an explanation for the drastic effect of ion particles. The conventional view on DNA damage induction is that

ionization and/or excitation of DNA and the radicals generated near the DNA molecule contribute to the formation DNA damage. Building on the simulation result of radial dose, the group is now exploring a possible contribution of heat in the generation of clustered DNA damage. The idea is that an enormous amount of heat deposited near the track would create a pressure wave, which in turn, could result in causing DNA damage.

Quantum life science is related with interactions between dynamical phenomena at extremely short time scales and minute length scales, that is, from atto to femtosecond energy transfer processes at the (sub)nanometer scale. Over the long term, the field of quantum life science is expected to produce unparalleled discoveries based on the significance of quantum phenomena in biological systems. The research of the three groups of the

Institute of Quantum Life Sciences at KPSI has just started to achieve such goals.

References

1. Kato D, Osakabe A, Arimura Y, Mizukami Y, Horikoshi N, Saikusa K, Akashi S, Nishimura Y, Park SY, Nogami J, Maehara K, Ohkawa Y, Matsumoto A, Kono H, Inoue R, Sugiyama M, Kurumizaka H. Crystal structure of the overlapping dinucleosome composed of hexasome and octasome. *Science*. 2017, 356(6334), 205-208
2. Xu X, Nakano T, Tsuda M, Kanamoto R, Hirayama R, Uzawa A, Ide H. Direct observation of damage clustering in irradiated DNA with atomic force microscopy. *Nucleic Acids Res*. 2019, 48(3), e18

Institute of Quantum Life Science

Using cutting-edge quantum technologies and advanced computer simulations, the Institute aims to contribute (1) to the elucidation of the basic principles of life, and in longer term, (2) to the benefit for the everyday life of the society.

Groups at KPSI

Fast processes (~fsec order), Minute regions (~nm order)

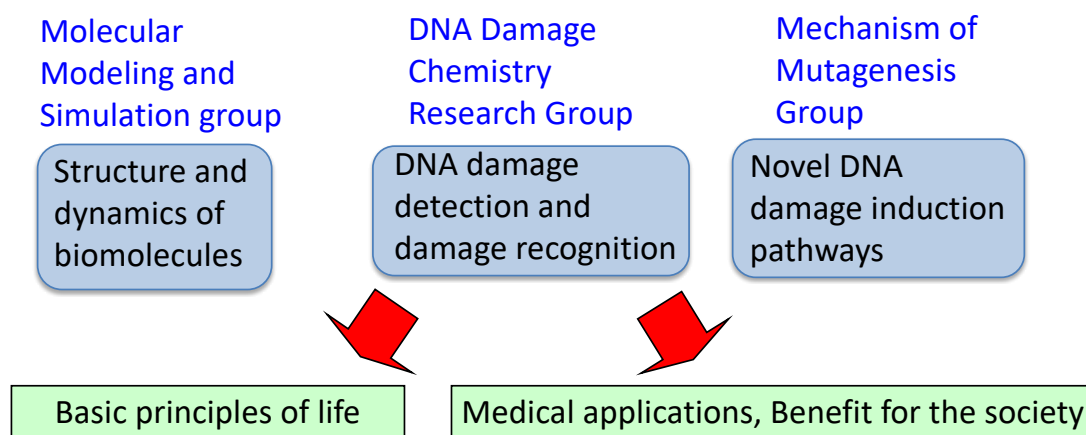


Figure 1.

Structural Studies of Overlapping Dinucleosomes in Solution



Atsushi Matsumoto

Molecular Modeling and Simulation Group, Institute for Quantum Life Science

Nucleosomes are fundamental structural units of chromatin, which enable eukaryotic genomic DNA to be packaged into a nucleus. The canonical nucleosome consists of a histone octamer and approximately 150 base pairs of DNA. The histone octamer is composed of two copies each of histones H2A, H2B, H3, and H4, and the DNA segment tightly wraps around its surface [1]. Nucleosomes are dynamic entities that change their position along genomic DNA (e.g., Segal and Widom [2]). In particular, rearrangement of nucleosome positioning around transcription initiation sites is thought to play a regulatory role in transcription initiation [3]. This nucleosome remodeling process is likely mediated by nucleosome remodeling factors [4, 5]. It has been reported, for example, that if two nucleosomes are closely positioned, one of the nucleosomes will invade the DNA of its neighbor, probably through nucleosome remodeling, and adopt an unusual structure called an overlapping dinucleosome (OLDN) [6, 7].

We previously reconstituted an OLDN and determined its crystal structure [8]. Within the OLDN structure, a histone hexasome lacking an H2A-H2B dimer associates with a canonical octasomal nucleosome, and a 250-base-pair DNA segment wraps around the two histone sub-nucleosomal moieties. In the present study, to understand the structure and dynamics of OLDN in solution, we measured its small-angle X-ray and neutron scattering (SAXS and SANS, respectively) and performed computations to build models of OLDNs that reproduce the scattering data. Recently, biological macromolecules have been measured by SAXS and SANS because of their capability to obtain structural information in solution. In the present study, SAXS was used to examine the overall shape of OLDNs, whereas SANS was employed to separately observe the structures of the elements comprising OLDNs, including the histone proteins and the DNA.

For building the models computationally, we first generated a large number of conformations of OLDNs by simulation using the crystal structure as the initial conformation. The histone proteins have a long string-like structure called histone tails at both ends, which were not observed in the crystal structure probably due to their flexibility. However, to reproduce the experimental SAXS and SANS data well, we found it necessary to include the histone tails in the models (Fig. 1). Thus, we modelled multiple conformations of the histone tails and added them to each model of the OLDN (Fig. 2a).

We then looked for the conformations that well reproduced the SAXS and SANS data. To select appropriate conformations, we used the χ^2 value defined as

$$\chi^2 = \frac{1}{N_p} \sum_{i=1}^{N_p} \left(\frac{I_e(Q_i) - I(Q_i)}{\sigma(Q_i)} \right)^2, \quad (1)$$

where N_p is the number of experimental points Q_i ; $I_e(Q_i)$ and $I(Q_i)$ are the experimental and computed profiles, respectively; $\sigma(Q_i)$ is the experimental error. Smaller χ^2 values indicate better conformations.

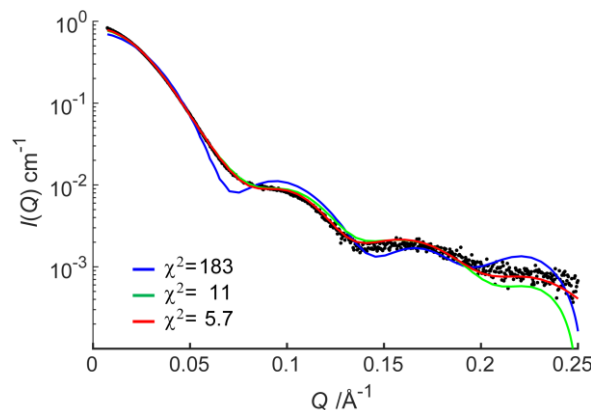


Fig. 1. SAXS profiles for OLDNs. Black dots show the experimental SAXS profile, and a blue line indicates the calculated profile based on the crystal structure (PDB: 5GSE). A green line is the calculated profile for the model with the smallest χ^2 for the SAXS profile in which histone tails were not considered, and a red line is the averaged profile for the model with the smallest χ^2 , where the multiple conformations of the histone tails were considered. Numerical values of χ^2 for the SAXS profile are also shown for the blue, green, and red lines.

Although the SAXS or SANS data individually were not sufficient to uniquely determine the solution conformations of OLDNs, integration of the SAXS and SANS data prevented the model structures from being overfitted to one or the other data set, which enabled us to successfully narrow the size of the conformational ensemble in solution.

Finally, we conducted molecular dynamics (MD) simulations by using each conformation of the ensemble as an initial structure to evaluate the structural stability of OLDNs and investigate their dynamic features in more detail (Fig. 3).

The results indicate that OLDNs adopt a wide variety of conformations in solution, each of which is stabilized by histone tails situated at the interface of the hexameric and octameric histones (Figs. 2 and 3). Furthermore, analysis of the conformations can determine the likely direction of the conformational changes. Such dynamics information may increase our understanding of the assembly and disassembly of OLDNs, which may provide the structural foundation for nucleosome rearrangement within chromatin.

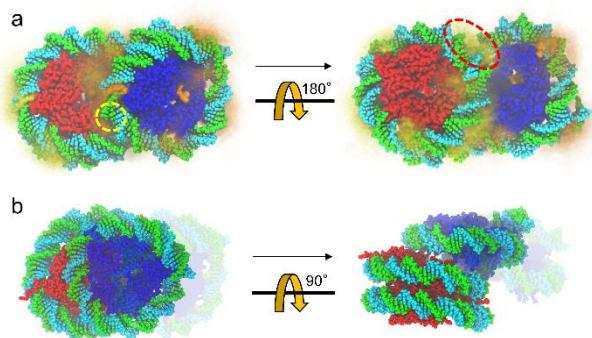


Fig.2. Atomic models of OLDN. Octameric core proteins are shown in red and hexameric in blue. (a) Multiple conformations of histone tails are illustrated by averaging 50 images of the model with histone tails in different conformations viewed from the same angle. The histone tails of the octamer and hexamer are colored in yellow and orange, respectively. Thick orange or yellow indicates that the histone tails are observed frequently in the area. The model has the smallest χ^2 for the SAXS profile among a half million candidate models we analyzed. The dashed circles in yellow and red, respectively, indicate the positions of one of the H4 and H3 histone tails in the octamer. Note that these circles are close to both the hexasomal and octasomal DNA. The H4 histone tail indicated by the yellow circle is mostly beneath the hexasomal DNA. (b) The crystal structure is compared with the model in (a). The octameric core proteins (red) are superimposed on each other. The computational model is represented with light colors. The RMSD between the two structures, excluding the histone tails atoms, was 19.6 Å.

Acknowledgments

This work was performed in collaboration with Dr. Hidetoshi Kono and Dr. Zhenhai Li (QST), Dr. Masaaki Sugiyama and Dr. Rintaro Inoue (Kyoto University, Japan), Dr. Anne Martel and Dr. Lionel Porcar (Institut Laue-Langevin, France), Dr. Daiki Kato and Dr. Akihisa Osakabe (Waseda University, Japan), and Dr. Hitoshi Kurumizaka (Waseda University and University of Tokyo, Japan). Molecular graphics were prepared using the software VMD [9]. This work was supported by Grants-in-Aid for Scientific Research (KAKENHI) from Japan Society for the Promotion of Science (JSPS) (18K06101 to A. Matsumoto; JP18H05534, JP18H05229, JP16H01306, and JP15H02042 to M.S.; JP17H01408 to H. Kurumizaka; JP25116003 to H. Kono; and JP18H05534 to H. Kurumizaka and H. Kono) and the Platform Project for Supporting Drug Discovery and Life Science Research from Japan Agency for Medical Research and Development (AMED) JP19am0101076 to H. Kurumizaka and JP19am0101106 (support number 0363) to H. Kono. The SANS experiments at Institut Laue-Langevin (ILL) were performed under proposals No. 8-03-824 (<https://doi.org/10.5291/ILL-DATA.8-03-824>) and No.8-03-884 (<https://doi.org/10.5291/ILL-DATA.8-03-884>), and the SAXS experiments at BL10C were also performed under proposal No. 2015G658. Computations were performed at National Institutes for Quantum and Radiological Science and Technology and at Tokyo Institute of Technology Global Scientific Information and Computing Center.

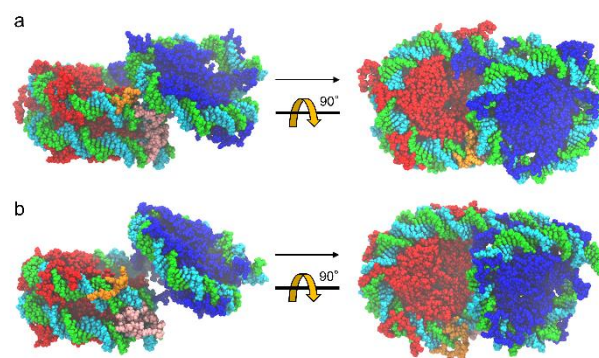


Fig.3. One of the conformations of OLDN during MD simulations in (a) a stable trajectory and (b) an unstable trajectory. Orange: one of the H4 histone tails in the octamer, pink: one of the H3 histone tails in the octamer. These MD simulations suggest that the positively charged histone tails serve as a bridge or glue between two negatively charged DNA sites so that the overall structure will be stabilized.

References

1. Luger, K., et al., *Crystal structure of the nucleosome core particle at 2.8 Å resolution*. *Nature*, 1997. **389**(6648): p. 251-60.
2. Segal, E. and J. Widom, *What controls nucleosome positions?* *Trends Genet*, 2009. **25**(8): p. 335-43.
3. Lai, W.K.M. and B.F. Pugh, *Understanding nucleosome dynamics and their links to gene expression and DNA replication*. *Nat Rev Mol Cell Biol*, 2017. **18**(9): p. 548-562.
4. Clapier, C.R., et al., *Mechanisms of action and regulation of ATP-dependent chromatin-remodelling complexes*. *Nat Rev Mol Cell Biol*, 2017. **18**(7): p. 407-422.
5. Narlikar, G.J., R. Sundaramoorthy, and T. Owen-Hughes, *Mechanisms and functions of ATP-dependent chromatin-remodeling enzymes*. *Cell*, 2013. **154**(3): p. 490-503.
6. Engholm, M., et al., *Nucleosomes can invade DNA territories occupied by their neighbors*. *Nat Struct Mol Biol*, 2009. **16**(2): p. 151-8.
7. Ulyanova, N.P. and G.R. Schnitzler, *Human SWI/SNF generates abundant, structurally altered dinucleosomes on polynucleosomal templates*. *Mol Cell Biol*, 2005. **25**(24): p. 11156-70.
8. Kato, D., et al., *Crystal structure of the overlapping dinucleosome composed of hexasome and octasome*. *Science*, 2017. **356**(6334): p. 205-208.
9. Humphrey, W., A. Dalke, and K. Schulten, *VMD: visual molecular dynamics*. *J Mol Graph*, 1996. **14**(1): p. 33-8, 27-8.

Direct observation of DNA damage using single molecule techniques and future perspectives



Toshiaki Nakano

DNA Damage Chemistry Research Group, Institute for Quantum Life Science

1. Abstract

Clustered DNA damages are defined as two or more lesions that are created by a single radiation track and separated by 20 base pairs. These cluster damages consist of pyrimidine and purine lesions, namely base damages, abasic sites, single-strand breaks, and a combination of these lesions. Other than double-strand breaks, these combinations can occur in the same or opposite strands. These significant biological lesions are hypothesized to challenge the repair machinery and to generate a high mutagenic potential. However, only simple clustered damage containing two or more lesions has been indirectly demonstrated experimentally. Here, we developed a novel method to directly analyze the complexity of clustered DNA damage. The plasmid DNA was irradiated with densely and sparsely ionizing Fe-ion beams and X-rays, respectively. Then, the resulting DNA lesions were labeled with biotin/streptavidin and observed with atomic force microscopy. Fe-ion beams produced complex clustered damage containing two–four lesions. Furthermore, they generated two or three clustered damage sites in a single plasmid molecule that resulted from the hit of a single track of Fe-ion beams. Conversely, X-rays produced a relatively simple clustered damage. The present results provide the first experimental evidence for complex cluster damages.

2. Introduction

2.1. Clustered Damages Induced by Ionizing Radiation

Double-strand breaks (DSBs) consist of two adjacent single-strand breaks (SSBs) on opposite strands of the DNA within 20 base pairs. Ionizing radiation (IR) deposits energy along its track, so the spatial distribution of DNA lesions is not random but localized along the track. Gamma rays induce 10–20 DSB/Gy per cells. Among clustered DNA lesions, DSBs make up approximately 20% of total damages (1). Base lesions are of other types, including abasic (AP) sites and excessive modifications such as 8-oxoguanine (8-oxo-G), 8-oxoadenine (8-oxo-A), thymine glycol (Tg), and DNA-protein crosslinks (2). The most frequent base damage is the AP site, which is formed spontaneously by hydrolysis of the glycoside bond of nucleotides or enzymatically as an intermediate in the base excision repair pathway. Both AP sites and these base damages can form clusters. A double-stranded cluster DNA lesion composed of 8-oxo-7,8-dihydroguanine (8-oxoG), one of the most common oxidized base damages induced by IR. Double-stranded cluster lesions are strongly correlated with structural and DNA helix distortions. Thus, clarifying the quantity and the complexity of clustered DNA damage is key to understanding the biological effect of IR.

2.2. Effects of Clustered Damages Induced by Ionizing Radiation

In general, clustered lesions can cause human mutagenesis, cancer, aging, and neuropathy. The nuclear DNA is the most important cellular target of IR to cause mutations and cell death. While chemicals primarily create single or isolated damage sites, a unique feature of IR-induced DNA damage is made of clustered lesions. In addition, the composition and spatial distribution of DNA lesions induced by IR are highly relevant for subsequent adverse biological effects. This is because the relative biological effectiveness (RBE) of IR, as measured by cell killing, mutagenicity, etc., increases with linear energy transfers (LETs) up to 100–200 keV/μm (3). This increase may be related to the formation of complex clustered DNA damage. The composition and spatial distribution of DNA lesions induced by IR are highly relevant for subsequent adverse biological effects. In cells, reduced repair of clustered DNA damage prolongs the life of lesions in the cluster, causing replication-induced mispairing, increasing mutations, ultimately chromosomal abnormalities, and genetic disorders.

2.3. New Analysis Methods of Clustered Damages

We developed a novel method to visualize individual DNA lesions with atomic force microscopy (AFM) and analyzed clustered DNA damage. We irradiated plasmid DNA with sparsely IR (X-rays) and densely IR (Fe-ion beams) in aqueous solution. Irradiated DNA was treated with DNA glycosylases. The resulting AP sites were labeled with an aldehyde reactive probe (ARP) that has both the alkoxyamine for the reaction with the aldehyde group of DNA and the biotin moiety for the subsequent labeling. Finally, the biotin moiety bound to DNA was tagged with streptavidin (53 kDa), and the resulting ARP–streptavidin complex was visualized with AFM to reveal the spatial distribution of damage along the DNA fiber (Figure 1).

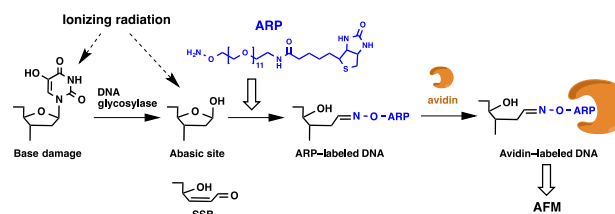


Fig.1 Direct observation of clustered damage by AFM

3. Methods

3.1. Preparation of DNA containing model clustered damage

Plasmid DNA (4 μg) was incubated simultaneously with *Escherichia coli* endonuclease (Endo) III (20 units, New England Biolabs) and human 8-oxoguanine glycosylase (OGG1, 6 units, New England Biolabs) in 20 mM Tris-HCl (pH 8), 1 mM EDTA, 50 mM NaCl, and 1 mM dithiothreitol at 37°C for 1 h. After the reactions, the reaction buffer was changed to TE buffer using a Centri-Sep spin column. DNA was incubated with 5 mM ARP in TE buffer at 37°C for 2 h. Free ARP was removed by a Centri-Sep spin column using phosphate buffered saline (pH 7.5, PBS) as an eluent. Finally, ARP-labeled DNA was incubated with streptavidin in PBS at 37°C for 3 h. Free streptavidin was removed by a Chroma spin TE200 column using TE buffer as an eluent.

3.2. AFM imaging

One microliter of ARP-streptavidin-labeled DNA (2 ng/ μL) was mixed with 1 μL of 40 mM NiCl_2 . The sample (2 μL) was adsorbed onto a freshly cleaved mica plate (ϕ 1.5 mm, Research Institute of Biomolecule Metrology (RIBM) Co. Ltd.) for 5 min at room temperature. Then, the surface was gently washed twice using MilliQ water. AFM images were recorded using a high-speed-scanning AFM system with an ultra-short cantilever. Scanning was performed using the tapping mode in MilliQ water. All images were recorded at an image acquisition speed of 1 frame/s. The DNA damage was quantified by counting the number of streptavidin-DNA complexes in the AFM images. The heights of streptavidin-DNA complexes were measured using IGOR Pro, and complexes with heights of 8–12 nm were considered as DNA damage. The heights of the DNA were 2–4 nm.

4. Results and discussion

4.1. X-rays produce simple clustered damage

pUC19 plasmid DNA (2,686 bp) was irradiated with 200 Gy of X-rays (LET = 1 keV/ μm) in TE buffer under aerobic conditions. The irradiated plasmid DNA was treated with saturating amounts of Endo III and OGG1 that excise oxidized pyrimidine and purine bases, respectively. The types of clustered damage generated by X-rays were DSB (3.55%), two vicinal damaged bases (B/B, 1.93%), DSB with a flanking base damage (DSB/B, 2.42%), and DSB with a flanking base damage on both sides of the DSB (B/DSB/B, 0.323%). AFM images of typical clustered damage by X-rays. Although X-rays also generated two separate clustered damage sites in one plasmid molecule that contained DSB and two vicinal damaged bases (DSB+B/B, 0.161%), where a plus indicates the combination of clustered damages. With X-rays, the complexity of clustered damage was two (DSB and B/B, 5.48%), three (DSB/B, 2.42%), four (B/DSB/B, 0.323%), and two + two (DSB+B/B, 0.161%), indicating that sparsely ionizing X-rays predominantly produce relatively simple clustered damages with the complexity of two and three (3).

4.2 Fe-ion beams produce two types of complex clustered damage

pUC19 plasmid was irradiated with 200 Gy of Fe-ion beams (LET = 200 keV/ μm), labeled with ARP and streptavidin, and observed with AFM as described for X-rays. Irradiation of plasmid resulted in 46.3% undamaged plasmid. Fe-ion beams

produced isolated and clustered damage. Fractions of plasmid ($n = 614$) containing isolated and clustered damage were 39.4% and 14.3%, respectively, showing an increase in the yield of clustered damage relative to that for X-rays. Fe-ion beams produced up to five isolated lesions in one plasmid molecule, but plasmids containing two, three, four, and five isolated lesions (6.4%, 2.0%, 1.1%, and 0.2%, respectively) were relative to that containing 1 isolated lesion (29.8%), indicating that the formation of multiple isolated lesions in one plasmid molecule was a rare event. Interestingly, the spectra of clustered damages associated with Fe-ion beams were dramatically different from those with X-rays. Fe-ion beams generated complex clustered damages, including those containing three vicinal damaged bases (B/B/B), four vicinal damaged bases (B/B/B/B), and DSB with two flanking base damages on one side of the DSB (DSB/B/B). Notably, Fe-ion beams generated multiple clustered damage sites in one plasmid molecule at significant levels. These include plasmids containing a combination of two vicinal damaged bases (B/B + B/B), a combination of three and two vicinal damaged bases (B/B/B + B/B), and three sets of two vicinal damaged bases (B/B + B/B + B/B). In addition, fragments of plasmid containing two complex DSB ends were also observed with Fe-ion beams. Thus, the formation of multiple clustered damage sites in one plasmid molecule was the hallmark of densely ionizing Fe-ion beams and will be an event associated with a single densely ionizing track of Fe-ion beams (3).

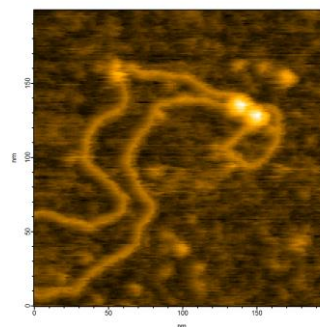


Fig.2 AFM imaging of DNA damage in plasmids irradiated with Fe-ion beams.

5. Future perspectives

DNA lesions in plasmid DNA irradiated with X-rays or Fe-ion beams were specifically labeled with biotin/avidin and directly observed by AFM. The structural complexity of clustered DNA damage was assessed on the basis of the number of DNA lesions per clustered DNA damage site. However, this method is not suitable for the purified DNA from cells or tissue. DNA derived from cells or tissue, unlike plasmids, cannot be observed by AFM because their total length is too long and the number of damages caused is small. To examine the cluster damage that has occurred in DNA purified from cells or tissue, further techniques need to be improved.

Acknowledgments

We wish to thank Dr. K. Akamatsu and Dr. N. Shikazono (QST) for their useful discussions.

References

- [1] Pouget, J.P., et al, Radit. Res., **157**, 589-595 (2002).
- [2] T. Nakano, et al., Free Radic Biol Med **107**, 136-145 (2017).
- [3] X, Xu, et al., Nucleic Acids Res, in press.

Publication List

[Original Papers]

1. Electromagnetic Burst Generation during Annihilation of Magnetic Field in Relativistic Laser-Plasma Interaction
Y. J. Gu, F. Pegoraro, P. V. Sasorov, D. Golovin, A. Yogo, G. Korn, S. Bulanov
Scientific Reports, **9**, 19462-1, 2019-12, DOI:10.1038/s41598-019-55976-0
2. Nonlinear, nondispersive wave equations: Lagrangian and Hamiltonian functions in the hodograph transformation
Francesco Pegoraro, Sergey Bulanov
Physics Letters A, **384**(2), 2020-01, DOI:10.1016/j.physleta.2019.126064
3. Improving Fatigue Performance of Laser-Welded 2024-T3 Aluminum Alloy Using Dry Laser Peening
Tomokazu Sano, Takayuki Eimura, Akio Hirose, Yosuke Kawahito, Seiji Katayama, Kazuto Arakawa, Kiyotaka Masaki, Ayumi Shiro, Takahisa Shobu, Yuji Sano
Metals, **9**(11), 2019-11, DOI:10.3390/met9111192
4. Development of a non-invasive blood sugar sensor
Koichi Yamakawa
Impact, **2019**(8), 38 - 40, 2019-11, DOI:10.21820/23987073.2019.8.38
5. 中赤外レーザーを用いた採血不要の血糖値センサー
山川 考一, 赤羽 温, 青山 誠
日本赤外線学会誌, **29**(2), 45 - 48, 2020-02
6. フェムト秒レーザーアブレーションの軟X線時間分解計測
長谷川 登, 錦野 将元, タンブン ゼン, 石野 雅彦, 南 康夫, 末元 徹
プラズマ・核融合学会誌, **96**(2), 83 - 88, 2020-03
7. 二重露光法による粗大粒材の応力測定
鈴木 賢治, 菖蒲 敬久, 城 鮎美
材料, **68**(4), 312 - 317, 2020-04, DOI:10.2472/jsms.68.312
8. Strong configuration interaction in the 3p photoelectron spectrum of Kr
S. Kosugi, F. Koike, T. Nagayasu, J. Martins, F. Hosseini, M. Oura, T. Gejo, J. Harries, J. D. Bozek, K. Ito, E. Sokell, S. Fritzsche, M. N. Piancastelli, M. Simon
Physical Review A, **101**, 042505, 2020-04, DOI:10.1103/PhysRevA.101.042505
9. Observation of Burst Intensification by Singularity Emitting Radiation generated from relativistic plasma with a high-intensity laser
Akito Sagisaka, Koichi Ogura, Esirkepov Timur, David Neely, Tatiana A. Pikuz, James Kevin Koga, Yuuji Fukuda, Hideyuki Kotaki, Yukio Hayashi, Bruno Gonzalez-Izquierdo, Kai Huang, Sergey Bulanov, Hiromitsu Kiriya, Kiminori Kondo, Tetsuya Kawachi, Masaki Kando, Alexander Pirozhkov
High Energy Density Physics, **36**, 2020-03, DOI:10.1016/j.hedp.2020.100751
10. Status and progress of the J-KAREN-P high intensity laser system at QST
Hiromitsu Kiriya, Alexander Pirozhkov, Mamiko Nishiuchi, Yuuji Fukuda, Koichi Ogura, Akito Sagisaka, Yasuhiro Miyasaka, Hironao Sakaki, Nicholas Peter Dover, Kotaro Kondo, Hazel Frances Lowe, Akira Kon, James Kevin Koga, Esirkepov Timur, Nobuhiko Nakanii, Kai Huang, Masaki Kando, Kiminori Kondo
High Energy Density Physics, **36**, 2020-03, DOI:10.1016/j.hedp.2020.100771
11. Recoil effects on reflection from relativistic mirrors in laser plasmas
P. Valenta, T. Esirkepov, J. K. Koga, A. Pirozhkov, M. Kando, T. Kawachi, Y.-K. Liu, P. Fang, P. Chen, J. Mu, G. Korn, O. Klimo, S. Bulanov
Physics of Plasmas, **27**(3), 2020-03, DOI:10.1063/1.5142084
12. 固体高分子形燃料電池 Pt 触媒の価電子帯電子状態観察による高活性化に関する研究
原田 慈久, 丹羽 秀治, 干鯛 将一, 木内 久雄, 松村 大樹, 石井 賢司
SPRING-8/SACLA 利用研究成果集, **8**(1), 97 - 100, 2020-01, DOI:10.18957/rr.8.1.97

13. 固体高分子形燃料電池カソードに適用される異なる粒径を持つ Pt ナノ粒子の価電子帯電子状態観察による酸素結合エネルギーの解明
原田 慈久, 丹羽 秀治, 干鯛 将一, 宮脇 淳, 尾嶋 正治, 石井 賢司
SPring-8/SACLA 利用研究成果集, **8(1)**, 104 - 107, 2020-01, DOI:10.18957/rr.8.1.104
14. 放射線によるアデノシン三リン酸分子変異によって誘発される生物学的効果
藤井 健太郎, 加藤 大, 藤井 紳一郎, 月本 光俊, 秋光 信佳
X 線分析の進歩, **51**, 251 - 259, 2020-03
15. 共鳴非弾性 X 線散乱を用いた電荷秩序状態からの電荷励起の探索
石井 賢司, 池内 和彦, 脇本 秀一, 藤田 全基, 高山 知弘
SPring-8/SACLA 利用研究成果集, **7(2)**, 192 - 196, 2020-03, DOI:10.18957/rr.7.2.192
16. Haldane Gaps of Large-S Heisenberg Antiferromagnetic Chains and Asymptotic Behavior
H. Nakano, N. Todoroki, T. Sakai
Journal of the Physical Society of Japan, **88(10)**, 114702-1 - 114702-4, 2019-10, DOI:10.7566/JPSJ.88.114702
17. Two magnetization plateaus in the kagome fluoride Ce₂LiTi₃F₁₂
R. Shirakami, H. Ueda, H. O. Jeschke, H. Nakano, S. Kobayashi, A. Matsuo, T. Sakai, N. Katayama, H. Sawa, K. Kindo, C. Michioka, K. Yoshimura
Physical Review B, **100**, 174401-1 - 174401-7, 2019-11, DOI:10.1103/PhysRevB.100.174401
18. Magnetization plateau of the S=2 antiferromagnetic Heisenberg chain with anisotropies
Toru Sakai, Kiyomi Okamoto, Takashi Tonegawa
Physical Review B, **100**, 054407-1 - 054407-6, 2019-08, DOI:10.1103/PhysRevB.100.054407
19. From kagome strip to kagome lattice: Realizations of frustrated S=1/2 antiferromagnets in Ti(III) fluorides
H. O. Jeschke, H. Nakano, T. Sakai
Physical Review B, **99**, 140410(R)-6 - 140410(R)-6, 2019-04, DOI:10.1103/PhysRevB.99.140410
20. Analysis of Rashba Effect on Au(111) Model Surface
Masaki Fujiwara, Nobuyuki Shima, Kenji Makoshi, Toru Sakai
Journal of the Physical Society of Japan, **88(3)**, 034604-1 - 034604-5, 2019-02, DOI:10.7566/JPSJ.88.034604
21. High-Order Harmonics from Laser Irradiated Electron Density Singularity Formed at the Bow Wave in the Laser Plasma
J. Mu, T. Zh. Esirkepov, P. Valenta, T. M. Jeong, Ya. Gu, J. K. Koga, A. S. Pirozhkov, M. Kando, G. Korn, S. V. Bulanov
Physics of Wave Phenomena, **27(4)**, 247 - 256, 2019-12, DOI:10.3103/S1541308X19040010
22. Multiple colliding laser pulses as a basis for studying high-field high-energy physics
J. Magnusson, A. Gonoskov, M. Marklund, T. Zh. Esirkepov, J. K. Koga, K. Kondo, M. Kando, S. V. Bulanov, G. Korn, C. G. R. Geddes, C. B. Schroeder, E. Esarey
Physical Review A, **100**, 063404, 2020-01, DOI:10.1103/PhysRevA.100.063404
23. Sequential Spin State Transition and Intermetallic Charge Transfer in PbCoO₃
Zhehong Liu, Yuki Sakai, Junye Yang, Wenmin Li, Ying Liu, Xubin Ye, Shijun Qin, Jinming Chen, Stefano Agrestini, Kai Chen, Sheng-Chieh Liao, Shu-Chih Haw, Francois Baudalet, Hirofumi Ishii, Takumi Nishikubo, Hayato Ishizaki, Tatsuru Yamamoto, Zhao Pan, Masayuki Fukuda, Kotaro Ohashi, Kana Matsuno, Akihiko Machida, Tetsu Watanuki, Saori I. Kawaguchi, Angel M. Arevalo-Lopez, Changqing Jin, Zhiwei Hu, J. Paul Attfield, Masaki Azuma, Youwen Long
Journal of the American Chemical Society, **142(12)**, 5731 - 5741, 2020-03, DOI:10.1021/jacs.9b13508
24. Weak-coupling Mean-field Theory of Magnetic Properties of NiGa₂S₄
Takuji Nomura, Yuji Yamamoto, Kenji Yoshii
Journal of the Physical Society of Japan, **89(2)**, 024704-1 - 024704-10, 2020-01, DOI:10.7566/JPSJ.89.024704
25. Superstoichiometric hydride PdH_{x < 2} formed by electrochemical synthesis: Dissolution as molecular H₂ proposed
Naoki Fukumuro, Yuh Fukai, Hidehiko Sugimoto, Yasushi Ishii, Hiroyuki Saitoh, Shinji Yae
Journal of Alloys and Compounds, **825**, 153830-1 - 153830-6, 2020-01, DOI:10.1016/j.jallcom.2020.153830

26. Bromine-isotope selective ionization using field-free alignment of IBr isotopologues with a switched nanosecond laser pulse
Hiroshi Akagi, Takayuki Kumada, Tomohito Ootobe, Ryuji Itakura, Hirokazu Hasegawa, Yasuhiro Ohshima
Chemistry Letters, **49(4)**, 416 - 418, 2020-04, DOI:10.1246/cl.200024
27. Experimental investigation on temporal contrast of pre-pulses by post-pulses in a petawatt laser facility
Hiromitsu Kiriyama, Yasuhiro Miyasaka, Akito Sagisaka, Koichi Ogura, Mamiko Nishiuchi, Alexander Pirozhkov, Yuuji Fukuda, Masaki Kando, Kiminori Kondo
Optics Letters, **45(5)**, 1100 - 1103, 2020-02, DOI:10.1364/OL.384759
28. Pressure-Induced Collapse of the Guest Eu Off-Centering in Type-I Clathrate $\text{Eu}_8\text{Ga}_{16}\text{Ge}_{30}$
Naoki Ishimatsu, Kei Yokoyama, Takahiro Onimaru, Toshiro Takabatake, Koichiro Suekuni, Naomi Kawamura, Satoshi Tsutsui, Masaichiro Mizumaki, Toshiaki Ina, Tetsu Watanuki, Vera Cuartero, Olivier Mathon, Sakura Pascarelli, Eiji Nishibori, Tetsuo Irifune
Journal of the Physical Society of Japan, **88(11)**, 4601-1, 2019-11, DOI:10.7566/JPSJ.88.114601
29. Wavelength-dependence of laser excitation process on silicon surface
Tomohito Ootobe
Physical Review Applied, **13**, 024062-1 - 024062-6, 2020-02, DOI:10.1103/PhysRevApplied.13.024062
30. Properties of the H-T phase diagram of the 3-K phase in eutectic Sr_2RuO_4 -Ru: Evidence for chiral superconductivity
Hirono Kaneyasu, Yuya Enokida, Takuji Nomura, Yasumasa Hasegawa, Toru Sakai, Manfred Sigrist
Physical Review B, **100**, 214501-1 - 214501-9, 2019-12, DOI:10.1103/PhysRevB.100.214501
31. Optical parametric oscillator pumped by a 100-kHz burst-mode Yb-doped fiber laser
Keisuke Nagashima, Yoshihiro Ochi, Ryuji Itakura
Optics letters, **45(3)**, 674 - 677, 2020-02, DOI:10.1364/OL.383397
32. Synchrotron-radiation-based Mössbauer absorption spectroscopy with high resonant energy nuclides
Ryo Masuda, Kohei Kusada, Takefumi Yoshida, Shinji Michimura, Yasuhiro Kobayashi, Shinji Kitao, Hiroyuki Tajima, Takaya Mitsui, Hirokazu Kobayashi, Hiroshi Kitagawa, Makoto Seto
Hyperfine Interactions, **240**, 2019-12, DOI:10.1007/s10751-019-1672-x
33. High magnetic field x-ray diffraction study of the α phase of solid oxygen: Absence of giant magnetostriction
Yasuhiro H. Matsuda, Ayumi Shimizu, Akihiko Ikeda, Toshihiro Nomura, Takeshi Yajima, Toshiya Inami, Kohki Takahashi, Tatsuo C. Kobayashi
Physical Review B, **100(21)**, 214105/1 - 214105/7, 2019-12, DOI:10.1103/PhysRevB.100.214105
34. In Situ Synchrotron X-ray Diffraction Reciprocal Space Mapping Measurements in the RF-MBE Growth of GaInN on GaN and InN
Tomohiro Yamaguchi, Takuo Sasaki, Seiji Fujikawa, Masamitsu Takahashi, Tsutomu Araki, Takeyoshi Onuma, Tohru Honda, Yasushi Nanishi
Crystals, **9(12)**, 631-1, 2019-11, DOI:10.3390/cryst9120631
35. Office diagnostic smart hystero-fiberscopy, hysmartscopy, using mobile technology: A single center experience and analysis of diagnostic accuracy
Kana Iwai, Hiroshi Shigetomi, Kiyoshi Oka, Hiroshi Kobayashi
World Academy of Sciences Journal, **1**, 247 - 253, 2019-11, DOI:10.3892/wasj.2019.26
36. Hodograph solutions of the wave equation of nonlinear electrodynamics in the quantum vacuum
Francesco Pegoraro, Sergey Bulanov
Physical Review D, **100**, 036004, 2019-08, DOI:10.1103/PhysRevD.100.036004
37. Synergic Cherenkov-Compton radiation
S. Bulanov, P. Sasorov, S. S. Bulanov, G. Korn
Physical Review D, **100**, 016012, 2019-07, DOI:10.1103/PhysRevD.100.016012
38. Feasibility Study on Application of Synchrotron Radiation μ CT Imaging to Alloy Steel for Non-Destructive Inspection of Inclusions

Yoshinobu Shimamura, Shinya Matsushita, Tomoyuki Fujii, Keiichiro Tohgo, Koichi Akita, Takahisa Shobu, Ayumi Shiro
Metals, **9(5)**, 527, 2019-05, DOI:10.3390/met9050527

39. Electron temperature optimization for efficient water-window soft x-ray emission from discharge-produced highly charged zirconium ions
Hayato Ohashi, Hiroyuki Hara, Bowen Li, Padraig Dunne, Gerry O'Sullivan, Akira Sasaki, Chihiro Suzuki, Naoki Tamura, Hiroyuki A. Sakaue, Daiji Kato, Izumi Murakami, Takeshi Higashiguchi
Journal of Optical Society of America B, **36(12)**, 3555 - 3561, 2019-12, DOI:10.1364/JOSAB.36.003555
40. Analysis of atomistic structural deformation characteristics of calcium silicate hydrate in 53-year-old tricalcium silicate paste using atomic pair distribution function
Sungchul Bae, Hyeonseok Jee, Hyeongwon Seo, Manabu Kanematsu, Ayumi Shiro, Akihiko Machida, Tetsu Watanuki, Takahisa Shobu, Satoshi Morooka, Hiroshi Suzuki
Construction and Building Materials, **237**, 117414, 2019-12, DOI:10.1016/j.conbuildmat.2019.117714
41. Light source based on a 100 mm-long monolithic undulator magnet with a very short 4 mm-period length
Shigeru Yamamoto, Shigeru Kashiwagi, Shinichi Masuda, Nobuhiko Nakanii, Tomonao Hosokai, Masaki Kando, Toshiya Muto, Kenichi Nanbu, Fujio Hinode, Hiroyuki Hama
Journal of Synchrotron Radiation, **26**, 1902 - 1910, 2019-11, DOI:10.1107/S1600577519013031
42. Detecting Crystallographic Lattice Chirality using Resonant Inelastic X-ray Scattering
Sean Mongan, Zengye Huang, Trinanjan Datta, Takuji Nomura, Dao-Xin Yao
Scientific Reports, **9**, 12771-1, 2019-09, DOI:10.1038/s41598-019-49157-2
43. Anomalous small-angle X-ray scattering (ASAXS) study of irradiation-induced nanostructure change in Fe-ion beam irradiated oxide dispersion-strengthened (ODS) steel
Takayuki Kumada, Yojiro Oba, Ryuhei Motokawa, Satoshi Morooka, Aki Tominaga, Hajime Tanida, Takahisa Shobu, Azusa Konno, Kenji Owada, Naoko Oono, Shigeharu Ukai
Journal of Nuclear Materials, **528**, 151890, 2019-11, DOI:10.1016/j.jnucmat.2019.151890
44. Self-supporting tetrahedral amorphous carbon films consisting of multilayered structure prepared using filtered arc deposition
Harigai Toru, Miyamoto Yu, Yamano Masafumi, Tanimoto Tsuyoshi, Suda Yoshiyuki, Takikawa Hirofumi, Kawano Takeshi, Mamiko Nishiuchi, Hironao Sakaki, Kiminori Kondo, Kaneko Satoru, Kunitsugu Shinsuke
Thin Solid Films, **675**, 123 - 127, 2019-04, DOI:10.1016/j.tsf.2019.02.022
45. Mössbauer Spectroscopy Study of $K_xFe_{2-y}Se_2$ under Pressure
Yoshiya Yamamoto, Takaya Mitsui, Shinji Kitao, Makoto Serto, Naoyuki Mizobata, Toshinori Ozaki, Hitoshi Yamaoka
Journal of the Physical Society of Japan, **88(12)**, 124703-1 - 124703-4, 2019-11, DOI:10.7566/JPSJ.88.124703
46. Optimized highly charged ion production for strong soft x-ray sources obeying a quasi-Moseley's law
Yuta Shimada, Hiromu Kawasaki, Kanon Watanabe, Hiroyuki Hara, Kyoya Anraku, Misaki Shoji, Toru Oba, Masaru Matsuda, Weihua Jiang, Atsushi Sunahara, Masaharu Nishikino, Shinichi Namba, Gerry O'Sullivan, Takeshi Higashiguchi
AIP Advances, **9(11)**, 115315, 2019-11, DOI:10.1063/1.5127943
47. Mesoscopic hierarchic polarization structure in relaxor ferroelectrics $Pb[(Mg_{1/3}Nb_{2/3})_{1-x}Ti_x]O_3$
Kazumichi Namikawa, Masahiko Ishino, Mitsuyoshi Matsushita, Kenji Owada, Maki Kishimoto, Jun'ichiro Mizuki, Noboru Hasegawa, Masaharu Nishikino
Physical Review B, **100(18)**, 184110-1 - 184110-7, 2019-11, DOI:10.1103/PhysRevB.100.184110
48. Metallurgical Synthesis of $Mg_2Fe_xSi_{1-x}$ Hydride: Destabilization of Mg_2FeH_6 Nanoconfined in Templated Mg_2Si
Kohta Asano, Hyunjeong Kim, Kouji Sakaki, Yumiko Nakamura, Yongming Wang, Shigehito Isobe, Masaaki Doi, Asaya Fujita, Naoyuki Maejima, Akihiko Machida, Tetsu Watanuki, Ruud J. Westerwaal, Herman Schreuders, Bernard Dam
Inorganic Chemistry, **59(5)**, 2758 - 2764, 2020-03, DOI:10.1021/acs.inorgchem.9b03117
49. Enhanced Negative Thermal Expansion Induced by Simultaneous Charge Transfer and Polar-Nonpolar Transitions
Takumi Nishikubo, Yuki Sakai, Kengo Oka, Tetsu Watanuki, Akihiko Machida, Masaichiro Mizumaki, Koki Maebayashi, Takashi Imai, Takahiro Ogata, Kesuke Yokoyama, Yoichi Okimoto, Shin-ya Koshihara, Hajime Hojo, Takashi Mizokawa, Masaki Azuma
Journal of the American Chemical Society, **141(49)**, 19397 - 19403, 2019-12, DOI:10.1021/jacs.9b10336

50. Resonant-Like Field Enhancement by Nanoscale Grating-Coupled Propagating Surface Plasmons and Localized Surface Plasmons in the Mid-Infrared Range: Implications for Ultrafast Plasmonic Electron Sources
Tomoya Mizuno, Kengo Takeuchi, Keisuke Kaneshima, Nobuhisa Ishii, Teruto Kanai, Jiro Itatani
ACS Applied Nano Materials, **2(11)**, 7067 - 7073, 2019-11, DOI:10.1021/acsnm.9b01597
51. Do SnI₄ molecules deform on heating and pressurization in the low-pressure crystalline phase?
Hiroki Naruta, Kazuhiro Fuchizaki, Daisuke Wakabayashi, Akio Suzuki, Ayako Ohmura, Hiroyuki Saitoh
Journal of Physics: Condensed Matter, **32(5)**, 5401-1, 2020-01, DOI:10.1088/1361-648X/ab4cbc
52. The First Observation of Pure Nuclear Bragg Reflection from Natural Iron α -Fe₂O₃ by Synchrotron Mössbauer Diffraction
Shin Nakamura, Takaya Mitsui, Takaya Mitsui, Yasuhiro Kobayashi, Susumu Shimomura
Journal of the Physical Society of Japan, **88**, 103702, 2019-09, DOI:10.7566/JPSJ.88.103702
53. Order versus disorder: In situ high-pressure structural study of highly polymerized three-dimensional C₆₀ fullerite
A. G. Lyapin, Yoshinori Katayama, V. V. Brazhkin
Journal of Applied Physics, **126(6)**, 065102-1 - 065102-7, 2019-09, DOI:10.1063/1.5111370
54. 高温高圧下の水の構造
片山 芳則, ヤガフアロフ オスカー, 齋藤 寛之
SPring-8/SACLA 利用研究成果集, **7(2)**, 117 - 119, 2019-08, DOI:10.18957/rr.7.2.117
55. Characterization of ionization injection in gas mixtures irradiated by sub-petawatt class laser pulses
Alexey Zhidkov, Naveen Pathak, James Kevin Koga, Kai Huang, Masaki Kando, Tomonao Hosokai
Physical Review Research, **2**, 013216-1 - 013216-12, 2020-02, DOI:10.1103/PhysRevResearch.2.013216
56. Scanning 3D-LiDAR based on visible laser diode for sensor-integrated variable distribution lighting
Masato Ishino, Toshiyuki Kitamura, Akira Takamori, Junichi Kinoshita, Noboru Hasegawa, Masaharu Nishikino, Kazuhisa Yamamoto
Optical Review, **26(1)**, 213 - 220, 2019-09, DOI:10.1007/s10043-018-0483-7
57. Properties of finite amplitude electromagnetic waves propagating in the quantum vacuum
Hedvika Kadlecová, Sergey Bulanov, Georg Korn
Plasma Physics and Controlled Fusion, **61(8)**, 084002, 2019-06, DOI:10.1088/1361-6587/ab21fb
58. Imprint of the stochastic nature of photon emission by electrons on the proton energy spectra in the laser-plasma interaction
Feng Wan, Kun Xue, Zhen-Ke Dou, Karen Z Hatsagortsyan, Wenchao Yan, Danila Khikhlikha, Sergei V Bulanov, Georg Korn, Yong-Tao Zhao, Zhong-Feng Xu, Jian-Xing Li
Plasma Physics and Controlled Fusion, **61**, 084010, 2019-09, DOI:10.1088/1361-6587/ab2b2c
59. Dynamics of relativistic laser-produced plasmas
Sergey Bulanov
Rendiconti Lincei. Scienze Fisiche e Naturali, **30(1)**, 5 - 9, 2019-02, DOI:10.1007/s12210-019-00787-8
60. Electromagnetic shocks in the quantum vacuum
Hedvika Kadlecová, Georg Korn, Sergey Bulanov
Physical Review D, **99(3)**, 036002, 2019-02, DOI:10.1103/PhysRevD.99.036002
61. Real-time observation of electronic, vibrational, and rotational dynamics in nitric oxide with attosecond soft X-ray pulses at 400 eV
Nariyuki Saito, Hiroki Sannohe, Nobuhisa Ishii, Teruto Kanai, Nobuhiro Kosugi, Yi Wu, Andrew Chew, Seunghwoi Han, Zenghu Chang, Jiro Itatani
Optica, **6(12)**, 1542 - 1546, 2019-12, DOI:10.1364/OPTICA.6.001542
62. Pressure and Composition Effects on Sound Velocity and Density of Core-Forming Liquids: Implication to Core Compositions of Terrestrial Planets
Hidenori Terasaki, Attilio Rivoldini, Yuta Shimoyama, Keisuke Nishida, Satoru Urakawa, Mayumi Maki, Fuyuka Kurokawa, Yusaku Takubo, Yuki Shibasaki, Tatsuya Sakamaki, Akihiko Machida, Yuji Higo, Kentaro Uesugi, Akihisa Takeuchi, Tetsu Watanuki, Tadashi Kondo
Journal of Geophysical Research: Planets, **124(8)**, 2272 - 2293, 2019-09, DOI:10.1029/2019JE005936

63. Enhancement of Perpendicular Exchange Bias by Introducing Twin Boundary in Pt/Co/ α -Cr₂O₃/ α -V₂O₃ Epitaxial Film
Yu Shiratsuchi, Saori Yoshida, Satoshi Onoue, Chiharu Mitsumata, Nobuhito Inami, Tetsuro Ueno, Kanta Ono, Ryoichi Nakatani
Materials Transactions, **60(9)**, 2028 - 2032, 2019-09, DOI:10.2320/matertrans.MT-M2019102
64. Effects of rolling and annealing on hydrogen permeability and crystal orientation in Nb-TiNi two-phase alloys
Kazuhiro Ishikawa, Yoshihide Saeki, Yoji Miyajima, Tetsu Watanuki, Akihiko Machida
International Journal of Hydrogen Energy, **44(41)**, 23101 - 23106, 2019-08, DOI:10.1016/j.ijhydene.2019.07.021
65. Polar-Nonpolar Phase Transition Accompanied by Negative Thermal Expansion in Perovskite-Type Bi_{1-x}Pb_xNiO₃
Yuki Sakai, Takumi Nishikubo, Takahiro Ogata, Hayato Ishizaki, Takashi Imai, Masaichiro Mizumaki, Takashi Mizokawa, Akihiko Machida, Tetsu Watanuki, Keisuke Yokoyama, Yoichi Okimoto, Shin-ya Koshihara, Hena Das, Masaki Azuma
Chemistry of Materials, **31(13)**, 4748 - 4758, 2019-07, DOI:10.1021/acs.chemmater.9b00929
66. Condensed ferric dimers for green photocatalytic synthesis of nylon precursors
Yusuke Ide, Satoshi Tominaka, Yumi Yoneno, Kenji Komaguchi, Toshiaki Takei, Hidechika Nishida, Nao Tsunoji, Akihiko Machida, Tsuneji Sano
Chemical Science, **10**, 6604 - 6611, 2019-06, DOI:10.1039/c9sc01253b
67. Hexagonal Close-packed Iron Hydride behind the Conventional Phase Diagram
Akihiko Machida, Hiroyuki Saitoh, Takanori Hattori, Asami Sano-Furukawa, Ken-ichi Funakoshi, Toyoto Sato, Shin-ichi Orimo, Katsutoshi Aoki
Scientific Reports, **9**, 12290, 2019-08, DOI:10.1038/s41598-019-48817-7
68. Destruction of tumor mass by gadolinium-loaded nanoparticles irradiated with monochromatic X-rays: Implications for the Auger therapy
Kotaro Matsumoto, Hiroyuki Saitoh, Tan Le Hoang Doan, Ayumi Shiro, Keigo Nakai, Aoi Komatsu, Masahiko Tsujimoto, Ryo Yasuda, Tetsuya Kawachi, Toshiki Tajima, Fuyuhiko Tamanoi
Scientific Reports, **9**, 13275-1 - 9, 2019-09, DOI:10.1038/s41598-019-49978-1
69. Formation of an Intermediate Valence Icosahedral Quasicrystal in the Au-Sn-Yb System
Tsunetomo Yamada, Yoko Nakamura, Tetsu Watanuki, Akihiko Machida, Masaichiro Mizumaki, Kiyofumi Nitta, Akira Sato, Yoshitaka Matsushita, An-Pang Tsai
Inorganic Chemistry, **58(14)**, 9181 - 9186, 2019-07, DOI:10.1021/acs.inorgchem.9b00801
70. Magnetic Field Induced Triple-q Magnetic Order in Trillium Lattice Antiferromagnet EuPtSi Studied by Resonant X-ray Scattering
Chihiro Tabata, Takeshi Matsumura, Hironori Nakao, Shinji Michimura, Masashi Kakihana, Toshiya Inami, Koji Kaneko, Masato Hedo, Takao Nakama, Yoshichika Onuki
Journal of the Physical Society of Japan, **88(9)**, 093704-1 - 093704-5, 2019-08, DOI:10.7566/JPSJ.88.093704
71. Statistical effects of optical parametric noise on signal pulses in synchronously pumped optical parametric oscillator
Keisuke Nagashima, Yoshihiro Ochi, Ryuji Itakura
Journal of the Optical Society of America B, **36(12)**, 3389 - 3394, 2019-12, DOI:10.1364/JOSAB.36.003389
72. Macroscopic electron-hole distribution in silicon and cubic silicon carbide by the intense laser pulse
Tomohito Otobe
Journal of Applied Physics, **126(20)**, 203101-1 - 203101-7, 2019-11, DOI:10.1063/1.5124424
73. Attosecond electro-optic effect in zinc sulfide induced by a laser field
Tomohito Otobe
Physical Review A, **100**, 033401-1 - 033401-5, 2019-08, DOI:10.1103/PhysRevA.100.033401
74. Angle dependence of dissociative tunneling ionization of NO in asymmetric two-color intense laser fields
Tomoyuki Endo, Hikaru Fujise, Hiroka Hasegawa, Akitaka Matsuda, Mizuho Fushitani, Oleg I. Tolstikhin, Toru Morishita, Akiyoshi Hishikawa
Physical Review A, **100(5)**, 053422, 2019-11, DOI:10.1103/PhysRevA.100.053422

75. Collisionless electrostatic shock acceleration of proton using high intensity laser
Masato Ota, Allesio Morace, Rajesh Kumar, S. Kambayashi, Syunsuke Egashira, Masato Kanasaki, Yuuji Fukuda, Youichi Sakawa
High Energy Density Physics, **33**, 100697-1 - 100697-4, 2019-07, DOI:10.1016/j.hedp.2019.100697
76. Dynamics of the boundary layer created by the explosion of a dense object in an ambient dilute gas triggered by a high power laser
Ryutaro Matsui, Yuuji Fukuda, Yasuaki kishimoto
Physical Review E, **100**(1), 013203-1 - 013203-19, 2019-07, DOI:10.1103/PhysRevE.100.013203
77. Effect of small focus on electron heating and proton acceleration in ultra-relativistic laser-solid interactions
N. P. Dover, M. Nishiuchi, H. Sakaki, K. Kondo, M. A. Alkhimova, A. Ya. Faenov, M. Hata, N. Iwata, H. Kiriyama, J. K. Koga, T. Miyahara, T. A. Pikuz, A. Pirozhkov, A. Sagisaka, Y. Sentoku, Y. Watanabe, M. Kando, K. Kondo
Physical Review Letters, **124**, 084802, 2020-03, DOI:10.1103/PhysRevLett.124.084802
78. Laser resonance frequency analysis: A novel measurement approach to evaluate acetabular cup stability during surgery
Shunsuke Kikuchi, Katsuhiko Mikami, Toshiyuki Kitamura, Noboru Hasegawa, Masaharu Nishikino, Arihiko Kanaji, Masaya Nakamura, Takeo Nagura
Sensors, **22**(19), 4879-1, 2019-11, DOI:10.3390/s19224876
79. Development of an apparatus for Bragg coherent X-ray diffraction imaging, and its application to the three dimensional imaging of BaTiO₃ nano-crystals
Kenji Owada, Kento Sugawara, Tomohiro Abe, Tetsuro Ueno, Akihiko Machida, Tetsu Watanuki, Shintaro Ueno, Ichiro Fujii, Satoshi Wada, Yoshihiro Kuroiwa
Japanese Journal of Applied Physics (Special Issues: Ferroelectric Materials and Their Applications), **58**(SL), SLLA05, 2019-08, DOI:10.7567/1347-4065/ab38dd
80. Application of nuclear emulsions for the identification of multi-MeV protons in laser ion acceleration experiments
Takafumi Asai, Masato Kanasaki, Satoshi Jinno, Nobuko Kitagawa, Nobumichi Shutoh, Satoshi Kodaira, Tomoya Yamauchi, Keiji Oda, Kunihiko Morishima, Yuuji Fukuda
High Energy Density Physics, **32**, 44 - 50, 2019-04, DOI:10.1016/j.hedp.2019.04.002
81. Charge Excitations in Nd_{2-x}Ce_xCuO₄ Observed with Resonant Inelastic X-ray Scattering: Comparison of Cu K-edge with Cu L3-edge
Kenji Ishii, Masahito Kurooka, Yusuke Shimizu, Masaki Fujita, Kazuyoshi Yamada, Junichiro Mizuki
Journal of the Physical Society of Japan, **88**(7), 075001-1 - 075001-2, 2019-07, DOI:10.7566/JPSJ.88.075001
82. The Utility of Applying Various Image Preprocessing Strategies to Reduce the Ambiguity in Deep Learning-Based Clinical Image Diagnosis
Yasuhiko Tachibana, Takayuki Obata, Jeffrey Kershaw, Hironao Sakaki, Takuya Urushihata, Tokuhiko Omatsu, Riwa Kishimoto, Tatsuya Higashi
Magnetic Resonance in Medical Sciences, **19**(2), 92 - 98, 2019-05, DOI:10.2463/mrms.mp.2019-0021
83. Plasma-mirror frequency-resolved optical gating using a liquid-sheet jet in ultraviolet region
Tomoyuki Endo, Masaaki Tsubochi, Ryuji Itakura
Optics Letters, **44**(13), 3234 - 3237, 2019-06, DOI:10.1364/OL.44.003234
84. Variation in electron emission time in weakly nonlinear laser wakefield acceleration
Kai Huang, Hideyuki Kotaki, Koji Mori, Esirkepov Timur, James Kevin Koga, Yukio Hayashi, Nobuhiko Nakanii, Sergey Bulanov, Masaki Kando
Physical Review Accelerators and Beams, **22**(12), 121301-1, 2019-12, DOI:10.1103/PhysRevAccelBeams.22.121301
85. Probing and possible application of the QED vacuum with micro-bubble implosions induced by ultra-intense laser pulses
James K. Koga, Masakatsu Murakami, Alexey V. Arefiev, Yoshihide Nakamiya
Matter and Radiation at Extremes, **4**(3), 034401-1 - 034401-7, 2019-05, DOI:10.1063/1.5086933
86. Probing molecular bond-length using molecular-frame photoelectron angular distributions
H. Fukuzawa, R. R. Lucchese, X. J. Liu, K. Sakai, H. Iwayama, K. Nagaya, K. Kreidi, M. S. Schoffler, J. R. Harries, Y.

Tamenori, Y. Morishita, I. H. Suzuki

The Journal of Chemical Physics, **150**, 174306-1 - 174306-5, 2019-05, DOI:10.1063/1.5091946

87. Relativistic proton emission from ultrahigh-energy-density nanosphere generated by microbubble implosion
M. Murakami, A. Arefiev, M. A. Zosa, James K. Koga, Y. Nakamiya
Physics of Plasmas, **26**, 043112, 2019-04, DOI:10.1063/1.5093043
88. Characterization of 20-fs VUV pulses by plasma-mirror frequency-resolved optical gating
Ryuji Itakura, Hiroshi Akagi, Tomohito Otobe
Optics Letters, **44**(9), 2282 - 2285, 2019-05, DOI:10.1364/OL.44.002282
89. Laser-Particle Collider for Multi-GeV Photon Production
J. Magnusson, A. Gonoskov, M. Marklund, T. Esirkepov, J. K. Koga, K. Kondo, M. Kando, S. V. Bulanov, G. Korn, S. S. Bulanov
Physical Review Letters, **122**(25), 254801, 2019-06, DOI:10.1103/PhysRevLett.122.254801
90. Atomic kinetics calculations of complex highly-charged ions in plasmas in non-local thermodynamic equilibrium by using a Monte-Carlo approach
Akira Sasaki, Richard M. More, Keisuke Fujii, Daiji Kato, Izumi Murakami
High Energy Density Physics, **32**, 1 - 7, 2019-05, DOI:10.1016/j.hedp.2019.04.005
91. Effects of hole-boring and relativistic transparency on particle acceleration in overdense plasma irradiated by short multi-PW laser pulses
Yano Masahiro, Alexey Zhidkov, James Kevin Koga, Hosokai Tomonao, Kodama Ryosuke
Physics of Plasmas, **26**(9), 093108-1 - 093108-8, 2019-09, DOI:10.1063/1.5120068
92. Room-temperature bonding with post-heat treatment for composite Yb:YAG ceramic lasers
Kana Fujioka, Xiaoyang Guo, Momoko Maruyama, Junji Kawanaka, Noriaki Miyanaga
Optical Materials, **91**, 344 - 348, 2019-04, DOI:10.1016/j.optmat.2019.03.032
93. High-order harmonic generation from hybrid organic-inorganic perovskite thin films
Hideki Hirori, Peiju Xia, Yasushi Shinohara, Tomohito Otobe, Yasunari Sanari, Hirokazu Tahara, Nobuhisa Ishii, Jiro Itatani, Kenichi L. Ishikawa, Tomoko Aharen, Masashi Ozaki, Atsushi Wakamiya, Yoshihiko Kanemitsu
APL Materials, **7**, 041107-1 - 041107-4, 2019-04, DOI:10.1063/1.5090935
94. An estimation of line width roughness of photoresists due to photon shot noise for extreme ultraviolet lithography using the percolation model
Akira Sasaki, Masahiko Ishino, Masaharu Nishikino
Japanese Journal of Applied Physics, **58**(5), 055002, 2019-05, DOI:10.7567/1347-4065/ab06bc
95. Controlled Strong Excitation of Silicon as a Step towards Processing Materials at Sub-nanometer Precision
Thanh-Hung Dinh, Nikita Medvedev, Masahiko Ishino, Toshiyuki Kitamura, Noboru Hasegawa, Tomohito Otobe, Takeshi Higashiguchi, Kazuyuki Sakaue, Masakazu Washio, Tadashi Hatano, Akira Kon, Yuya Kubota, Yuichi Inubushi, Shigeki Owada, Tatsunori Shibuya, Beata Ziaja, Masaharu Nishikino
Communications Physics, **2**, 150, 2019-11, DOI:10.1038/s42005-019-0253-2
96. Incident angle and photon energy dependence of polariton lasing in an organic microcavity
Hideyuki Mizuno, Hiroshi Akagi, Masaaki Tsubochi, Ryuji Itakura, Hiroyuki Katsuki, Hisao Yanagi
Japanese Journal of Applied Physics, **58**(5), 052003, 2019-05, DOI:10.7567/1347-4065/ab0507
97. Deformation of an inner valence molecular orbital in ethanol by an intense laser field
Hiroshi Akagi, Tomohito Otobe, Ryuji Itakura
Science Advances, **5**(5), eaaw1885, 2019-05, DOI:10.1126/sciadv.aaw1885
98. High-energy-resolution XANES of layered oxides for sodium-ion battery
Hideharu Niwa, Kazuyuki Higashiyama, Karol Amaha, Wateru Kobayashi, Kenji Ishii, Yutaka Moritomo
Applied Physics Express, **12**(5), 052005-1 - 052005-5, 2019-05, DOI:10.7567/1882-0786/ab10cd
99. Electrochemical Adsorption on Pt Nanoparticles in Alkaline Solution Observed Using In Situ High Energy Resolution X-ray Absorption Spectroscopy

Shogo Kusano, Daiju Matsumura, Kenji Ishii, Hiroshi Tanaka, Jun'ichiro Mizuki
Nanomaterials, **9(4)**, 642, 2019-04, DOI:10.3390/nano9040642

100. Temperature Dependence of the Microscopic Magnetization Process of $Tb_{12}Co_{88}$ using Magnetic Compton Scattering
Akane Agui, Akino Harako, Akane Shibayama, Kento Haishi, Naruki Tsuji, Xiaoxi Liu, Chuang Ma, Hiroshi Sakurai
Journal of Magnetism and Magnetic Materials, **484**, 207 - 211, 2019-08, DOI:10.1016/j.jmmm.2019.04.031
101. Almost pure $J_{\text{eff}} = 1/2$ Mott state of $In_2Ir_2O_7$ in the limit of reduced intersite hopping
Aleksandra Krajewska, Tomohiro Takayama, Robert Dinnebier, Alexander Yaresko, Kenji Ishii, Masahiko Isobe, Hidenori Takagi
Physical Review B, **101(12)**, 121101, 2020-03, DOI:10.1103/PhysRevB.101.121101
102. Ordering of hidden pseudo-dipolar moments in spin-orbital entangled $5d^1$ Ta chlorides
Hajime Ishikawa, Tomohiro Takayama, Reinhard K. Kremer, Juergen Nuss, Robert Dinnebier, Kentaro Kitagawa, Kenji Ishii, Hidenori Takagi
Physical Review B, **100(4)**, 045142-1 - 045142-9, 2019-07, DOI:10.1103/PhysRevB.100.045142
103. Reciprocity between local moments and collective magnetic excitations in the phase diagram of $BaFe_2(As_{1-x}P_x)_2$
Jonathan Pelliciani, Kenji Ishii, Yaobo Huang, Marcus Dantz, Xingye Lu, Paul Olalde-Velasco, Vladimir N. Strocov, Shigeru Kasahara, Lingyi Xing, Xiancheng Wang, Changqing Jin, Yuji Matsuda, Takasada Shibauchi, Tanmoy Das, Thorsten Schmitt
Communications Physics, **2**, 139, 2019-11, DOI:10.1038/s42005-019-0236-3
104. Tyrosyl-DNA phosphodiesterase 2 (TDP2) repairs topoisomerase 1 DNA-protein crosslinks and 3'-blocking lesions in the absence of tyrosyl-DNA phosphodiesterase 1 (TDP1)
Masataka Tsuda, Kaito Kitamasu, Chiho Kumagai, Kazuya Sugiyama, Toshiaki Nakano, Hiroshi Ide
DNA repair, **89**, 102837 - 10248, 2020-03, DOI:https://doi.org/10.1016/j.dnarep.2020.102837
105. Repair of trapped topoisomerase II covalent cleavage complexes: Novel proteasome-independent mechanisms
Tsuda M, Kitamasu K, Hosokawa S, Toshiaki Nakano, Ide H
Nucleosides, Nucleotides & Nucleic Acids, **39(1-3)**, 170-184, 2019-10, DOI:10.1080/15257770.2019.1674332
106. Erratum to "Radial dose distribution model independent of species of incident ions"
Kengo Moribayashi
Nuclear Instruments and Methods in Physics Research Section B: Beam Interactions with Materials and Atoms, **458**, 190 - 195, 2019-08, DOI:10.1016/j.nimb.2019.07.009
107. Heterochromatin protein 1 (HP1): interactions with itself and chromatin components
Amarjeet Kumar, Hidetoshi Kono
Biophysical Reviews, **12(2)**, 387 - 400, 2020-04, DOI:10.1007/s12551-020-00663-y
108. Large-Scale Parallel Implementation of Hartree-Fock Exchange Energy on the Real-Space Grids Using 3D-Parallel FFT
Hideaki Takahashi, Shun Sakuraba, Akihiro Morita
Journal of Chemical Information and Modeling, **60(3)**, 1376 - 1389, 2020-02, DOI:10.1021/acs.jcim.9b01063
109. Structural Studies of Overlapping Dinucleosomes in Solution
Atsushi Matsumoto, Masaaki Sugiyama, Zhenhai Li, Anne Martel, Lionel Porcar, Rintaro Inoue, Daiki Kato, Akihisa Osakabe, Hitoshi Kurumizaka, Hidetoshi Kono
Biophysical Journal, **118**, 1 - 11, 2020-01, DOI:10.1016/j.bpj.2019.12.010
110. Free Energy Profile for Unwrapping Outer Superhelical Turn of CENP-A Nucleosome
Hidetoshi Kono, Shun Sakuraba, Hisashi Ishida
Biophysics and Physicobiology, **16**, 337 - 343, 2019-12, DOI:10.2142/biophysico.16.0_337
111. Histone H3K23-specific acetylation by MORF is coupled to H3K14 acylation
Brianna J. Klein, Suk Min Jang, Catherine Lachance, Wenyi Mi, Shun Sakuraba, Krzysztof Krajewski, Jie Lyu, Wesley W. Wang, Simone Sidoli, Kezhi Yan, Jiuyang Liu, Yi Zhang, Céline Roques, Eric Fournier, Xiaolu Wang, Becka M. Warfield, Xiang-Jiao Yang, Benjamin A. Garcia, Wenshe R. Liu, Wei Li, Brian D. Strahl, Hidetoshi Kono, Xiaobing Shi, Jacques

Côté, Tatiana G. Kutateladze

Nature Communications, **10**, 4724, 2019-10, DOI:10.1038/s41467-019-12551-5

112. Dynamic analysis of ribosome by a movie made from many three-dimensional electron-microscopy density maps
Atsushi Matsumoto
Biophysics and Physicobiology, **16**, 108 - 113, 2019-04, DOI:10.2142/biophysico.16.0_108
113. Balance between DNA-binding affinity and specificity enables selective recognition of longer target sequences in vivo
Sunami Tomoko, Kono Hidetoshi
Protein Science, **28(9)**, 1630 - 1639, 2019-08, DOI:10.1002/pro.3677
114. Role of the photosystem II as an environment on the oxidation free energy of the Mn cluster from S₁ to S₂
Hideaki Takahashi, Daiki Suzuoka, Shun Sakuraba, Akihiro Morita
The Journal of Physical Chemistry B, **123(33)**, 7081 - 7091, 2019-08, DOI:10.1021/acs.jpcc.9b03831
115. Operational experience of a 500 kV photoemission gun
Nobuyuki Nishimori, Ryoji Nagai, Ryoichi Hajima, Masahiro Yamamoto, Yosuke Honda, Tsukasa Miyajima, Takashi Uchiyama
Physical Review Accelerators and Beams, **22(5)**, 053402-1 - 053402-10, 2019-05, DOI:10.1103/PhysRevAccelBeams.22.053402

[Proceedings]

1. Spin Nematic Liquids of the S = 1 Spin Ladder in Magnetic Field
Toru Sakai, Kiyomi Okamoto
JPS Conference Proceedings, **30**, 011083-1 - 011083-6, 2020-03, DOI:10.7566/JPSCP.30.011083
2. Ground-State Phase Diagram of an Anisotropic S = 1 Ferromagnetic– Antiferromagnetic Bond-Alternating Chain
Kiyomi Okamoto, Takashi Tonegawa, Makoto Kaburagi, Toru Sakai
JPS Conference Proceedings, **30**, 011024-1 - 011024-6, 2020-03, DOI:10.7566/JPSCP.30.011024
3. Quantum Phase Transition of the Twisted Spin Tube
Yuta Tachibana, Yuki Ueno, Tomosuke Zenda, Kiyomi Okamoto, Toru Sakai
JPS Conference Proceedings, **30**, 011082-1 - 011082-5, 2020-03, DOI:10.7566/JPSCP.30.011082
4. Quantum Phase Transitions of the Distorted Diamond Spin Chain
Tomosuke Zenda, Yuta Tachibana, Yuki Ueno, Kiyomi Okamoto, Toru Sakai
JPS Conference Proceedings, **30**, 011084-1 - 011084-5, 2020-03, DOI:10.7566/JPSCP.30.011084
5. Magnetization Plateau of the Distorted Diamond Spin Chain
Yuki Ueno, Tomosuke Zenda, Yuta Tachibana, Kiyomi Okamoto, Toru Sakai
JPS Conference Proceedings, **30**, 011085-1 - 011085-5, 2020-03, DOI:10.7566/JPSCP.30.011085
6. Features of Chirality Generated by Paramagnetic Coupling to Magnetic Fields in the 3 K-Phase of Sr₂RuO₄
Hirono Kaneyasu, Yuya Enokida, Takuji Nomura, Yasumasa Hasegawa, Toru Sakai, Manfred Sigrist
JPS Conference Proceedings, **30**, 011039-1 - 011039-6, 2020-03, DOI:10.7566/JPSCP.30.011039
7. High Spectral and Spatial Resolution Soft X-ray/XUV VLS Spectrographs
E. N. Ragozin, A. O. Kolesnikov, A. Pirozhkov, P. V. Sasorov, A. N. Shatokhin
X-Ray Lasers 2018, Springer Proceedings in Physics, **241**, 169 - 174, 2020-03, DOI:10.1007/978-3-030-35453-4_25
8. Stability diagnosis of orthopedic implants based on resonance frequency analysis with fiber transmission of nanosecond laser pulse and acceleration sensor
Katsuhiro Mikami, Daisuke Nakashima, Shunsuke Kikuchi, Toshiyuki Kitamura, Noboru Hasegawa, Takeo Nagura, Masaharu Nishikino
Proceedings of SPIE, **11233**, 112330O, 2020-03, DOI:10.1117/12.2544793

9. Spin Nematic Phase of the Quantum Spin Nanotube
Toru Sakai
JPS Conference Proceedings, **29**, 014004-1 - 014004-5, 2020-02, DOI:10.7566/JPSCP.29.014004
10. Field-Induced Spin Nematic Phase in the S=1 Anisotropic Spin Ladder
Ryo Yamanokuchi, Kiyomi Okamoto, Toru Sakai
2018 16th International Conference on Megagauss Magnetic Field Generation and Related Topics (MEGAGAUSS), , 8722674-1 - 8722674-4, 2019-05, DOI:10.1109/MEGAGAUSS.2018.8722674
11. Sequence-dependent hydration water dynamics of dodecameric DNA
Hiroshi Nakagawa, Yoshiteru Yonetani, Kenji Nakajima, Seiko Ohira-Kawamura, Tatsuya Kikuchi, Yasuhiro Inamura, Mikio Kataoka, Hidetoshi Kono
JPS Conference Proceedings, to be published, 2020-06
12. Non-uniform Distribution of Doped Carrier in a Na-doped CaB₆ Bulk Material Observed by EPMA-SXES
Masami Terauchi, Yohei Sato, Masatoshi Takeda, Tadashi Hatano, Masato Koike, Hiroyuki Sasai, Tetsuya Nagano, Masaru Koeda, Takanori Murano, Hideyuki Takahashi
Microscopy & Microanalysis, **24(S1)**, 746 - 747, 2018-08, DOI:10.1017/S1431927618004221
13. Diffraction Efficiency Measurements of Laminar-Type Diffraction Gratings Overcoated with Lanthanum Series Layers for Boron-K Emission Spectroscopy
Tadashi Hatano, Masato Koike, Masami Terauchi, Alexander Pirozhkov, Nobukazu Hayashi, Hiroyuki Sasai, Tetsuya Nagano
Photon Factory Activity Report (PFACR), **36**, 2019-07
14. Evaluation of Pulse Duration of the Soft X-ray Free Electron Laser at SACLA BL1 with Single-Shot Spectrometry
Y. Kubota, I. Inoue, K. Togawa, R. Kinjo, H. Iwayama, J. Harries, Y. Inubushi, S. Owada, K. Tono, T. Tanaka, T. Hara
2018 16th International Conference on Megagauss Magnetic Field Generation and Related Topics (MEGAGAUSS), 68-71, 2019-05, DOI:10.1109/MEGAGAUSS.2018.8722659

[表彰]

1. 小島 完興
レーザー学会学術講演会第40回年次大会 優秀論文発表賞, 2020-05-29
「次世代小型加速器のためのレーザー駆動イオンの高繰り返し発生」
2. 上野 哲朗
令和元年度関西光科学研究所 所長表彰 創意工夫功労賞, 2020-03-27
磁性・スピントロニクス材料科学ビームライン計画の立案
3. 杉谷 寛弥
結晶工学×ISYSE 合同研究会 研究発表奨励賞, 2019-11-20
「放射光その場 X線回折による InGaN/GaN 多重量子井戸ナノワイヤの構造評価」
4. 菅沼 明夫
令和元年度理事長表彰 模範賞, 2019-07-11
ユーザーへの影響を最小限に抑えたサイクロトロンメインコイルの適切な補修と更新の完遂
5. 杉山 僚
令和元年度理事長表彰 模範賞 特賞, 2019-07-11
量子生命科学領域の創設に関する貢献
6. 長谷川 登、錦野 将元、岡田 大
令和元年度理事長表彰 研究開発功績賞 特賞, 2019-07-01
社会実装に向けた高速レーザー打音検査技術の開発

7. 小島 完興
光・量子ビーム科学合同シンポジウム 2019 (OPTO2019) ベストポスター賞, 2019-06-12
「高時間分解能 FROG を用いた高強度レーザー・プラズマ相互作用面の高速挙動診断」
8. 稲見 俊哉
Journal of the Physical Society of Japan, Award for Most Cited Articles in 2018 from Vol. 86 (2017), 2019-05-27
“Chiral Soliton Lattice Formation in Monoaxial Helimagnet $\text{Yb}(\text{Ni}_{1-x}\text{Cu}_x)_3\text{Al}_9$ ”, J. Phys. Soc. Jpn. **86**, 124702
9. 山川 考一、青山 誠
量子生命科学会第 1 回大会 優秀ポスター発表賞, 2019-05-23
「赤外レーザーの病理学分野への応用の可能性」
10. 坂井 徹
Journal of the Physical Society of Japan, Award for Most Cited Articles in 2018 from Vol. 86 (2017), 2019-05-21
“Ferrimagnetism in the Spin-1/2 Heisenberg Antiferromagnet on a Distorted Triangular Lattice”, J. Phys. Soc. Jpn. **86**, 063702
11. 櫻庭 俊、松本 淳、河野 秀俊、クマール アマラジート
Excellent Presentation Award, National Institutes for Quantum and Radiological Science and Technology (QST), 2019-12-04
“Stable Interdomain Interfaces of Heterochromatin Protein 1: Modeling all-atom Dinucleosome HP1 complex”

[特許登録]

1. 「レーザー装置、光源および測定装置」 特許第 6551898 (2019-07-12)
赤羽 温, 青山 誠, 山川 考一
2. 「ラミナー型回折格子」 特許第 6579371 (2019-09-06)
小池 雅人, 長野 哲也

[特許出願]

1. 「表面造形方法」 特願 2019-215176 (2019-11-28)
石野 雅彦, タンフン ズン, 錦野 将元, 東口 武史, 坂上 和之, 鷺尾 方一
2. 「パルス整形装置及びパルス整形方法」 特願 2019-239404 (2019-12-27)
錦野 将元, 森 道昭, タンフン ズン, 小島 完興, 長谷川 登, 近藤 公伯
3. “HIGH-Z ATOM-CONTAINING NANOPARTICLES IRRADIATED WITH A MONOCHROMATIC X-RAY AND CANCER THERAPY WITH THE SAME” 米国特許 62/907043 (2019-09-27)
玉野井 冬彦, 松本 光太郎, 田島 俊樹, 齋藤 寛之, 城 鮎美
4. 「組織識別装置、組織識別システム、組織識別方法、内視鏡システム、組織識別プログラムおよび記録媒体」 PTC/JP2019/017863 (2019-04-26)
山川 考一, 青山 誠, 森岡 孝満, 今岡 達彦
5. 「磁性体観察方法、磁性体観察装置」 PCT/JP2019/012018 (2019-03-22)
稲見 俊哉, 綿貫 徹, 上野 哲朗, 安田 良

The Kids' Science Museum of Photons

概要

4月10日には総来館者70万人を達成、ささやかな記念式典を行い、70万人目となられた木津川市在住の男性とお孫さんに記念品を贈呈しました。4月15日～21日は科学技術週間、DNA模型や偏光シートを使った工作、さらに機械部品をモチーフにしたレジン工作を楽しんでいただきました。映像ホールの新メニュー2作品も上映、きめ細やかで繊細なCGに引き込まれる「GRAVITATION」と研究施設内部と壮大なアンテナ群が圧巻の「ALMA」は、宇宙や科学の面白さを伝えてくれる素晴らしいコンテンツです。追加上映を行っても満席になる日もあったほど、多くの方々にご観賞いただきました。また、4月30日は超大入りで、1,000人余りの方々にご来館いただきました。

5月、こいのぼりで季節感を出した工作では、最初にパーツを選ぶ時から真剣なまなざしの親子の姿が。できあがると、小さな手でしっかりと愛おしそうに完成品を眺める参加者の様子がなんとも微笑ましいものでした。連休が明けると、学校団体の遠足・校外学習のシーズンに突入し、平日も盛況となりました。

6月には、中学校からの要望に応え、レーザーの特別ラボを、1日6回連続で242人の中学生に実施しました。

7月は科学館ロビーに大きな七夕飾りをセットすることから始まり、親子工作でも、スタッフが朝採りした笹を使って、手のひらに乗るくらいの「ミニミニ七夕」を実施しました。夏休みに入り、平日も賑わう毎日となり、臨時のスタッフも迎え、特に8月7日～14日のメインイベント期間には、いつもより工作数を増やし、連日開館前から工作希望の長い列ができました。お盆明けには、アマチュア無線社団局による免許不要の無線機の貸し出しが行われ、「無線ごっこ」を楽しむ親子の姿が見られました。

9月の“ふおとん プレハロウィン”では、一足早いハロウィン工作が始まりました。人気のレジン工作は2種類あり、暗闇に光るジャック・オー・ランタンのキーホルダーと、おじいちゃんやおばあちゃんに感謝を伝える敬老の日のキーホルダー作りです。それぞれの思いをメッセージに入れ、作品に取り組んでいた子供たちの姿が印象的でした。

10月～12月は、学校関係の団体見学が多く、近隣の梅美台小学校や主に京都・奈良の小学校からの団体見学に加え、神戸から200人近い中学3年生に来館いただき、科学館駐車場に大型バス4台が並んだ光景はそれなりに迫力のあるものでした。また、木津高校からは、豪州留学生13名を含む生徒26名が来館、プラネタリウムとレーザーラボを体験いただきました。

新年は1月4日から開館し、その翌日ともに、入館者数200人前後のおだやかなスタートとなりましたが、その後、入館者数は徐々に増え、月間入館者数は3,000人超と、例年の1月上回る大入りとなりました。お正月工作はおめでたいものをと、七福レジンや宝船プラバン、偏光板工作の偏光ねずみ、福笑いスーパーボール作りなどの工作イベントを開催しました。

科学館では、年中ハート型のミニたこ（バレンタインバージョン）が人気ですが、2月のバレンタイン週間には、キラキラパーツを散りばめたハート型のレジン工作に、女の子も男の子も、一所懸命取り組んでいました。地元ケーブルテレビ「KCN 京都」の取材があり、科学館の展示や光の不思議について紹介を行いました。3月前半の2週間、「My けいはんな」という番組で放送されました。

2020年2月27日以降は、新型コロナウイルスの感染拡大防止のため、臨時休館となりました（4月1日以降も当面の間、休館期間の延長が予定されています）。

3月23日～27日にかけて、プラネタリウムの制御用及び描画用機器等のハードウェアならびにデジ

タルプラネタリウムソフトウェアの更新、さらに光学部品の交換を行い、より鮮明な映像をご覧いただけるようになりました。

I. 2019年度の活動

1. 入館者状況

平日は主に幼児連れのお客様や、学校等による団体見学の利用が中心で、特に、今年度は中学・高校からの見学者数が昨年度の3倍程度（～1,100人）に増えました。また、土・日・祝日や夏休みなどには、多くのご家族に利用いただいています。今年度の入館者総数は50,963人と、関西研による科学館の直営が開始された2012年以降では初めて5万人を上回りました。

2. 主な行事

<2019年>

4月6、7、13、14、20、21、27～30日	ふおとん再始動
5月3～6、12、18、19、25、26日	ふおとん皐月祭
6月1、2、8、9、15、16、22、23、29、30日	ふおとんで雨やどり
7月6、7、13～15、20、21、24～28、31日	ふおとんプレ工作夏祭り
8月1～4、7～14、17、18、21～25、28～31日	ふおとん工作夏祭り2019
9月1、7、8、14～16、21～23、28、29日	ふおとんプレハロウィン
10月13～14、19、20、22、26、27日	Photons Halloween 2019
11月2～4、9、10、16、17、23、24、30日	ふおとん11月祭
12月1、7、8、14、15、21、22、25～28日	Photons Merry Christmas 2019

<2020年>

1月4、5、11～13、18、19、25、26日	Photons Happy New Year 2020
2月1、2、8、9、11、15、16、22～24日	Photons Happy Valentine 2020

3. 事業内容（実験・工作・映像）

(1) レーザーラボ

Nd:YAG や He-Ne レーザー、分光器等を用いた光及びレーザーのライブ実験を行っています。通常スケジュール、(午前) 11:45～12:05、(午後) 15:00～15:20、に加え、団体見学者用に適宜実施しました。2019年度の観覧者総数は9,559人。



レーザーラボ

実施実績（2019年4月1日～2020年2月26日）

年 月	実施日数	実施回数	観覧者数	累積観覧者数
2019年4月	20日	39回	897人	897人
5月	17日	30回	753人	1,650人
6月	19日	38回	1,085人	2,735人
7月	21日	37回	1,016人	3,751人
8月	23日	47回	1,885人	5,636人
9月	20日	34回	991人	6,627人
10月	16日	30回	622人	7,249人
11月	20日	37回	687人	7,936人
12月	16日	27回	454人	8,390人
2020年1月	17日	34回	604人	8,994人
2月	17日	28回	565人	9,559人
3月	-	-	-	9,559人
年度合計	206日	381回	9,559人	-

(2) レーザー加工体験

木製ブロックに、レーザーで文字や絵を刻印する「レーザー加工」を体験いただいています。(午前)10:30～11:30、(午後)14:00～14:45、に加え、団体見学者に対しては希望者の状況に応じて実施しました。木製ブロックの入手が困難となったため、12月以降は休止しました。



レーザー加工体験

実施実績（2019年4月1日～2020年2月26日）

年 月	実施日数	実施回数	体験者数	累積体験者数
2019年4月	21日	37回	262人	262人
5月	16日	27回	200人	462人
6月	18日	29回	254人	716人
7月	19日	38回	389人	1,105人
8月	23日	46回	653人	1,758人
9月	2日	3回	31人	1,789人
10月	7日	13回	61人	1,850人
11月	3日	6回	26人	1,876人

12月	-	-	-	1,876人
2020年1月	-	-	-	1,876人
2月	-	-	-	1,876人
3月	-	-	-	1,876人
年度合計	109日	199回	1,876人	-

(3) 実験・工作教室

主に小学生を対象とした実験・工作教室を、土日祝日休日を中心に、マルチホールとロビーにおいて開催しています。マルチホールでは、(午前) 10:30～11:00、(午後) 13:00～13:30 と 15:00～15:30、ロビーでは随時実施しました。

実験・工作教室実績 (2019年4月1日～2020年2月26日)

年 月	実施日数		マルチホール実験・工作		ロビー工作
	マルチ	ロビー	実施回数	参加者数	参加者数
2019年4月	13日	12日	36回	342人	1,702人
5月	12日	9日	33回	464人	1,262人
6月	10日	10日	31回	294人	1,853人
7月	16日	14日	38回	400人	2,657人
8月	23日	23日	86回	842人	4,663人
9月	11日	11日	32回	313人	2,360人
10月	9日	7日	28回	419人	1,166人
11月	12日	10日	33回	470人	863人
12月	16日	11日	35回	536人	944人
2020年1月	9日	9日	27回	268人	1,238人
2月	11日	10日	31回	296人	1,582人
3月	-	-	-	-	-
年度合計	142日	126日	410回	4,644人	20,290人

(4) 映像コンテンツの上映

光の映像ホール（ドーム型全天周映像ホール）において、通常スケジュール、(午前) 11:10～11:40、(午後) 14:00～14:30 と 15:40～16:10、に加え、団体見学者用に適宜、以下のコンテンツから1日あたり2～3作品の上映を行いました。2019年度の観覧者総数は35,439人。

1) 映像コンテンツ

①ALMA ～まだ見ぬ宇宙へ～ (29分)

南米チリのアタカマ砂漠、標高 5,000 メートルの地に誕生した電波望遠鏡 ALMA は 66 台のパラボラアンテナを駆使して、人類が見たことの無い宇宙の姿を鮮明に描き出します。星誕生の謎、生命誕生の神秘に迫る ALMA の能力と、美しいアタカマの大地、そして星空の映像とともに楽しみください。

②GRAVITATION ～魔法使いの少年とロボット 不思議な一夜～ (28分)

魔法でもないのに、なぜ物は地面に落ちるの?!

舞台となるのは架空のアインシュタイン博物館。見習い魔法使いの少年と小さな不思議なロボットが「時間」と「空間」をめぐる不思議な旅に出かけ、宇宙の秘密に迫ります。アインシュタインの一般相対性理論をテーマとして、子どもたちにも分かりやすく宇宙や科学の面白さを体感していただけます。

③プラネタリウム絵本「こぐま座のティオ」～星空だいぼうけん～ (27分)

プラネタリウムに来てくれた君、ぼくと一緒に天の川のピンチを助けに行こう。春夏秋冬の星座のお友だちと力を合わせて、さあ、ポンプ座まで星空だいぼうけんの始まり!

④恐竜の記憶 (25分)

国立科学博物館が収蔵する、ティラノサウルスとトリケラトプスの骨格標本を精確に三次元デジタル計測し、学術的監修のもとにバーチャルリアリティ映像としてコンテンツ化した立体感と奥行きのある高精細映像を投影します。

⑤宇宙 ～その大きさを感じてみよう～ (25分)

太陽系惑星の大きさ、距離、銀河系の大きさ、宇宙大規模構造等を紹介します。

⑥ふと気になる宇宙 (25分)

どこからが宇宙? 宇宙の大きさって? 等宇宙の話題について紹介します。

⑦THE MOON 月の不思議 (25分)

月の満ち欠け、月面の様子、地球からの距離や大きさの比較、月の生成、誕生の歴史を紹介します。

⑧ブラックホールの謎?! 驚異の深宇宙 (25分)

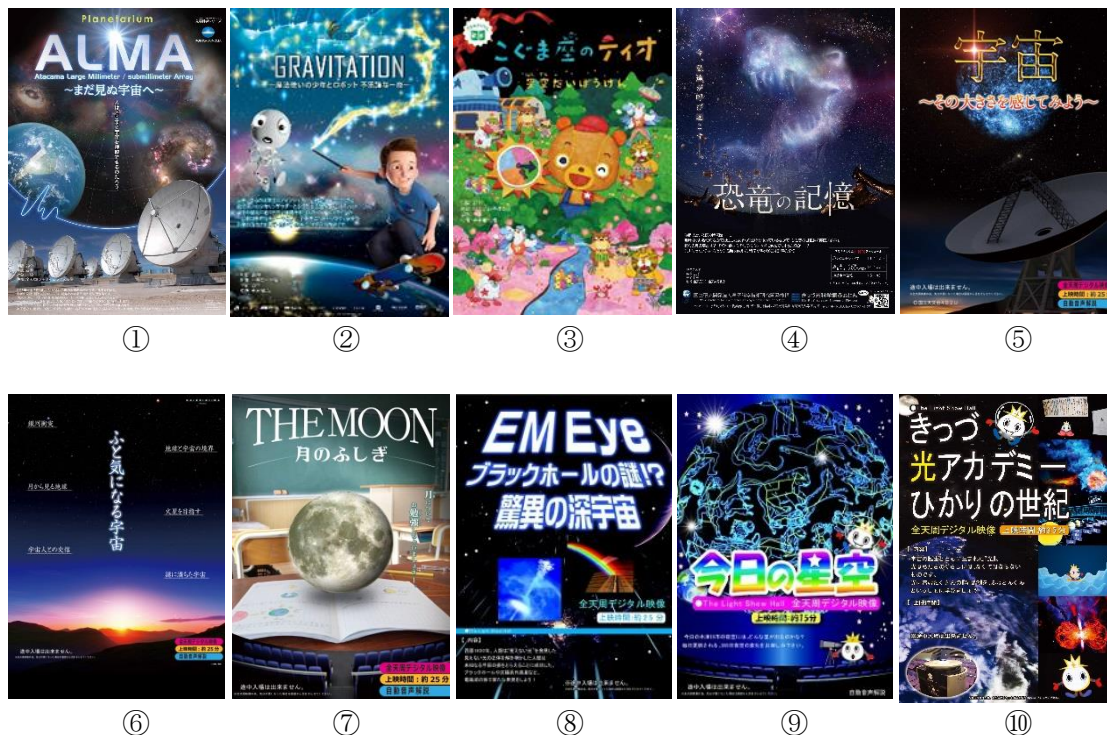
ブラックホールや太陽系外惑星などを電磁波の旅で探ります。

⑨今日の星空 (15分)

今日の本津川市の星空を紹介します。

⑩きつづ光アカデミー ひかりの世紀 (35分)

光に潜むたくさんの不思議を光科学館のマスコット「ふおとんくん」と一緒に学びます。



2) 上映実績 (2019年4月1日～2020年2月26日)

年 月	上映日数	上映回数	観覧者数	累積観覧者数
2019年4月	22日	70回	3,595人	3,595人
5月	20日	58回	3,254人	6,849人
6月	22日	67回	3,708人	10,557人
7月	21日	68回	3,952人	14,509人
8月	23日	69回	6,367人	20,876人
9月	21日	62回	3,296人	24,172人
10月	19日	60回	2,490人	26,662人
11月	22日	69回	2,284人	28,946人
12月	20日	60回	1,987人	30,933人
2020年1月	20日	54回	2,199人	33,132人
2月	18日	46回	2,307人	35,439人
3月	-	-	-	35,439人
年度合計	228日	683回	35,439人	-

4. 実験・工作実施例

4月



ミニミニ
スコープ



スーパー
ふおとんボール



ミニプラバン



レジ
アラカルト



偏光トンネル mini

5月



こどもの日
スコープ



こどもの日
スーパーボール



こどもの日
プラバン



こどもの日
レジ



母の日
レジ

6月



父の日レジ
&プラバン



レインボー
ボール



レイン棒



しおり作り (日光写真)

7月



七夕プラバン



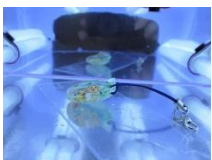
ミニミニ七夕



マリンスーパーボール



マリンスコープ



マリレジ



花火スーパー
ボール



花火キラキラ棒



ミニ花火
プラバン



星座表を作ろう

8月



ミニ金魚プラバン



金魚レジン



すいかキーホルダー



プラカップ・メダル



コイルモーター



星座プラバン



紙コップカメラ



コスモプラバン

9月



敬老の日レジン



ハロウィン
キラキラ棒



ハロウィン
ポラライザー

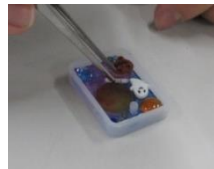


ハロウィンレジン

10月



ハロウィンプラバン



ハロウィンレジン



ハロウィンスコープ



ハロウィン
スーパーボール

11月



洋食レジン



食べ物プラバン



きのこプラバン



オータムスコープ

12月



クリスマス
プラバンレジン



クリスマススーパー
ボール



クリスマススcoop



クリスマスレジン



クリスマス
キラキラツリー



スーパースノーボール

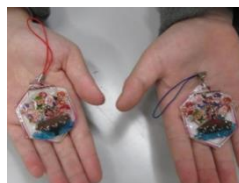


梅美台小学生



木津高校生・
豪州留学生

1月



七福レジン



宝船プラバン



偏光ねずみ



福笑いスーパー
ボール

2月



バレンタインレジン



バレンタインプラバン



キラキラ棒
(ハートバージョン)



レジンアラカルト

3月 (臨時休館)



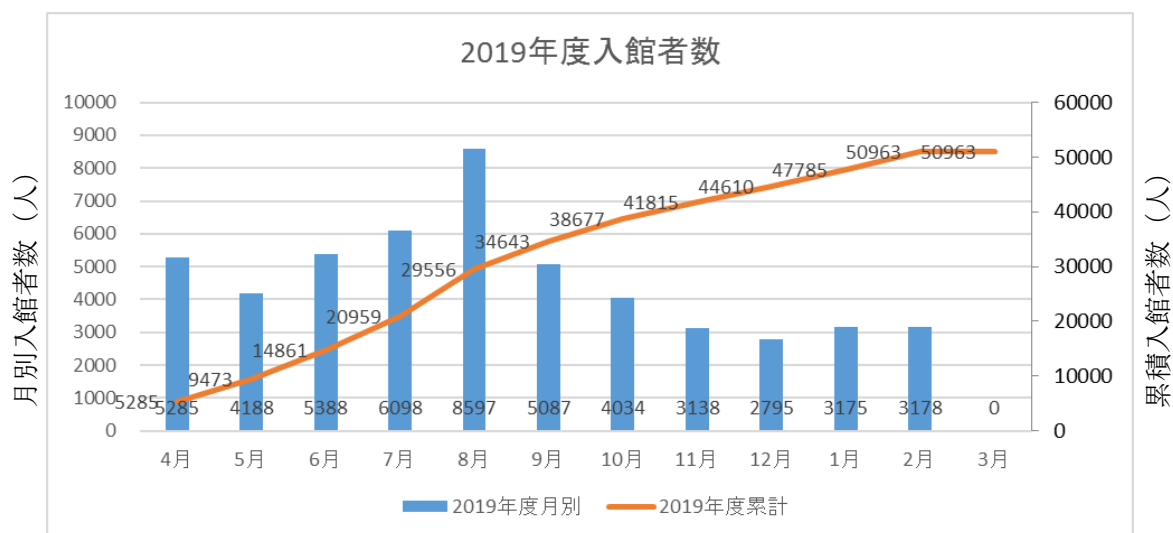
KCN 京都の取材

Ⅱ. 2019年度利用状況

1. 入館者数（2019年4月1日～2020年2月26日）

		開館日数	入館者数	
			月別	累計
2019	4月	22日	5,285人	5,285人
	5月	20日	4,188人	9,473人
	6月	22日	5,388人	14,861人
	7月	21日	6,098人	20,959人
	8月	23日	8,597人	29,556人
	9月	21日	5,087人	34,643人
	10月	19日	4,034人	38,677人
	11月	22日	3,138人	41,815人
	12月	20日	2,795人	44,610人
2020	1月	20日	3,175人	47,785人
	2月	18日	3,178人	50,963人
	3月	-	-	50,963人
年度合計		228日	50,963人	-

2. 月別及び累積入館者数分布（2019年4月1日～2020年2月26日）



Appendix

共同研究課題、施設共用課題

1) 木津地区

【共同研究課題】

共同研究先	共同研究課題名	担当研究グループ
慶應義塾大学、(株)ユニタック、 近畿大学	レーザーを活用した整形外科インプラント設置強 度評価機構の開発	X線レーザー研究 グループ
(株)島津製作所	高耐性光学デバイスの開発研究	X線レーザー研究 グループ
宇都宮大学、広島大学、東北大 学	水の窓高輝度軟X線発生に関する基礎研究	X線レーザー研究 グループ
京都大学	レーザー誘起弾性波を用いた道路橋床板の非破壊 検査に関する研究	X線レーザー研究 グループ
(株)フォトンラボ	レーザー誘起振動波計測技術の小型化に関する研 究	X線レーザー研究 グループ
九州大学	高効率フェムト秒レーザーアブレーションに関す る基礎研究	X線レーザー研究 グループ
核融合科学研究所、東北大学	分子動力学シミュレーションを用いたフェムト秒 レーザーアブレーションに関する研究	X線レーザー研究 グループ
レーザー技術総合研究所	レーザーを用いた遠隔計測手法に関する研究	X線レーザー研究 グループ
京都大学、大阪大学	フェムト秒レーザー表面加工による異材接合に関 する研究	X線レーザー研究 グループ
京都大学	TW 級 TiS レーザーを用いた量子ビーム発生に関 する研究	X線レーザー研究 グループ
奈良女子大学、双葉鉄道工業 (株)	レーザー計測手法の精度向上に関する研究	X線レーザー研究 グループ
東京学芸大学	リラクサー強誘電体のドメイン形成に関する研究	X線レーザー研究 グループ
NTT アドバンステクノロジー(株)	高耐力軟X線光学素子に関する基礎研究	X線レーザー研究 グループ
兵庫県立粒子線医療センター	量子メスに向けた粒子線照射計測・制御技術に関 する研究	高強度レーザー科学 研究グループ
大阪大学	ステーjingレーザー加速の安定化研究	高強度レーザー科学 研究グループ
大阪大学	超高強度レーザーと固体物質からのガンマ線発生 および核物理に関する研究	高強度レーザー科学 研究グループ
神戸大学	固体飛跡検出器を用いた高エネルギーイオン検出 手法開発	先端レーザー技術 開発グループ

東京大学、神戸大学	水素クラスターをターゲットとした 100 MeV を超えるレーザー陽子加速の実証	先端レーザー技術開発グループ
神戸大学、名古屋大学	原子核乾板を用いた 100MeV 級レーザー加速プロトンの特性評価	先端レーザー技術開発グループ
京都大学	高強度レーザーと構造的媒質との相互作用に関する研究	先端レーザー技術開発グループ
大阪大学	宇宙物理の手法に基づく粒子加速・電磁放射に関する研究	先端レーザー技術開発グループ
京都大学	高強度光子場による固体電子駆動に関する基礎研究	超高速光物性研究グループ
奈良先端科学技術大学院大学	有機半導体におけるフォノン-励起子相互作用を利用した状態制御に関する基盤技術開発	超高速光物性研究グループ
理化学研究所	テラヘルツパルス光源による高分子高次構造の制御	超高速光物性研究グループ
大阪大学	高強度テラヘルツパルス光源による新規物質創成と新規物性発現に関する研究	超高速光物性研究グループ
東京大学	薄ディスクレーザー励起光パラメトリックチャープ増幅装置に関する研究開発	超高速光物性研究グループ
ライトタッチテクノロジー(株)	中赤外レーザーを用いたがん診断技術の開発	光量子科学研究部
東北大学、(株)島津製作所	極端紫外線領域の低入射角高効率回折格子の開発	光量子科学研究部

【施設共用課題】

令和元年度施設共用課題

課題番号	利用区分	施設装置	利用課題
2019A-K01	公開	J-KAREN レーザー装置	非線形逆コンプトン散乱によるガンマ線渦の発生とらせん波面測定
2019A-K02	公開	J-KAREN レーザー装置	J-KAREN レーザーによるグラフェンを用いた高エネルギーイオン加速
2019A-K04	公開	J-KAREN レーザー装置	無衝突衝撃波による準単色イオン生成の物理機構解明
2019A-K05	公開	J-KAREN レーザー装置	高強度レーザーと構造的媒質の相互作用による高エネルギー密度プラズマの閉じ込めと磁場生成

2) 播磨地区

【共同研究課題】

共同研究先	共同研究課題名	担当研究グループ
兵庫県立大学	反応性ガスクラスタライオンビームによる新規化合物の創製と電子状態の解析	磁性科学研究グループ
京都大学	同位体特定による局所状態解明のための先進的メスbauer分光法の開発研究	磁性科学研究グループ
広島大学	コヒーレント X 線を利用した強誘電体一粒子計測	コヒーレント X 線利用研究グループ
京都大学	ナノ粒子を取り込んだがん細胞に及ぼす高エネルギー単色 X 線照射の影響に関する研究	高圧・応力科学研究グループ
JEF テクノリサーチ(株)	磁気円偏光発光を用いた方向性珪素鋼板の内部磁区観察のための研究開発	磁性科学研究グループ
高輝度光科学研究センター	次世代ハイブリッド型二次元検出器の開発とその応用研究	高圧・応力科学研究グループ

【施設共用課題】

播磨地区では 2012 年度より文部科学省のナノテクノロジープラットフォーム事業を受託しており、放射光科学研究施設を成果公開型課題で利用する外部研究者に対して、特に専用ビームラインにおける研究支援を強化しています。課題は年 2 回、SPring-8 を運営する公益財団法人高輝度光科学研究センターの一般課題募集時期（5 月及び 11 月）に合わせて募集しています。

令和元年度前期施設共用課題

課題番号	利用区分	利用装置	研究課題
2019A-H01	公開	放射光メスbauer分光装置	単分子磁石中における金属分子間電荷移動研究のためのGd放射光メスbauer吸収分光法の高度化
2019A-H02	公開	放射光メスbauer分光装置	Sm(Fe _{1-x} Co _x) ₁₂ 薄膜の内部磁場の温度依存性
2019A-H03	公開	放射光メスbauer分光装置	高感度放射光メスbauer回折装置の開発（2）
2019A-H04	公開	共鳴X線非弾性散乱装置	有機合成用鉄触媒の高精度電子状態解析
2019A-H05	公開	共鳴X線非弾性散乱装置	共鳴非弾性X線散乱を用いた擬一次元Ni酸化物の電荷移動励起観測
2019A-H06	公開	表面X線回折計	RF-MBE法による窒化物半導体成長初期過程のXRDその場観察
2019A-H07	公開	表面X線回折計	機械学習によるX線回折パターンの特徴抽出と応用

2019A-H08	公開	表面X線回折計	Si基板上GaAs成膜における歪緩和過程のその場X線構造解析
2019A-H09	公開	表面X線回折計	その場X線回折測定を用いたグラフェン析出成長メカニズムの検討
2019A-H10	公開	表面X線回折計	SiO ₂ 基板に転写されたグラフェン上でのGa ₂ O ₃ 結晶成長のリアルタイムX線回折
2019A-H11	公開	高温高圧プレス装置	水素組成制御下の六方晶鉄水素化物の合成と安定温度圧力の決定
2019A-H12	公開	高温高圧プレス装置	Mo-H二元系温度圧力状態図決定のための放射光X線その場観察
2019A-H13	公開	高温高圧プレス装置	U曲げ加工した自動車用高強度鋼板の応力分布と水素脆化の関係
2019A-H14	公開	高温高圧プレス装置	高エネルギー密度負極活物質C ₂ Liの生成過程のその場観察(2)
2019A-H15	公開	ダイヤモンドアンビルセル回折計	PbCoO ₃ の圧力下温度誘起金属絶縁体転移機構解明と負熱膨張の観測
2019A-H16	公開	ダイヤモンドアンビルセル回折計	X線PDF解析を用いた乾燥がもたらすC-S-Hの分子構造の変化の解明
2019A-H17	公開	ダイヤモンドアンビルセル回折計	BCC型水素吸蔵合金の水素化物の局所構造解析 ～4d、5d遷移金属置換が水素吸蔵特性及び局所構造に及ぼす影響～
2019A-H18	公開	ダイヤモンドアンビルセル回折計	X線PDF解析による合成C-S-Hの高温加熱及び再水和による構造変化及び変形挙動特性の解明
2019A-H19	公開	大型X線回折計	レーザー急冷法によるリラクサー強誘電体における不均一競合相の解明
2019A-H20	公開	大型X線回折計	DyNi ₃ Ga ₉ における電気四極子らせん秩序の観測
2019A-H22	公開	表面X線回折計	放射光X線を用いた格子不整合III-V族化合物半導体混晶のリアルタイム構造解析

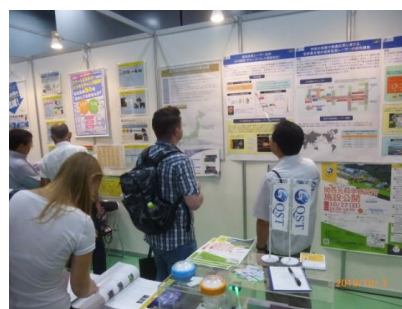
令和元年度後期施設共用課題

課題番号	利用区分	施設装置	利用課題
2019B-H01	公開	放射光メスbauer分光装置	電子/X線を区別した放射光メスbauer吸収分光法の開発
2019B-H02	公開	放射光メスbauer分光装置	(Sm _{1-x} Zr _x)(Fe _{1-y} Co _y) ₁₂ 薄膜の内部磁場の温度依存性

2019B-H03	公開	放射光メスバウアー分光装置	放射光メスバウアー回折による自然鉄試料のサイト選択的スペクトル測定
2019B-H05	公開	共鳴非弾性X線散乱装置	有機合成用鉄触媒の高精度電子状態解析
2019B-H06	公開	共鳴非弾性X線散乱装置	方向性珪素鋼板におけるランセット磁区の内部構造の可視化
2019B-H07	公開	表面X線回折計	機械学習のX線ビーム位置の補正と結晶成長その場観察への応用
2019B-H08	公開	表面X線回折計	その場X線回折測定を用いた析出成長グラフェンにおける面内配向メカニズムの解明
2019B-H09	公開	表面X線回折計	単層MoS ₂ 上でのGa ₂ Nのリモートエピタキシー過程のリアルタイムX線回折
2019B-H10	公開	表面X線回折計	InGa ₂ N量子構造形成におけるその場X線回折測定
2019B-H11	公開	高温高圧プレス装置	鉄-水素系の高温高圧相図の再検証
2019B-H12	公開	高温高圧プレス装置	超高压水素化技術を活用した高容量新規水素化物の合成および水素化物の安定性に対する水素同位体効果に関する基礎研究
2019B-H13	公開	高温高圧プレス装置	高水素配位錯イオンの形成過程における水酸化物イオン添加効果
2019B-H14	公開	高温高圧プレス装置	自動車用ホットスタンプ鋼板と冷間プレス鋼板の応力、ひずみ分布と水素脆化の関係
2019B-H15	公開	高温高圧プレス装置	鉄鋼材料の圧縮過程のX線その場観察技術の開発
2019B-H16	公開	高温高圧プレス装置	異種材料抵抗スポット溶接継手界面凝固部の攪拌状態と金属間化合物の非破壊測定
2019B-H17	公開	高温高圧プレス装置	単色X線と白色X線を利用したCdTeピクセル検出器によるひずみ評価の検証
2019B-H18	公開	高温高圧プレス装置	マグネシウム単結晶の4点曲げ試験中の放射光透過ラウエ解析
2019B-H19	公開	ダイヤモンドアンビルセル回折計	BiNiO ₃ の高圧低温電荷グラス相安定領域の解明
2019B-H20	公開	ダイヤモンドアンビルセル回折計	放射光全散乱測定によるカチオンディスオーダー型Li ₂ MnO ₃ 電極材料の充放電過程における局所構造解析
2019B-H21	公開	ダイヤモンドアンビルセル回折計	高温型の水素雰囲気下X線全散乱実験用試料セルの開発とそれを活用した新規発熱現象の理解

関西光科学研究所での各種シンポジウム・施設公開・出展・アウトリーチ活動

関西研（木津地区、播磨地区）では、各種シンポジウム、セミナー、ワークショップ、研究会等を開催しています。また、研究所として参加した会合についても、主なものを記載しています。その他、関西研では、施設公開（播磨地区1回（毎年4月ごろ）、木津地区1回（毎年10月ごろ））や研究成果のわかり易い公表、光科学の基礎についての出前授業、科学啓発イベント等への出展を積極的に進めています。ここでは主なものを記載し、KPSIセミナー、QST播磨セミナー、S-cube（スーパーサイエンスセミナー）については別途記載しています。



京都スマートシティエキスポ 2019

【木津地区】

1	7-April-2019	高崎量子応用研究所（群馬県高崎市）	主催：高崎量子応用研究所
	第42回花と緑の見学会		
2	12-June-2019	大阪大学・银杏会館（大阪府吹田市）	主催：量研関西光科学研究所、大阪大学レーザー科学研究所
	光・量子ビーム科学合同シンポジウム 2019 OPTO2019 Symposium on Photon and Beam Science		
3	25-July-2019	みやこメッセ（京都市左京区）	主催：一般社団法人日本能率協会
	夏休み 2019 宿題 自由研究大作戦！		
4	27-28-July-2019	科学技術館（東京都千代田区）	主催：日本科学技術振興財団
	青少年のための科学の祭典 2019		
5	3-August-2019	関西光科学研究所（木津地区）	主催：日本加速器学会
	第16回日本加速器学会年会・施設見学会		
6	22-September-2019	大阪市中央公会堂（大阪府大阪市北区）	主催：大阪大学レーザー科学研究所
	IFSA2019 公開イベント「核融合とレーザー」		
7	3-4-October-2019	けいはんなオープンイノベーションセンター（京都府相楽郡精華町及び木津川市）	主催：京都スマートシティエキスポ運営協議会
	京都スマートシティエキスポ 2019		
8	3-4-October-2019	けいはんなオープンイノベーションセンター（京都府相楽郡精華町及び木津川市）	主催：関西文化学術研究都市推進機構
	けいはんなビジネスメッセ 2019		
9	27-October-2019	関西光科学研究所（木津地区：京都府木津川市）	主催：関西光科学研究所

	関西光科学研究所施設公開（木津地区）		
10	31-October, -2-November-2019	けいはんなプラザ（京都府相楽 郡精華町）	主催：けいはんな情報通信フェア 2019 実 行委員会、情報通信研究機構、関西文化学 術研究都市推進機構、国際電気通信基礎技 術研究所、関西経済連合会
	けいはんな情報通信フェア 2019		
11	4-5-December-2019	奈良春日野国際フォーラム”薨” （奈良県奈良市）	主催：QST
	第3回 QST 国際シンポジウム “Quantum Life Science（参考訳：量子生命科学）”		
12	5-6-December-2019	福井大学附属国際原子力工学研 究所（福井県敦賀市）	主催：日本原子力研究開発子機構（敦賀総 合研究開発センター）
	福井大学附属国際原子力工学研究所（福井県敦賀市）		
13	19-20-December-2019	関西光科学研究所（木津地区： 京都府木津川市）	主催：日本原子力研究開発機構
	PHITS 講習会		
14	6-7-December-2019	福井大学附属国際原子力工学研 究所（福井県敦賀市）	主催：日本原子力研究開発子機構（敦賀総 合研究開発センター）
	レーザー応用技術 産学官連携成果報告会		
15	13-14-February-2020	伊勢かぐらばリゾート千の杜 （三重県伊勢市）	主催：RIKEN-RAP & QST- KPSI
	第3回 RIKEN-RAP & QST-KPSI ジョイントセミナー		

【播磨地区】

1	27-April-2019	SPring-8（兵庫県佐用郡佐用町）	主催：理化学研究所放射光科学研究センタ ー
	第27回 SPring-8/SACLA 施設公開（関西研）		
2	7-10-July-2019	SPring-8（兵庫県佐用郡佐用町）	主催：兵庫県立大学大学院物質理学研究科・ 生命理学研究科、関西学院大学大学院理工 学研究科、東京大学放射光分野融合国際卓 越拠点、岡山大学大学院自然科学研究科、大 阪大学・未来科学光科学連携センター・蛋白 質研究所・核物理研究センター、（公財）高 輝度光科学研究センター、理化学研究所放 射光科学研究センター、日本原子力研究開 発機構 物質科学研究センター、量子科学技 術研究開発機構 放射光科学研究センター
	第19回 SPring-8 夏の学校		
3	20-21-July-2019	姫路科学館（兵庫県姫路市）	主催：姫路市
	姫路桜山公園まつり「科学の屋台村」		
4	27-August-2019	兵庫県立工業技術センター（兵 庫県神戸市須磨区）	主催：QST 微細構造解析プラットフォーム、 JAEA 微細構造解析プラットフォーム、 NIMS 微細構造解析プラットフォーム

	令和元年度文部科学省ナノテクノロジープラットフォーム事業 JAEA、NIMS&QST 微細構造解析プラットフォーム放射光設備利用講習会 ―構造・電子状態・表面界面の分析―		
5	30-31-August-2019	岡山大学（岡山市北区）	主催：SPring-8 ユーザー協同体（SPRUC）、（公財）高輝度光科学研究センター、理化学研究所放射光科学研究センター、岡山大学
	SPring-8 シンポジウム 2019		
6	24-September-2019	東京大学（東京都文京区）	主催：ナノテクノロジープラットフォームセンター
	文部科学省ナノテクノロジープラットフォーム 令和元年度 利用成果発表会		
7	25-September-2019	東京大学（東京都文京区）	主催：ナノテクノロジープラットフォームセンター
	令和元年度学生研修・米国 NNCI 施設利用研修プログラム成果発表会		
8	17-October-2019	播磨高原東中学校（兵庫県たつの市）	主催：関西光科学研究所 放射光科学研究センター
	播磨高原東中学校出前授業		
9	10-12-January-2020	ウインクあいち（愛知県名古屋市中村区）	主催：第 33 回日本放射光学会年会・放射光科学合同シンポジウム組織委員会
	第 33 回日本放射光学会年会・放射光科学合同シンポジウム		
10	29-31-January-2020	東京ビッグサイト（東京都江東区）	主催：nano tech 実行委員会
	nano tech 2020		
11	31-January-2020	東京ビッグサイト（東京都江東区）	主催：ナノテクノロジープラットフォームセンター
	JAPAN NANO 2020 第 18 回ナノテクノロジー総合シンポジウム		
12	10-February-2020	SPring-8（兵庫県佐用郡佐用町）	主催：関西光科学研究所、協力：SPRUC キラル磁性・マルチフェロイックス研究会、SPRUC コヒーレント X 線物質科学研究会
	キラル磁性・マルチフェロイックス研究会、コヒーレント X 線物質科学研究会、QST 播磨セミナー合同研究会		



左：青少年のための科学の祭典 2019



右：放射光設備利用講習会 ―構造・電子状態・表面界面の分析―

KPSI セミナー

QST 木津地区では国内外の著名な研究者をお招きして学術的に最先端の専門的なセミナーを開催しています。今年度は合計 21 回のセミナーを開催しました。開催にあたっては KPSI Web サイトやメーリングリストを活用し、関西研内外に開催案内を行っています。また報告については Web サイト、関西研だより等を活用しています。(参加費無料・事前登録制)



Web サイト : <https://www.qst.go.jp/site/kansai-english/29630.html>

53	10-April-2019	Prof. Tano Keizo	Institute for Integrated Radiation and Nuclear Science, Kyoto University/ Japan
	Reverse genetic analysis of the DNA damage response mechanism and the applied examples in the vertebrate cells		
54	15-April-2019	Dr. Hayakawa Takehito	LCS gamma-ray project, QST/ Japan
	Basic techniques for gamma-ray measurements and ideas for laser derive gamma-ray sources		
55	18-April-2019	Dr. Yano Masahiro	Osaka University
	Effects of hole-boring and relativistic transparency on particle acceleration in overdense plasma irradiated by short multi-PW laser pulses		
56	19-April-2019	Dr. Csaba Tóth	Lawrence Berkeley National Laboratory/ CA USA
	Particles Surfing on Plasma Waves: Ultrahigh Intensity Lasers used for High-Gradient Acceleration of Electrons and Ions		
57	17-May-2019	Prof. Jack Tuszynski	University of Alberta/ Canada and Politecnico di Torino/ Italy
	On the biophysical properties of microtubules and their importance in health and disease		
58	23-May-2019	Prof. Sergei Popov	KTH Royal Institute of Technology/ Sweden and The University of Tokyo/ Japan
	Ultra high intense laser matter interaction and their application		
59	23-May-2019	Dr. William Rieken	Nara Institute of Science and Technology/ Japan
	Morphological Superconductors: Fundamental discoveries in Superconducting Materials		
60	4-June-2019	Prof. Matsumoto Kunio	Kanazawa University/ Japan
	Macrocyclic Peptide Drug Discovery Targeting Hepatocyte Growth Factor and the Receptor		
61	4-June-2019	Director , Prof. Yasui Takeshi	Tokushima University/ Japan
	Dual-comb microscopy for scan-less confocal imaging		

62	28-June-2019	Assoc. Prof. Suzuki Masayuki	Doshisha University/ Japan
	Spectral dynamics in build-up femtosecond pulse with time stretch spectroscopy		
63	2-July-2019	Dr. Imasaka Kotaro	Institute of Industrial Science, The University of Tokyo/ Japan
	High harmonic generation in solids and the driving by plasmonic enhanced field		
64	18-July-2019	Dr. Ishii Nobuhisa	Environmental Genomics Laboratory, Institute of Genome Research (IGR), Vietnam Academy of Science and Technology (VAST).)
	Development of an intense few-cycle light source in the infrared and its application to ultrafast soft x-ray spectroscopy of nitric oxide and nitrogen dioxide		
65	25-July-2019	Prof. Luis Roso.	Centro de Láseres Pulsados Ultracortos, Salamanca/ Spain
	The Spanish Petawatt Laser: high repetition rate challenges		
66	2-August-2019	Dr. Matsubara Hiroki	Tohoku University/ Japan
	Molecular scale picture of heat conduction in liquids based on molecular dynamics simulation		
67	22-August-2019	Dr. A. Zhidkov	The Institute of Scientific and Industrial Research, Osaka University/ Japan
	Characterization of Ionization Injection in Gas Mixtures Irradiated by PW Laser Pulses		
68-1	19- September-2019	Dr. Ondrej Klimo	FNSPE, Czech Technical University in Prague, Institute of Physics of the ASCR, ELI-Beamlines / Czech Republic
	Lecture by ELI-BL theory group		
68-2	19- September-2019	Dr. YanJun Gu	Institute of Physics of the ASCR, ELI-Beamlines, Institute of Plasma Physics of the CAS / Czech Republic
	High Harmonic Generation and QED Effects Induced by Relativistic Oscillating Mirror		
68-3	19- September-2019	Dr. Martin Matys	Institute of Physics of the ASCR, ELI-Beamlines project, FNSPE, Czech Technical University/ Czech Republic
	Double layer target with interface modulations for laser acceleration of collimated ion beams		
69	25-September-2019	Dr. Martin Tolley	Central Laser Facility, RAL/ UK
	Microtarget Fabrication for High Power Laser Facilities and Future High Repetition Rate Drivers		
70	11-November-2019	Mr. Petr Valenta	PhD student at the Czech Technical University in Prague/ Czech Republic
	Research on Relativistic Mirrors at ELI Project		
71	6-December-2019	Prof. Ozaki Tsuneyuki	Institut national de la recherche scientifique (INRS), Québec/ Canada
	The “Odd” Harmonics – harmonics via the four-step model and terahertz harmonics		

72	4-February-2020	Dr. Hayakawa Takehito	Tokai Quantum Beam Science Center, QST/ Japan
	Generation and detection of “photon vortex” in quantum level		
73	25-February-2020	Prof. Morishita Toru	The University of Electro-Communications/ Japan
	Intense-laser-induced rescattering photoelectron spectroscopy of atomic and molecular systems		

QST 播磨セミナー

播磨地区では国内外の著名な研究者をお招きして学術的に最先端の専門的なセミナーを開催しています。

11	4-July-2019	Dr. Fujiwara Kosuke	JASRI
	Iron Vacancy Effect in Electric Ferroelectric Material YbFe_2O_4 and Development of Möössbauer Diffraction Measurement with Synchrotron Source		
12	30-July-2019	Dr. Koide Hiroaki	QST
	Application of electron scattering theory to X-ray spectroscopy		
13	21-November-2019	Dr. Endo Naruki	AIST
	Development and demonstration of a stationary H_2 energy system		



左：第12回 QST 播磨セミナー



右：第13回 QST 播磨セミナー

S-cube (スーパーサイエンスセミナー)

中学高校生を中心に一般の方に光科学についての理解を深めていただくことを目的に、第一線の研究者による講義「S-cube (エスキューブ：スーパーサイエンスセミナー)」を開講しています。

2019年度は合計6回(第210回～第215回)開催しました。

Webサイト：<https://www.qst.go.jp/site/kansai-topics/29911.html>

210	13-June-2019	講師：遠藤 友随 超高速光物性研究グループ	125人参加
	テーマ：光で分子を知る、見る、壊す		
211	14-June-2019	講師：乙部 智仁 超高速光物性研究グループ	125人参加
	テーマ：コンピュータの中に実験室を作る		
212	3-December-2019	講師：遠藤 友随 超高速光物性研究グループ	40人参加
	テーマ：光で分子を知る、見る、壊す		
213	3-December-2019	講師：宮坂 泰弘 先端レーザー技術開発グループ	43人参加
	テーマ：めざせレーザーマスター		
214	5-December-2019	講師：乙部 智仁 超高速光物性研究グループ	40人参加
	テーマ：コンピュータの中に実験室を作る		
215	30-January -2020	講師：近藤 康太郎 高強度レーザー科学研究グループ	41人参加
	テーマ：光に導かれてきた？これまでの軌跡とこれから		



左：和歌山県立向陽高等学校 (S-cube)



右：宮城県富谷高等学校 (実験室棟見学)

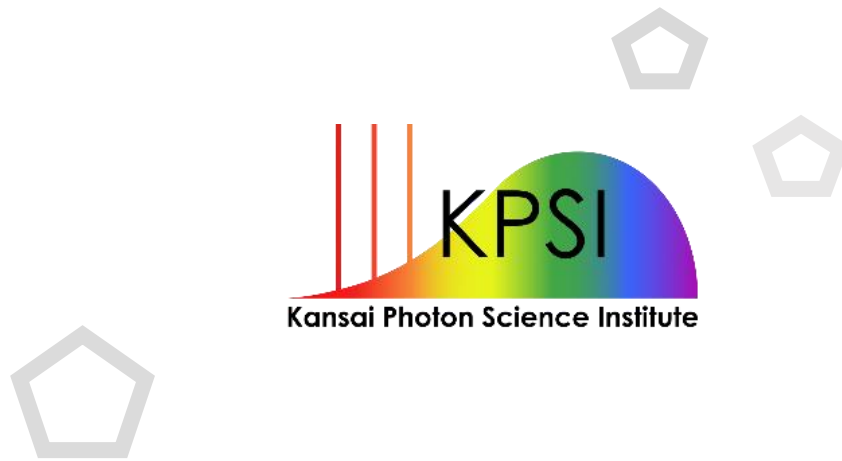
関西光科学研究所2019年度年報
KPSI Annual Report 2019

【発行】
2020(令和2)年7月

【編集・発行】
国立研究開発法人量子科学技術研究開発機構
関西光科学研究所 管理部庶務課

【印刷】
株式会社アイプリコム

©2020 国立研究開発法人量子科学技術研究開発機構



Kansai Photon Science Institute
Quantum Beam Science Research Directorate
National Institutes for Quantum and Radiological Science and Technology

8-1-7, Umemidai, Kizugawa-shi, Kyoto 619-0215, Japan
<https://www.qst.go.jp/site/kansai-english/>